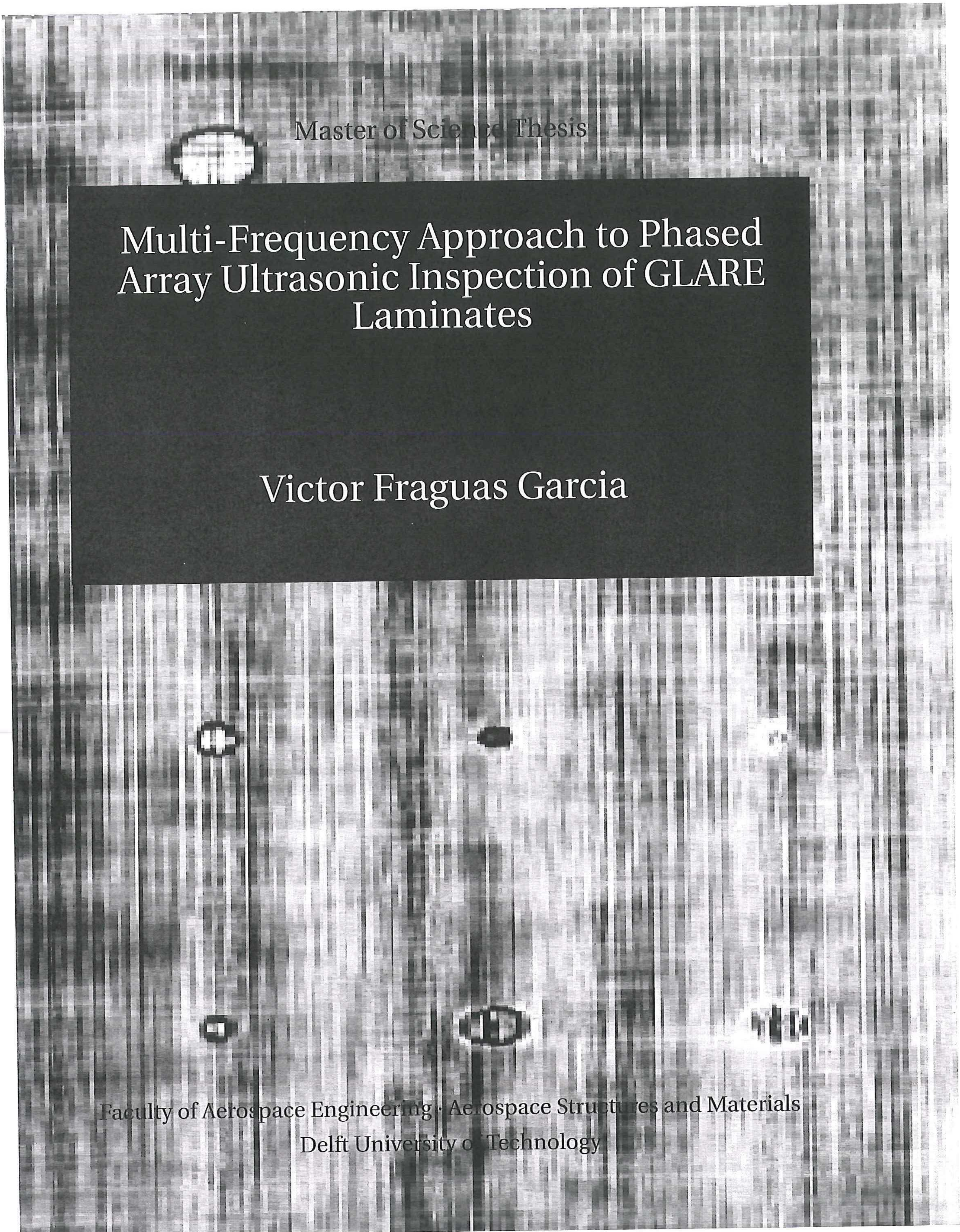

Master of Science Thesis

Multi-Frequency Approach to Phased Array Ultrasonic Inspection of GLARE Laminates

Victor Fraguas Garcia

Faculty of Aerospace Engineering · Aerospace Structures and Materials
Delft University of Technology

TU Delft Delft University of Technology

Multi-Frequency Approach to Phased Array Ultrasonic Inspection of GLARE Laminates

Master of Science Thesis

For obtaining the degree of Master of Science in Aerospace Engineering at Delft University of Technology

Victor Fraguas Garcia

December 16, 2014

Head of Department:

Prof.dr.ir. R. Benedictus

Thesis Committee:

Dr. R.M. Groves

Ir. F. Buijsen

Dr.ir. R.C. Alderliesten

Dr.ir. M. Snellen

The work in this thesis was supported by TiaT Europe BV. Their cooperation is gratefully acknowledged.

Abstract

Fiber Metal Laminates have been increasingly used in aerospace applications due to their light weight and superior fatigue properties. One such material is GLARE, consisting of aluminum and glass fibers embedded in epoxy adhesive which is currently being used in aircraft such as the Airbus A340 and A380. This gave rise to the need to perform in-service and non-scheduled maintenance inspections on such materials in order to ensure their safe operation whilst minimizing the down time of the aircraft. Answering the market's call for a quick and reliable Non-Destructive Testing (NDT) method, a multi-frequency approach to pulse-echo Phased Array Ultrasonic inspection was suggested. The Phased Array Ultrasonic (PAUT) method works on the same principles as conventional ultrasonic inspection but benefits from the flexibility of having several individual piezoelectric crystals capable of focusing and steering the ultrasonic beam as well as allowing for a quicker scan.

This thesis aims to investigate and understand the effects that the frequency of PAUT transducers has on the detection and characterization of delaminations in GLARE laminates in order to assess the potential usefulness of applying a multi-frequency pulse-echo PAUT inspection method for GLARE laminates. It was expected that different frequencies would be capable of exclusively detecting defects that the other frequencies could not detect, making a multi-frequency approach an attractive option to detect all defects that might be present in a structure.

To determine the effects that the frequency of PAUT transducers had on the detection and characterization of delaminations in GLARE, three different GLARE test samples were inspected utilizing commercial PAUT transducers operating at 2.25MHz, 5MHz and 10MHz frequencies. Furthermore, an ultrasonic model used to calculate the attenuation of ultrasonic waves in through-transmission was adapted to calculate the attenuation of ultrasonic waves in a pulse-echo method in order to provide a better understanding of the frequency interaction with GLARE. This model was then validated with real test results.

From the testing it was concluded that the 5MHz frequency could detect defects of 3mm and 6mm in diameter better than both the 2.25MHz and 10MHz frequencies in all the test samples. It was also determined that both the 2.25MHz and 5MHz frequencies were capable of 100% defect detection in all tests samples and the 5MHz frequency provided better visibility of these defects. Testing also revealed that the 2.25MHz frequency performed better at sizing 3mm and 6mm defects in GLARE panels thinner than 0.875mm whilst the 10MHz performed better at sizing defects at depths greater than 0.875mm. However, the 5MHz frequency had the best overall performance across all types of defects and samples. Nevertheless, the inaccuracies in the sizing of 3mm defects was found

to be unacceptably high, whilst the size deviation of the 6mm defects was on average lower than 40%. It was however determined that these high deviations were caused by the fact that the transducers had elevation sizes of 7mm.

Testing showed that the 10MHz frequency performed better than the other frequencies at measuring the depth of defects at depths greater than 0.875mm. However, the 5MHz transducer again performed better on average across all all types of defects and samples. Lastly, It was found that the 5MHz frequency had the best Signal-to-Noise Ratio (SNR) on GLARE panels thinner than 0.875mm whilst the 2.25MHz frequency had the best SNR on panels with thicknesses grater than 0.875mm.

It was finally concluded that a multi-frequency approach would provide very little benefit over applying a single-frequency approach with a carefully selected frequency. It was concluded that the best frequency to detect delaminations in GLARE panels with thicknesses between 0.875mm and 5.15mm was 5MHz.

Lastly, it was shown that the model adapted to determine the attenuation of ultrasonic waves in GLARE panels was excessively sensitive to variations in parameters such as density of the materials, thicknesses and velocities of the layers, causing it to be too inaccurate. Furthermore, unexplained phenomenon also occurred, which could be attributed to inappropriate assumptions. It was therefore concluded that a better model had to be developed to predict the behavior of ultrasonic waves in GLARE during pulse-echo inspections.

Acknowledgments

First of all I would like to express my deepest gratitude to Dr. Roger Groves for his guidance during the whole Master's Thesis. His knowledge, faith and dedication to this project were essential to this thesis.

I would like to thank Franc Buijsen from TiaT Europe BV for providing me with the opportunity for this thesis as well as the knowledge, training and equipment that made it possible. Furthermore, I would like to express my gratitude to Wilbert Martens, who had the patience and willingness to share his vast knowledge of Phased Array Ultrasonic with me.

I would also like to express my gratitude towards Andrei Anisimov who helped me setup the Phased Array Ultrasonics Lab and was always available for me to pick his brain. Furthermore, I would like to thank all the technicians at the ASM Laboratory at TU Delft for their assistance.

I would like to thank all my fellow master students and everyone in the NDT laboratory of the Aerospace Faculty at TU Delft for all the inspiring conversations.

Lastly, I am grateful to my family, especially my parents and my sisters for their unconditional love, support and encouragement in all my endeavors. They have guided and inspired me through my life's journey and are the reason I have been able to accomplish my goals in life.

Contents

List of Figures

LIST OF TABLES

List of Symbols and Abbreviations

Symbol	Meaning
A	Number of aluminum layers
A	Aperture
A_1	Amplitude first back wall
A_2	Amplitude second back wall
A_a	Active aperture
BW	Bandwidth
c	Velocity of longitudinal acoustic waves
C_A	Absorption coefficient
c_l	Velocity of longitudinal acoustic waves
c_n	Velocity of longitudinal acoustic waves
C_S	Scattering coefficient
d	Layer thickness
D_{min}	Minimum defect size
E	Elastic Modulus
e_m	Distance to centroid of m^{th} element
f	Frequency
F^B	Received (sensed) mechanical strain
F^i	Input mechanical strain
f_c	Center frequency
f_L	Lower frequency limit
f_n	Noise frequency
f_U	Upper frequency limit
G	Number of prepreg layers
g_x	Element gap
l_x	Element length
l_y	Element elevation
M	Number of active elements
$M_{laminate}$	Transfer matrix of a laminate
N	Number of elements
N	Signal amplitude at a reference point where no defect is present
N_{act}	Number of active elements
N_0	Near field length
p	Acoustic pressure

PV	Pressure and velocity vector
R	Reflection Coefficient
s	Distance from edge of one element to the next
S	Signal amplitude
s_x	Element pitch
SNR	Signal to Noise Ratio
T	Thickness of aluminum layer
T	Transmission coefficient
$T_{couplant}$	Transmission coefficient couplant
$t_{couplant}$	Thickness couplant
t_d	Time delay
V^i	Input voltage
V^r	Received voltage
v_s	Scanning velocity
v_z	Acoustic velocity of waves in z-direction
X	Glare grade
z_{layer}	Acoustic impedance of a layer
z_{water}	Acoustic impedance of water
Z_1	Acoustic impedance of first material
Z_2	Acoustic impedance of second material
Z_n	Acoustic impedance n^{th} layer

Greek Symbols	**Meaning**
β_g	Grating lobe angle
Δx_{res}	Scan resolution
ζ	Ratio of peak side lobe to main acoustic lobe
θ_s	Steering angle
λ	Wavelength
μ	Poisson's ratio
ρ	Density
ρ_n	Acoustic impedance
ϕ	Grain size

Abbreviations	Meaning
Avg	Signal Averaging
BCP	Batch Component Panel
BV	Barely Visible Damage
BWP	Batch Witness Panel
CCD	Charged-Coupled Device
CRP	Component Reference Panel
CWL	Component Witness Laminate
DPSM	Distributed Point Source Method
FEM	Finite Element Method
FML	Fiber Metal Laminate
GL3	Glare 3 Test Sample
GL4	Glare 4 Test Sample
MRL	Master Reference Laminate
MRP	Master Reference Panel Test Sample
NDT	Non Destructive Testing
NV	Non Visible Damage
PAUT	Phased Array Ultrasonic
PE	Pulse-Echo
PRF	Pulse Repetition Frequency
PT	Thermography
PTFE	Polytetrafluoroethylene
RSI	Rayleigh-Sommerfeld Integral
TSR	Thermographic Signal Reconstruction
UT	Ultrasonic
V	Visible Damage
VT	Vibrothermography

1
Introduction

GLARE is a glass fiber aluminum Fiber Metal Laminate (FML) that has been implemented in different aircraft such as the Airbus A340 and A380 and is gaining popularity due to its light weight and superior fatigue properties [1]. However, due to the inherent difference in material properties of laminated materials, Non-Destructive Testing (NDT) of GLARE has proven to pose a challenge. Several inspection methods such as ultrasonic C-scan inspection [2], Eddy current testing [3], X-ray radiography [4], thermography [5, 6] and shearography [7] have all proven to be able to detect different defects and damages in GLARE. These methods have several limitations that either hinders or limits their in-service use. These issues have given rise for the need to find a suitable and reliable NDT method that can perform in-service inspections of GLARE.

One method that could be used for in-service inspection of GLARE is the pulse-echo method with Phased Arrays Ultrasonics (PAUT) [8]. This method can perform inspections with a relatively small mobile unit requiring only one-side access to the material and offers the operator more control and flexibility than conventional ultrasonic inspections. The frequency of ultrasonic waves is an important parameter that influences the resolution of the image at determined depths as well as the size of the defects that can be detected. A lower frequency will have the ability of penetrating the material deeper and have reduced noise whilst a higher frequency will be capable of detecting smaller defects and will a higher resolution.

The goal of this MSc thesis is to evaluate the effects of frequency on the detection of defects and damages in GLARE in order to evaluate the benefits of a multi-frequency PAUT approach capable of reliably performing in-service inspections of GLARE in a near future. A multi-frequency PAUT transducer could combine different ultrasonic frequencies into one transducer housing, making use of the benefits of each ultrasonic frequency to detect all defects and damages in GLARE, regardless of size and location. This could provide an added level of certainty during inspections that could aid in the pass/fail decision making process. The knowledge collected during this research project will ensure that there is a clear understanding of the effects of frequency on defect and damage detection for GLARE, which can be applied in a future to develop a multi-frequency PAUT transducer capable of detecting most defects and damages reliably during in-service inspections of GLARE.

This thesis will be divided into 7 parts:

1. The first part of this thesis will introduce the reader to GLARE and will proceed to describe the defects and damages that can occur in GLARE, as well as the different Non Destructive Testing (NDT) methods that have been applied in order to detect them.
2. The second part will discuss Ultrasonic and Phased Array Ultrasonic (PAUT) theory to gain a better understanding on the physics behind it. This will provide a solid basis on which to plan and perform the tests as well as aid in the interpretation of results.
3. The third part will explain the equipment used during testing in this thesis. The properties of the equipment as well as its limitations will be explored within the context of this thesis.
4. The fourth part will walk the reader through the process of selecting the test samples, the testing methodology used as well as the criteria used to evaluate the results. Lastly, the results will be presented and discussed.
5. The fifth part of the thesis will attempt to adapt known models for the prediction of the attenuation of ultrasonic waves in GLARE for use within the context of this thesis. The results will then be analyzed and discussed.
6. Lastly, conclusions will be drawn and recommendations for further research will be made.

REFERENCES

[1] A. Vlot and J. W. Gunnink, eds., *Fibre Metal Laminates: An Introduction* (Kluwer Academic Publishers, Dordrecht, 2001).

[2] R. A. M. Coenen, *Design of a Quality Assurance System for Structural Laminates,* Ph.D. thesis, Delft University of Technology (1998).

[3] J. Sinke, *Some Inspection Methods for Quality Control and In-service Inspection of GLARE,* Applied Composite Materials **10**, 277 (2003).

[4] A. Fahr, C. E. Chapman, D. S. Forsyth, C. Poon, and J. F. Lalibert, *Nondestructive evaluation methods for damage assessment in fiber-metal laminates,* Polymer Composites **21**, 568 (2000).

[5] C. Ibarra-Castanedo, N. P. Avdelidis, E. G. Grinzato, P. G. Bison, and S. Marinetti, *Delamination detection and impact damage assessment of GLARE by active thermography,* International Journal of Materials and Product Technology **41** (2011).

[6] K. Dragan, A. Leski, A. Czulak, and W. Hufenbach, *Inspection Methods for Quality Control of Fibre Metal Laminates (FML) in Aerospace Components,* Composites Theory and Practice **4**, 272 (2012).

[7] W. Steinchen, L. Yang, G. Kupfer, and P. Mäckel, *Non-destructive testing of aerospace composite materials using digital shearography,* Proceedings of the Institution of Mechanical Engineers, Part G: Journal of Aerospace Engineering **212**, 21 (1998).

[8] W. Bisle, T. Meier, S. Mueller, and S. Rueckert, *In-Service Inspection Concept for GLARE – An Example for the Use of New UT Array Inspection Systems,* ECNDT , 1 (2006).

2

Defects, Damages and NDT of GLARE

This chapter presents a literature review on GLARE and the different types of damages and defects that can occur during the manufacturing, assembly and in-service life of GLARE. Furthermore, a study of the different NDT techniques that can detect such defects and damages is also presented in order to understand their approach and their limitations when inspecting GLARE.

2.1. GLARE

Fiber Metal Laminates (FMLs) are composite materials composed of stacked thin layers of metal bonded together by a fiber reinforced adhesive system. FMLs combine the better fatigue performance of fiber reinforced composites with the good impact damage properties of metals to provide a material with tailored properties [1]. One of the most widely used FML in the aerospace industry is GLARE, consisting of layers of S-glass fibers embedded in FM 94 epoxy adhesive and aluminum. It has found applications in the Airbus A340 as a bulkhead section in the fuselage, as part of the fuselage skin of the Airbus A380 and as the constituent material of the ECOS3 Unit Load Device, capable of containing the explosion of a bomb [1].

2.1.1. Composition of GLARE

GLARE is composed of aluminum 7475-T761 or 2024-T3 and S-glass fibers embedded in the FM 94 epoxy adhesive as depicted in figure 2.1. The aluminum layers are simply sheets with a thickness between 0.2-0.5 mm whilst the fibers embedded in the FM 94 epoxy adhesive are prepregs with a thickness of 0.127 mm. The fibers themselves are about 10 μm thick and are present in a fiber volume fraction of 59%. [1]

As with any fiber composite system, the fibers have better mechanical properties than the epoxy adhesive system. This is reflected in the strength and stiffness of each since

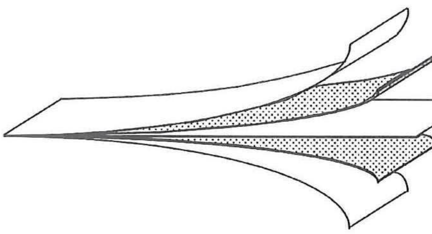

Figure 2.1: GLARE [2]

the fibers have a strength of 4000 MPa and a stiffness of 88 GPa whilst the epoxy has a strength of 50 MPa and a stiffness of 1.7 GPa. [1]

2.1.2. TYPES OF GLARE

There are 6 different grades of GLARE, categorized based on the fiber orientation and stacking order. These are summarized in table 2.1. It is important to notice that all GLARE laminates have symmetrical layups in order to avoid bending effects caused by the internal stresses that arise from unsymmetrical layups. [3]

Table 2.1: GLARE grades [1]

GLARE grade	sub	Aluminum Thickness [mm]	Metal Alloy	Prepreg orientation	Main beneficial characteristics
GLARE 1	-	0.3-0.4	7475-T761	0/0	fatigue, strength, yield stress
GLARE 2	GLARE 2A	0.2-0.5	2024-T3	0/0	fatigue, strength
	GLARE 2B	0.2-0.5	2024-T3	90/90	fatigue, strength
GLARE 3	-	0.2-0.5	2024-T3	0/90	fatigue, impact
GLARE 4	GLARE 4A	0.2-0.5	2024-T3	0/90/0	fatigue, strength in 0° direction
	GLARE 4B	0.2-0.5	2024-T3	90/0/90	fatigue, strength in 90° direction
GLARE 5	-	0.2-0.5	2024-T3	0/90/90/0	impact
GLARE 6	GLARE 6A	0.2-0.5	2024-T3	+45/-45	shear, off-axis properties
	GLARE 6B	0.2-0.5	2024-T3	-45/+45	shear, off-axis properties

GLARE laminates follow a certain standardized coding system which allows anyone to quickly know its properties. The standardized coding system is defined as follows:

$$GLARE\,X - A/G - T \tag{2.1}$$

In equation 2.1, X defines the grade (1, 2A, 2B, etc), the A defines the number of aluminum layers, the G defines the number of glass fibers layers and T defines the thickness of the aluminum layer in mm. [1]

2.1.3. PROPERTIES OF GLARE

GLARE has many advantages over other thin sheet materials. One of the properties that stands out the most is the superior fatigue properties of GLARE when compared to conventional aluminum. It has been shown that GLARE has a relatively low and constant crack propagation rate due to the fact that the fibers take part of the load over the crack when aluminum cracks form, thus resulting in longer fatigue life when compared to similar aluminum parts (up to x10 longer). Furthermore, due to the slower crack growth rate, the loss of residual strength of GLARE is much slower than for a comparable aluminum plate [3]. This proves to be a very useful property for aircraft where fatigue is an important issue.

Another important property of GLARE is its damage tolerance to impact damage. The impact damage properties of GLARE are better than those of aluminum and glass fiber composites [1, 4, 5]. Furthermore, GLARE will present dents on the surface after impact damages, allowing for visual detection of the damage. This is particularly a problem in fiber reinforced composites where this is not the case.

GLARE also has been shown to have good corrosion properties since the thin 2024-T3 aluminum sheets allow for a much faster quenching after rolling, resulting in fewer alloy elements in the crystal boundaries, thus creating better corrosion properties [5].

When compared to other glass composites, the moisture absorption rate of GLARE is very low and thus the effect on its properties is minimal [5, 6]. This is due to the aluminum layers acting as a barrier against humidity.

Another notable advantages of GLARE is its lower specific weight (10% lower than aluminum), the ability to form single and double curved panels with relative ease and the fact that the tensile strength is higher than 1.5 x yield stress. GLARE can also be machined and repaired with similar methods and equipment used to repair aluminum. GLARE also has superior fire resistance to aluminum since the glass fibers can withstand temperatures of up to 1100°C acting as a fire barrier, thus protecting the aluminum layers between the fibers from melting. [1]

2.2. DEFECTS AND DAMAGE IN GLARE

All materials that are manufactured and used in structural components are exposed to the risk of suffering defects during manufacturing or damage during the operational life.

GLARE is no exception. Therefore, this section will explore the different defects that can occur in GLARE during manufacturing and assembly as well as the damages that can occur during the operational life.

2

2.2.1. MANUFACTURING DEFECTS IN GLARE

The manufacturing of GLARE is relatively complex by nature as it has many steps and many variables which can all introduce defects during the manufacturing. The degree of severity of these defects depends on their nature, size and the consequences they might have on the finished structure. Therefore it is important to understand the types of defects that can be encountered when manufacturing GLARE. It is important to note that the defects covered here are only the ones arising from the manufacturing, meaning that the defects in the raw materials such as voids in the 'raw' prepreg or the processes that GLARE is subjected to after curing are not covered.

DELAMINATIONS

Delaminations are the separation of the plies within the laminate. In GLARE this type of defect occurs only within one layer unlike other composite laminates. There are many causes that can lead to delaminations during manufacturing, such as poor surface treatment of the aluminum sheets or inclusions [1]. Other causes for delaminations will be explored in the following sections.

INCLUSIONS

Inclusions are unwanted foreign materials or objects that have been embedded in the layup. Most of these inclusions are different kinds of sheets used during the manufacturing process that accidentally get stuck in between layers. Teflon sheets are used to facilitate removal of the vacuum bag. However, they could unintentionally get caught between layers if attention is not paid during layup. It is important to mention that the *location* of these inclusions is important for detection. If the inclusion is between the aluminum-prepreg layer, the Teflon will not bond to the aluminum and will show up in a C-scan. If the inclusion is between two prepreg layers, the Teflon will partly bond to both prepreg layers, thus making it slightly more difficult to detect with C-scan. This is represented in figure 2.2. Similar things can occur with the tape or bleeder sheets.[7]

Another important kind of insert that can occur is backing or cover sheets of prepregs. These types of sheets are used to protect the prepreg during transport and storage and should be removed before the prepreg is laid. It can occur that this sheet is not removed at all because of operator error or that the sheet is not removed properly and a piece remains attached to the prepreg. One of the biggest problems with these types of inclusions is that if they are present during the layup and are then cured, they will melt in the autoclave and fuse with the prepreg. This is especially dangerous because it can create kissing bonds between the insert and the prepreg, which are difficult to detect. [7]

There are other materials that could also be classified as inclusions such as scissors or body hair. However, all these inclusions may cause delaminations between the layers

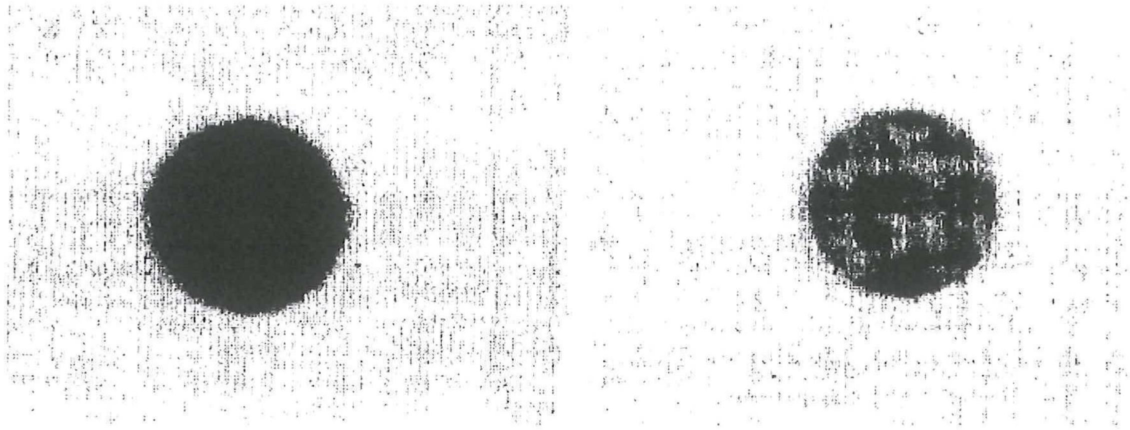

Figure 2.2: C-scan of Teflon inclusions in GLARE. Left side: Teflon insert between aluminum-prepreg layer. Right side: Teflon insert between prepreg-prepreg layer. [7]

which will greatly reduce the strength properties of the material. It is therefore important to be able to detect them.

VOIDS AND POROSITY

Voids and porosity are defined in the ASM Handbook [8] as: " [*Voids are*] air or gas that has been trapped and cured into a laminate. Porosity is an aggregation of microvoids". Voids and porosity are usually removed by applying a vacuum to the laminated structure and then subjecting it to high pressures to further remove voids and avoid porosity. These voids and pores can be as small as 1-2 μm [7]. An example of voids in glare is given in figure 2.3.

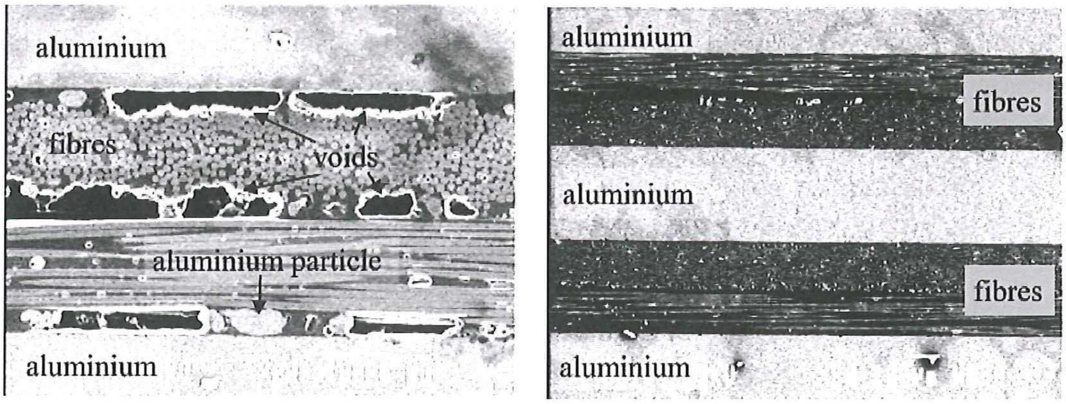

Figure 2.3: Voids between aluminum and glass fiber layers [1]

One of the main factors that causes voids is process control, as it has been shown that the control of the curing cycle greatly affects the void content of the finished GLARE panels [1, 9]. Other common causes for voids and porosity are improper storage of the prepregs as they can absorb humidity which will then cause voids when the prepreg is cured, overaging of the adhesive layer, or insufficient thickness in the adhesive film used [1].

These voids cause an increase in moisture absorption which will eventually cause a significant reduction in the durability of the GLARE panel [1]. Furthermore, these small voids act as stress concentrations, making them weak spots for either delaminations and/or crack formation [1, 8, 9].

DISBONDS

Disbonds are defects that occur because there is a lack of bonding between two surfaces or layers. These can occur at splices where a lack of adhesive at the splice location might prevent proper bonding from occurring. Poor fitting of parts as well as poor process control can also cause disbonds. [1]

One special type of disbond are the so called 'kissing bonds'. These types of disbonds occur when two surfaces are in close contact but without any actual bonding. Since there is no bonding, they cannot transfer loads. However, due to the close proximity of the surfaces, these defects are difficult to find with conventional ultrasonic methods, making them very dangerous defects [10]. New UT inspection methods, such as those used by Yan et al., have proven to be able to detect kissing bonds in bonded aluminum pieces with conventional ultrasonics by examining the nonlinearity of the ultrasonic signal [11]. Other techniques such as Digital Image Correlation (DIC) have also been successful in detecting kissing bonds in composite materials in laboratory environment [12]. However, all these methods are experimental and are not used in the field [11, 12] This type of disbond can occur due to inclusions (as explained previously), or poor process control.

RESIN VARIATIONS

One of the defects that can occur during manufacturing of GLARE is having an uneven distribution of resin throughout the panel. If the prepreg has dry spots or uneven distribution of the resin, it may cause voids or resin rich areas, both of which are prone to delaminations. Other causes for such defects can be the improper use of autoclave tools as well as wrong cure cycles [1, 7].

SURFACE DEFECTS

As the name explains, surface defects are defects that occur at the surface of the laminate. These defects usually are small dents or small scratches that usually occur due to poor cleaning of either the mold or the aluminum sheets. They are relatively common and do not usually pose a mechanical problem to the laminate but might become problematic for uses where smooth surfaces are required, such as for aerodynamic parts. [7]

CONFIGURATION DEFECTS

Configuration errors are those made during the lay-up process. These are mainly errors introduced by the operator and can include:

- Wrong ply alignment or orientation - Plies are positioned in the wrong direction or are moved during curing of the laminate
- Wrong ply stacking - The order of the stacking is not followed, leading to wrong orientations at the wrong ply layer or an excess or shortage in the number or plies

- Incorrect positioning - Plies are not properly positioned in the mold or at splicing locations. Very important for splicing
- Wrong sizing - sizing of plies/laminate/thickness is not according to requirements

All these types of defects will produce parts with undesired mechanical properties. As mentioned, there are systems to aid in this part of the manufacturing process, but mostly depend on the skill and concentration of the person making the layup. [7]

2.2.2. POST-MANUFACTURING AND ASSEMBLY DAMAGE IN GLARE

After the panels of GLARE have been cured in the autoclave, the end products are flat or curved panels that might still require additional work in order for them to enter service. Usually they require post-manufacturing processing techniques such as forming or hole drilling for the part to be usable in a structure. The damage that these processes might introduce to the material will be reviewed below.

DELAMINATIONS

Delaminations are very common damages that are introduced during post-manufacturing processes. On many occasions GLARE panels have to be milled to the right shape and size and holes have to be drilled to allow for the assembly of (sub)parts. When GLARE is machined or drilled, the laminate is subjected to forces perpendicular to the laminate, potentially causing delaminations as shown in figure 2.4. These types of delaminations are usually caused by the excessive wear of tools or when the wrong process control parameters such as feed force are used [13]. It is therefore important to inspect the edges of panels or drilled holes to ensure there are no delaminations.

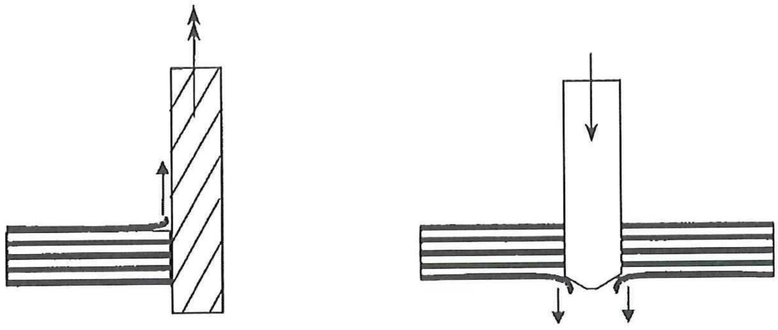

Figure 2.4: Delamination occuring during milling (left) and drilling (right) of GLARE [13]

GLARE can also be formed in similar manners to those of conventional metals in order to produce parts such as stringers or curved panels. However, GLARE's formability is limited by many factors such as the low failure strain of the fibers. If not performed properly , the shear stresses between the metal and composite layers introduced during these forming processes will be too high, causing delaminations and disbonds. [13]

BUCKLING

If the metal sheets used in GLARE are very thin (≤0.3mm), then they can experience buckling during the bending part of the forming process. [13]

MATRIX CRACKS

Micro-cracking may occur during the forming process of GLARE. It is important to notice that micro-cracking in the matrix does not lead to total failure of the laminate. [13]

SURFACE DAMAGE

During the post-manufacturing processes, GLARE panels are still exposed to surface damage such as scratches, cuts or indentations. Again, scratches and indentations can occur if the panels are not handled with care during transport or when being set up for these post-manufacturing processes. [7]

2.2.3. IN-SERVICE DAMAGE IN GLARE

DELAMINATION

Delaminations are one of the most common damage types that can occur during operational lifetime of GLARE. Delaminations can occur due to common damage types such as impact damage [4] and fatigue damage [3]. GLARE can also suffer from delamination due to thermal effects such as long time exposure to high temperatures (depending on resin, but as 'low' as 188°C) [14], freeze/thaw stressing due to moisture expansion or thermal spikes [1].

SURFACE DAMAGE

Surface damage such as cuts, scratches and dents are common damages that GLARE can suffer when in-service. Cuts and scratches may occur due to mishandling or from flying debris. Dents may occur due to impact damage or mishandling (such as personnel stepping in no-step regions). Abrasion of the surface may also occur due to erosion from prolonged exposed to rain and/or grit. Surface oxidation and corrosion may also occur in GLARE if the material is struck by lightning, overheated or exposed to moisture. [1, 3]

PENETRATION DAMAGE

Penetration in GLARE can occur due high velocity impacts or battle damage. Furthermore, penetration could also occur due to mishandling of ground or maintenance operators, where improper operation of equipment such as fork lifts could cause penetration damage. These can also cause edge delaminations in the same manner as drilling [1].

MATRIX CRACK

Cracking of the cured resin matrix may occur in GLARE if it is exposed to repeated low-velocity impacts [4] as well as fatigue loading [3]. These often occur before the cracking of the aluminum layers and may occur parallel or perpendicular to the fiber direction . Moisture absorption by the matrix will also cause it to degrade faster and stimulate crack growth [3].

ALUMINUM CRACK

Cracks in the aluminum layer may occur during the operational life-time of GLARE due to fatigue effects [3] as well as repeated impact damages [4]. An example of aluminum cracking due to impact damages can be seen in figure 2.5. These type of cracks will expose the matrix to moisture, degrading it faster.

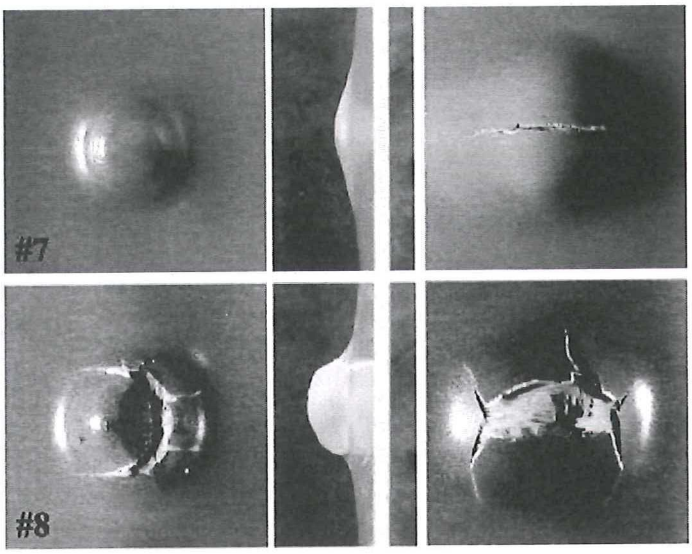

Figure 2.5: Aluminum cracking in GLARE due to repeated impact damage as seen from the front (left), side (middle) and back (right) sides [4]

HOLE ELONGATION

Hole elongation can occur when holes are overloaded. This usually occurs at bolted or riveted joints and can cause bearing failures, local buckling, deformations, and exposure of the matrix materials to moisture. [1]

2.2.4. OVERVIEW OF DEFECTS AND DAMAGE IN GLARE

All the different defects and damages present through the manufacturing, post-manufacturing and assembly and the in-service life of GLARE are presented in table 2.2.

2

Table 2.2: Defects and damage overview

Defects & Damages	Cause	Consequence
Manufacturing		
Delaminations	Poor surface treatment, inclusions, voids, resin variations	Reduction of mechanical properties
Inclusions	Poor layup process control	Delaminations, kissing bonds
Voids and porosity	Poor process control (curing), poor prepreg storage conditions	Increase moisture absorption, decrease durability, delaminations, cracks
Disbonds	Poor fitting of parts, poor process control	Kissing bonds, strength reduction
Resin variations	Prepreg dry spots, improper autoclave tools, wrong cure cycle	Delaminations
Surface defects	Poor cleaning of aluminum layer or mold	Small dents, scratches, unsmooth surface
Configuration defects	Poor layup process control	Wrong ply alignment, orientation, stacking, incorrect positioning, sizing. Undesired mechanical properties
Assembly		
Delaminations	Improper milling, drilling, forming	Reduction of mechanical properties
Buckling	Improper forming	Failure
Matrix cracks	Improper forming	Reduction of mechanical properties
In-Service		
Surface damage	Mishandling	Small dents, scratches, unsmooth surface
Delaminations	Impact damage, fatigue damage, thermal effects	Reduction of mechanical properties
Surface damage	Mishandling, impact damage, lightning strike, rain/grit erosion, moisture	Small dents, scratches, unsmooth surface, oxidation, corrosion, holes
Penetration damage	High velocity impact damage, mishandling	Holes, reduction of mechanical properties
Matrix cracks	Impact damage, fatigue loading, moisture absorption	Reduction of mechanical properties
Aluminum crack	Impact damage, fatigue loading	Increase moisture absorption, decrease durability, reduction of mechanical properties
Hole elongation	Overload	Bearing failure, local buckling, deformations, exposure of matrix material to moisture

2.3. NON-DESTRUCTIVE TESTING OF GLARE

Fiber Metal Laminates like GLARE pose a special challenge for Non-Destructive Testing (NDT) due to their highly anisotropic nature and the very different properties of each layer. Various methods such as active thermography, Eddy currents, shearography and ultrasonic (UT) through transmissions are used to inspect GLARE panels. All these methods will be reviewed and discussed in this section. The distinction should be made that the methods discussed here are NDT methods used to inspect the final GLARE product (after curing), and not to monitor processes such as the curing process.

2.3.1. ULTRASONIC THROUGH TRANSMISSION

Ultrasonic inspection consists of sending ultrasonic waves (with frequency f>50 kHz) through a material. When these waves encounter a change in the material (delamination, entrapped air, different material), part of the acoustic wave will be reflected. Due to the relatively small wavelengths of UT waves, small defects can be found using ultrasonic inspection. In the Pulse-Echo (PE) method, the reflected sound (echo) will be detected by the same UT transducer that produced the sound [15], as shown in the left side of figure 2.6. If there is a discontinuity, the sound will reflect 'sooner' than expected. Pulse-echo ultrasonic inspections can create A-scans (amplitude of reflected UT signal vs. time or distance traveled), B-scans (cross-sectional representation of reflected UT signals crossing a defined gate) and C-scans.

In through transmission (known as C-scan), the ultrasonic wave is sent by one transducer and received by a second transducer on the other side of the specimen as shown in figure 2.6. As mentioned, the changes in material will reflect the sound, which in *through transmission* will result in the attenuation or even blockage of the ultrasonic wave received by the second transducer [7]. Typically an attenuation of the ultrasonic wave below -6dB is considered as a damage/defect [16].

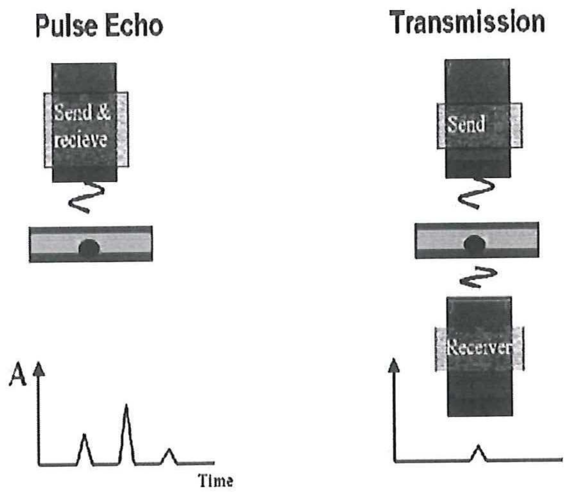

Figure 2.6: Left: Pulse-echo. Right: Through transmission [17]

Ultrasonic (UT) through transmission is the most common method of inspection of GLARE [1]. To create a C-scan, the whole panel has to be inspected and the attenuations for each position recorded. These attenuations can then be matched to a color scale to make an image showing the locations of damage as seen from a top view.

One of the biggest differences between FMLs such as GLARE and metals or even composites is the requirement for a different type of reference system when performing Quality Assurance. In metals and some composites, the interaction of the acoustic wave with the material is a function of the depth. However, due to the reflections that occur when the wave crosses from the aluminum to the fiber/epoxy composite in GLARE, interference may occur and the signal is difficult to interpret. [7, 17]

Coenen [7] developed a reference system to be applied with the UT C-scan at TU Delft. This reference system utilized 5 different reference panels called the Master Reference Laminate (MRL), the Batch Witness Panel (BWP), the Component Witness Laminate (CWL) and a Component Reference Panel (CRP) and a Batch Component Panel (BCP). The MRL is a part of the material used for qualification and is the reference to which other reference laminates are compared to. The full description of the reference system can be found in [7].

Ultrasonic C-scan can detect many types of damages such as delaminations, voids/-porosity, inclusions, configuration defects (ply orientation) and cracks [7]. A measurement accuracy of 2 mm square has been achieved in FML with UT C-scan [18]. It however cannot provide information regarding the depth at which the damage is located.

One of the disadvantages of C-scan is that it is not mobile and is therefore mostly used to detect defects in manufacturing for quality assurance rather than in-service inspections. The reason it cannot be used for in-service inspection is that it requires two-side access to the material and this is not always possible during inspections.

Dragan et al. [16] successfully inspected FML using other ultrasonic inspection methods such as single transducer pulse-echo inspections and air coupled ultrasonic inspections. The panel tested was an FML composite consisting of 3 layers of 2024T3 aluminum layers and 2 T700GC-carbon fiber/epoxy prepregs with polytetrafluoroethylene (PTFE) and aluminum inserts. The thicknesses varied between 0.02 mm - 0.125 mm and were located between the aluminum and epoxy layers as well as the in the middle of the epoxy. The size of the defects was varied between 2.5mm and 9.5mm in diameter. Pulse-echo ultrasonic inspection proved to be better at finding defects in FML as it was able to find 70% of the damages whilst air coupled was only able to find 50% of the damages. The investigators concluded that the lower performance of air-coupled UT was due to the lower resolution of the air-coupled UT inspection. However, both methods were incapable of accurately finding aluminum inserts.

Lastly, Bilse et al. [19] investigated the use of PAUT transducers for in-service non-scheduled inspections for GLARE. They determined that frequencies between 1MHz and

2.25MHz were to be used for undisturbed plates whilst 1MHz was to be used for bonded doublers. They were capable of inspecting disbonds in bonded stringers, delaminations in dents and defects in spliced areas. However, no mention was made on minimum detectable size or accuracy of the measurements.

2.3.2. Eddy Currents

Eddy current testing uses electromagnetic induction to detect defects in a conductive material. This method consists on placing a coil with alternating current near the conductive surface (with the windings of the coil parallel to the surface) of an object in order to create changing magnetic fields. These changing magnetic fields will cause the current to flow in circular loops perpendicular to the magnetic field. These currents, known as eddy currents, will produce their own magnetic field opposing the magnetic field from the coil. [17]

When the eddy currents encounter an anomaly that obstructs them, the primary magnetic field will change, causing a change in the eddy currents and their magnetic field. These changes will cause a change in the impedance of the coil which will cause an electric potential, which can be seen as a change in voltage. [17]

Eddy currents tend to have the highest density at the surface and their penetration in FML is problematic as the composite layers are not conducting. Furthermore, there is a phase and amplitude lag between the surface layers and the deeper layers which allows the inspector to determine the defect depths (in layers, not mm) and sizes [17].

It has been shown that eddy current testing can find cracks of 3 mm in the aluminum (not in the composite) layers of GLARE of lap joints of 3/2 layups with a Probability of Detection (POD) of 90% and practically 100% for bigger cracks [17]. It has also been found to be able to detect cracks in the second layer of aluminum with an accuracy of 1 mm [18]. Eddy currents have proven to be unsuccessful at finding delaminations but capable of mapping corrosion between the layers [18].

One of the advantages of the eddy current testing is that it can be used for in-service inspection since the equipment is mobile and only requires single sided access to the material. The types of defects they can detect are however very limited.

2.3.3. X-ray Radiography

Radiography is a technique in which a material is exposed to X-rays which will penetrate the material and strike a radiographic film or camera. The photons in these X-rays will interact with the materials particles, which will absorb or scatter some of the photons energy. This loss of energy is measured as an attenuation and is dependent on the geometry of the material as well as the material's properties, such as thickness and density. The attenuation will cause photons to strike the radiographic film with different energies depending on the material they traveled through, creating an image which can depict changes in the material. [8]

When a discontinuity such as a delamination is encountered, the attenuation of the photons at the location of the discontinuity will change, causing the energy of the photon to change. When these photons impact the radiographic film, they will do it with a different energy that will then be shown as a different color in the film, showing the location and size of the damage, as can be seen in figure 2.7. Penetrants can be used to obtain better contrast in images. [8]

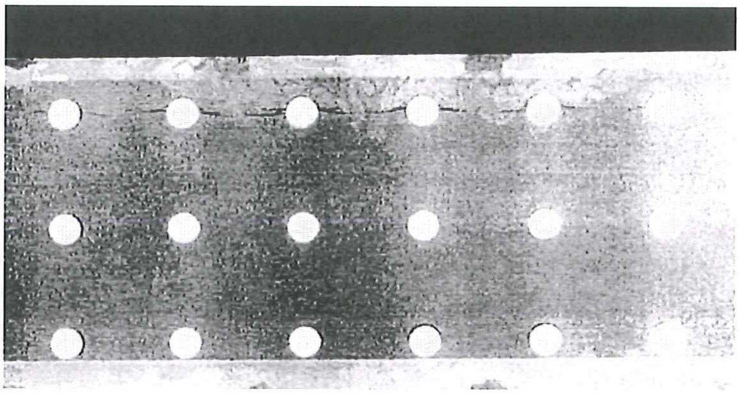

Figure 2.7: X-ray image of a GLARE-3 panel showing fatigue cracks and corrosion [18]

Test conducted using proprietary penetrant enhanced X-ray radiography in GLARE 3 showed that penetrant enhanced X-ray radiography could be suitable for imaging of delaminations caused by impacts or fatigue in laboratory environments. It was also determined that penetrant enhanced X-ray radiography underestimated the size of these delaminations by as much as 35% due to the penetrant not covering all the crack. X-ray radiography also proved to be able to detect cracks near rivet holes as well as corrosion. [18]

2.3.4. ACTIVE THERMOGRAPHY

Active thermography consists of stimulating a material sample with energy, such as optical, mechanical or electromagnetic energy, and recording the resulting thermal signatures with an infrared camera at different intervals to create a thermogram (thermal map). When optical energy is used to stimulate the material, the heat will be produced at the surface and will travel through the specimen but will reflect when it encounters a defect. Mechanical energy on the other hand will create heat at the defect interface, from where it will travel to the surface. Lastly, electromagnetic energy can be applied to the internal electro-conductive layers, which will in turn create eddy currents at the surface. An example of delaminations caused inserts in GLARE detected by means of thermography can be seen in figure 2.8.[20]

Ibarra-Castanedo et al. [20] have shown that thermography (PT) can successfully detect (in a qualitative manner) delaminations caused by inserts (as small as 2.5x2.5mm) as well as indicate the severity of damage in impact damage in GLARE. PT also proved useful for detecting paint surface scratches. This was done by painting the surface to increase its emissivity and using thermographic signal reconstruction (TSR) since the

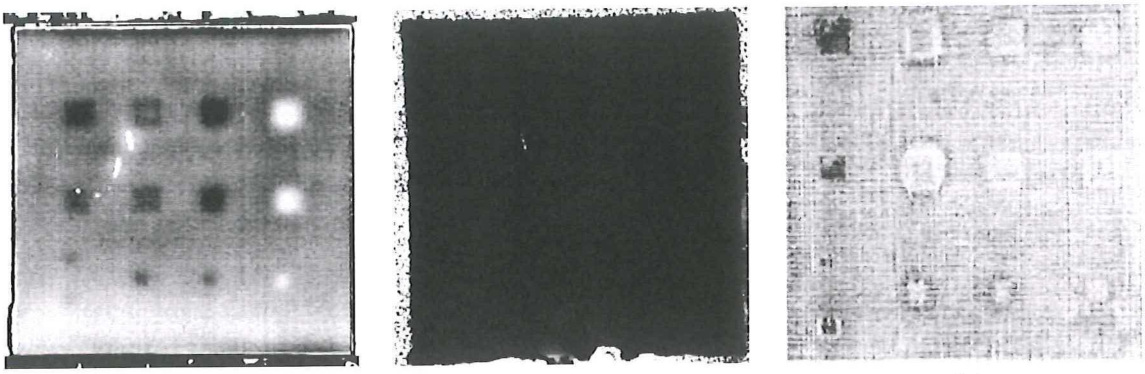
(a) (b) (c)

Figure 2.8: Delamination caused by inserts in GLARE as detected by (a) pulsed thermography (b) vibrothermorgraphy (c) ultrasonic C-scan (15 MHz) [20]

infrared signature was affected by non-uniform heating as well as environmental reflections and emissivity variations at the surface. They also showed that vibrothermography (VT) could be used to detect delaminations caused by inserts but had limited detection of impact damage in GLARE.

Dragan et al. [16] found that flash thermography using Time Signal Reconstruction was less successful at detecting inserts than X-ray computer tomography (100% damages detected) pulse-echo ultrasonics (70% damages detected) and air coupled ultrasonics (50% damages detected) in FML since it could only detect 30% of the damages. It is worth noting that carbon fiber-aluminum FML were used in their testing and that only the polytetrafluoroethylene film inclusions were detected, whilst the aluminum inserts went undetected. The poor results were attributed to the high thermal emissivity of the aluminum layers as well as the high directional thermal expansion of the carbon fibers.

2.3.5. DIGITAL SHEAROGRAPHY

In digital shearography, an object is illuminated by an expanded laser beam from which the light will reflect onto an image plane of an image shearing CCD (Charge-Coupled Device) camera. The intensity pattern of the light field is recorded as an interferogram of the material surface in an unstressed and a stressed state after which the intensities of both states can then be compared. If there is a material defect, the stressed material will have quite a different interferogram, causing it to show discontinuities and 'butterfly' patterns when the images are compared.

Steinchen et al. [21] determined that cracks of a depth of about 0.3 mm and a length of 45 mm created on the top and bottom aluminum layers could be detected by shearography when a thermal loading caused by a temperature change of $30°C$ or $40°C$ was applied on GLARE 3/2. They determined that when the surface observed was reduced in size, a higher resolution was obtained and delaminations could be distinguished from the cracks.

2.3.6. OVERVIEW AND DISCUSSION OF NDT METHODS FOR GLARE

The different Non-Destructive Inspection methods that have been used to inspect GLARE and the defects and damages they can detect are presented in table 2.3. It is important to notice that most of these inspection methods are not used to inspect GLARE by the industry and are merely a scientific effort to determine their viability.

Table 2.3: NDT methods to inspect GLARE and the types of defects/damages they can detect

NDT Method	Damage/Defects Detected
Ultrasonic C-scan	Delaminations, voids, porosity, inclusions, configuration defects, cracks
Ultrasonic Pulse-Echo	Delaminations, voids, porosity, inclusions, cracks
Eddy Current	Cracks in aluminum layers and corrosion between layers
X-ray Radiography	Delaminations, inclusions, corrosion, cracks
Active thermography	Delaminations, inclusions, surface scratches
Digital Shearography	Cracks in aluminum layers and delaminations around aluminum cracks

Of the NDT methods capable of inspecting GLARE, the ultrasonic C-scan seems to be the most widely used and the only one used by the industry since it is the NDT method used for Quality Assurance of manufactured GLARE panels [1, 7]. This system is however not suitable for in-service inspections due to the need for two-side access to the structure and precise positioning of the transducers.

Eddy currents are very limited in their detection since they can only detect cracks in aluminum layers and corrosion between layers of GLARE. Digital shearography has a similar drawback since it can only detect cracks in the aluminum layers and delaminations around those aluminum cracks. Eddy current however offers the advantage of a small portable system, allowing it to perform in service inspections in GLARE. Portable shearography systems are also available but are typically larger in size.

X-ray radiography in GLARE requires penetrants to obtain a good contrast and be able to detect damage. This could pose several problems since the penetrant has to reach and fully cover the damaged areas in order for these damages to show, making it a slightly less reliable method. Furthermore, if the penetrant cannot be removed, it could adversely affect the mechanical properties of GLARE. Active thermography has similar shortcomings since it requires painting of the surface to increase the emissivity of the aluminum surface. This could be problematic for NDT in-service inspections if the paint could not be easily removed.

It can be concluded that ultrasonic C-scan offers the best results for NDT of GLARE. It therefore offers the best way to validate results during the course of the thesis.

2.4. CONCLUSION

This chapter presented the defects and damages that can occur in GLARE and the methods that have been used to detect them. It can be concluded that there is currently no suitable method to perform in-service inspections of GLARE, leaving a gap that could be filled by PAUT. However, a better understanding of the effects of the frequencies of PAUT in the detection of different defects and damages is essential to allow for its application by the industry.

It was also found that many different NDT methods could be used to detect defects in GLARE. The only NDT method that was found to be used by the industry to detect damage in GLARE panels was ultrasonic through-transmission C-scans. It is therefore wise to use such a method to validate the results.

REFERENCES

[1] A. Vlot and J. W. Gunnink, eds., *Fibre Metal Laminates: An Introduction* (Kluwer Academic Publishers, Dordrecht, 2001).

[2] T. Beumler, *Flying GLARE,* Ph.D. thesis, Delft University of Technology, Delft (2004).

[3] R. C. Alderliesten and J. J. Homan, *Fatigue and damage tolerance issues of Glare in aircraft structures,* International Journal of Fatigue **28**, 1116 (2006).

[4] F. D. Morinière, R. C. Alderliesten, M. Y. Tooski, and R. Benedictus, *Damage evolution in GLARE fibre-metal laminate under repeated low-velocity impact tests,* Central European Journal of Engineering **2**, 603 (2012).

[5] C. A. J. R. Vermeeren, *An Historic Overview of the Development of Fibre Metal Laminates,* Applied Composite Materials **10**, 189 (2003).

[6] B. Borgonje and M. S. Ypma, *Long Term Behaviour of Glare,* Applied Composite Materials **10**, 243 (2003).

[7] R. A. M. Coenen, *Design of a Quality Assurance System for Structural Laminates,* Ph.D. thesis, Delft University of Technology (1998).

[8] *ASM Handbook, Volume 21, Composites* (ASM International, 2001).

[9] S. Y. Park, W. J. Choi, and H. S. Choi, *A comparative study on the properties of GLARE laminates cured by autoclave and autoclave consolidation followed by oven postcuring,* The International Journal of Advanced Manufacturing Technology **49**, 605 (2009).

[10] P. B. Nagy, *Ultrasonic detection of kissing bonds at adhesive interfaces,* Journal of Adhesion Science and Technology **5**, 619 (1991).

2

[11] D. Yan, B. W. Drinkwater, and S. A. Neild, *Measurement of the ultrasonic nonlinearity of kissing bonds in adhesive joints,* NDT & E International **42**, 459 (2009).

[12] R. L. Vijaya Kumar, M. R. Bhat, and C. R. L. Murthy, *Evaluation of kissing bond in composite adhesive lap joints using digital image correlation: Preliminary studies,* International Journal of Adhesion and Adhesives **42**, 60 (2013).

[13] J. Sinke, *Manufacturing of GLARE Parts and Structures,* Applied Composite Materials **10**, 293 (2003).

[14] G. Zhu, Y. Xiao, Y. Yang, J. Wang, B. Sun, and R. Boom, *Degradation behavior of epoxy resins in fibre metal laminates under thermal conditions,* Journal of Shanghai Jiaotong University (Science) **17**, 257 (2012).

[15] W. Martens, *Phased Array Sabca Training,* Tech. Rep. (TiaT Europe B.V., Roosendaal, 2014).

[16] K. Dragan, A. Leski, A. Czulak, and W. Hufenbach, *Inspection Methods for Quality Control of Fibre Metal Laminates (FML) in Aerospace Components,* Composites Theory and Practice **4**, 272 (2012).

[17] J. Sinke, *Some Inspection Methods for Quality Control and In-service Inspection of GLARE,* Applied Composite Materials **10**, 277 (2003).

[18] A. Fahr, C. E. Chapman, D. S. Forsyth, C. Poon, and J. F. Lalibert, *Nondestructive evaluation methods for damage assessment in fiber-metal laminates,* Polymer Composites **21**, 568 (2000).

[19] W. Bisle, T. Meier, S. Mueller, and S. Rueckert, *In-Service Inspection Concept for GLARE – An Example for the Use of New UT Array Inspection Systems,* ECNDT , 1 (2006).

[20] C. Ibarra-Castanedo, N. P. Avdelidis, E. G. Grinzato, P. G. Bison, and S. Marinetti, *Delamination detection and impact damage assessment of GLARE by active thermography,* International Journal of Materials and Product Technology **41** (2011).

[21] W. Steinchen, L. Yang, G. Kupfer, and P. Mäckel, *Non-destructive testing of aerospace composite materials using digital shearography,* Proceedings of the Institution of Mechanical Engineers, Part G: Journal of Aerospace Engineering **212**, 21 (1998).

3

ULTRASONIC THEORY

This chapter will present ultrasonic theory with the intention of providing a solid basis of understanding to aid in the course of this thesis. It is important however to realize that PAUT is a variation of conventional UT and therefore PAUT and conventional ultrasonics are essentially governed by the same physical principles. Therefore basic theory that applies to both conventional UT and PAUT will be presented first, whilst PAUT specific theory will be presented after.

3.1. PHYSICAL PRINCIPLES

As explained in section 2.3.1, ultrasonic inspection methods make use of mechanical waves traveling through a medium in order to non-destructively detect changes and irregularities within the medium. When waves encounter an anomaly or discontinuity, such as a change in material properties, the wave will reflect sooner than expected, indicating that there is a change in material properties.

3.2. ULTRASONIC WAVE GENERATION

Ultrasonic waves are created by piezoelectric crystals cased inside an ultrasonic transducer. Using the reverse piezoelectric effect, the piezoelectric material can be excited with an electrical charge of voltage V^i to mechanically strain it, which in turn will create mechanical strains (waves) F_i, as can be seen in figure 3.1a. Conversely, the sensing of these mechanical waves uses the direct piezoelectric effect of the piezoelectric crystal, where mechanical strains F^B on the piezoelectric element are converted to electrical energy (voltage) V^r to recover information on the interaction of the mechanical wave with the material, as seen in figure 3.1b.

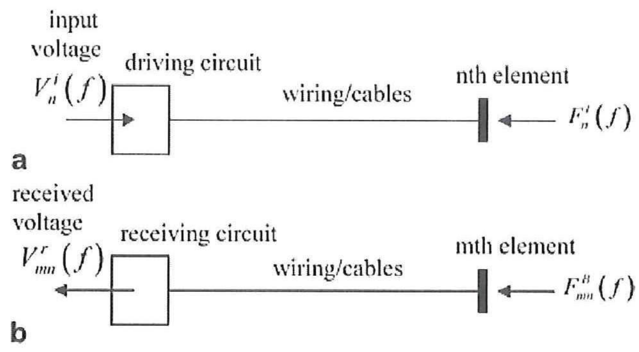

Figure 3.1: Generation and reception of ultrasonic waves [1]

3.3. ULTRASONIC WAVES

Waves are disturbances that occur in space and can transfer energy [2]. Waves are characterized by several important parameters such as the the wavelength λ and the amplitude A, as depicted below in figure 3.2.

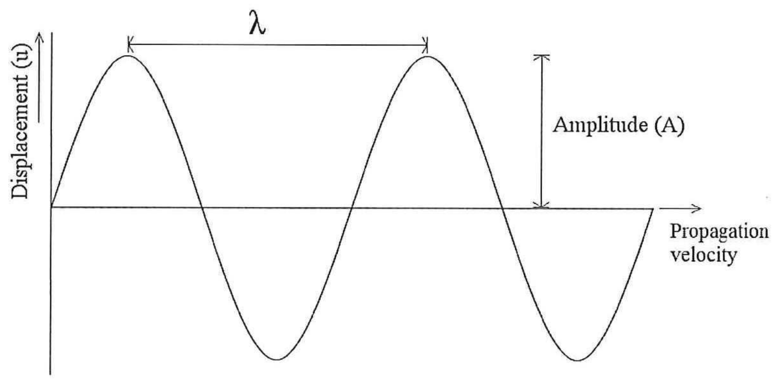

Figure 3.2: Wave properties

One property commonly used to describe waves is the frequency f, which defines the number of complete oscillations that the wave can perform in one unit of time. The frequency is related to the wavelength λ as follows:

$$f = \frac{c}{\lambda} \tag{3.1}$$

Where c is velocity of the wave. The propagation of ultrasonic signals is done by means of several different types of ultrasonic waves [3]. Two of the most common types of waves are the longitudinal (compression) wave and the transverse (shear) wave [3]. In longitudinal waves, the particle motion is parallel to the waves propagation direction whilst in transverse waves, the particle motions occur perpendicular to the propagation direction of the wave, as shown in figure 3.3.

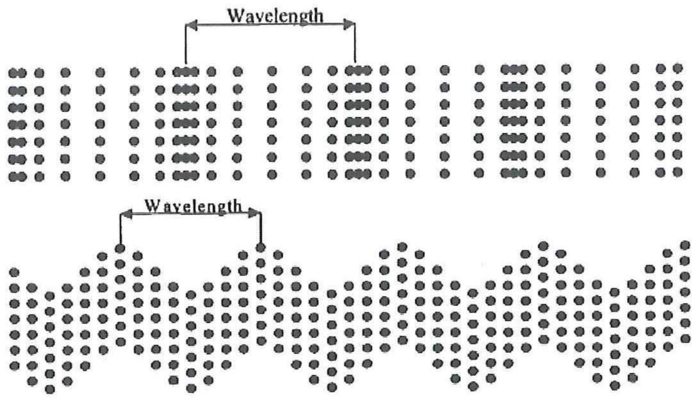

Figure 3.3: Longitudinal wave (top) and transverse wave (bottom) [3]

Longitudinal waves may travel through solids, liquids and gasses, whilst transverse waves can only travel through solids since they require a material that has a shear strength [3]. In 0° incident wave inspections, only longitudinal waves occur. However, when performing inspections at an angle, there will be a wave mode conversion and both longitudinal and transverse waves will occur simultaneously. If the angle is increased even further, first only transverse waves are present then surface waves can also occur, as shown in figure 3.4. In thinner plates, special types of transverse waves may occur, such as Rayleigh and Lamb waves. For the inspection of GLARE, only longitudinal waves and 0° inspections will be conducted, and therefore only longitudinal waves will be used.

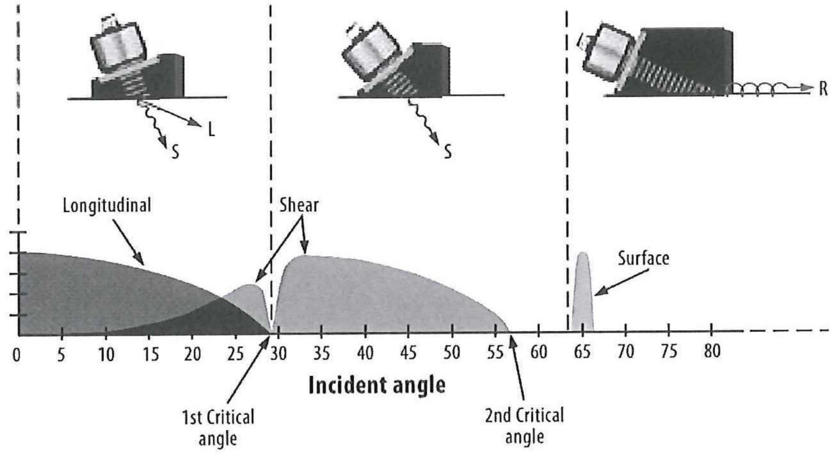

Figure 3.4: Relative amplitude of different wave types as a function of the angle of incidence [4]

Ultrasonic waves are a special type of waves that have frequencies between $20kHz$ and $1GHz$ [2].

The velocity of acoustic longitudinal waves c_l in a material is a function of various material properties such as the density ρ, the modulus of elasticity E and the Poisson's ratio μ

and can be expressed as [5]:

$$c_l = \sqrt{\frac{c_{11}}{\rho}} = \sqrt{\frac{E(1-\mu)}{\rho(1+\mu)(1-2\mu)}} \tag{3.2}$$

Equation 3.2 can be used to determine the velocity of sound in materials of which the mechanical properties are known with certainty.

3

3.4. FREQUENCY

The frequency of the acoustic wave generated by UT and PAUT transducers have a great impact on the inspection and is therefore crucial to select the optimum frequency when performing an inspection [6]. The frequency f is directly related to the wavelength λ of the acoustic wave by the following relation:

$$\lambda = \frac{c}{f} \tag{3.3}$$

Where c is the velocity of sound in the material being tested.

Higher frequencies result in smaller wavelengths and therefore tend to provide higher sensitivity (ability to detect small discontinuities) and better axial resolution (ability to distinguish between two discontinuities that are close together) due to the smaller wavelengths having an increased chance of colliding with a defect and therefore finding it. However, higher frequencies might have such a small wavelength that they are reflected and scattered at the grain boundaries, thus making penetration into the material and inspection very difficult due to high attenuation. The frequency of a transducer is essentially determined by the material and the thickness of the crystal, where the thickness is selected so the crystal resonates at the desired frequency.[6]

It is important to note that UT and PAUT transducers do not create acoustic waves at one single frequency, but create vibrations within a bandwidth with lower and upper frequency limits, as shown in figure 3.5. The lower and upper limits are measured at $-6dB$ (50% signal amplitude) and expressed as a percentage of the center frequency. The center frequency f_c and the bandwidth are defined as [7]:

$$f_c = \frac{f_U + f_L}{2} \tag{3.4}$$

$$BW = \frac{f_U - f_L}{f_c} \tag{3.5}$$

Where f_U and f_L are the upper and lower frequency limits measured at $-6dB$. The bandwidth of a transducer is mainly affected by the material of the piezoelectric crystal, the damping material placed behind the crystal to dampen vibrations and the electrical network connecting the transducer with the instrument [5].

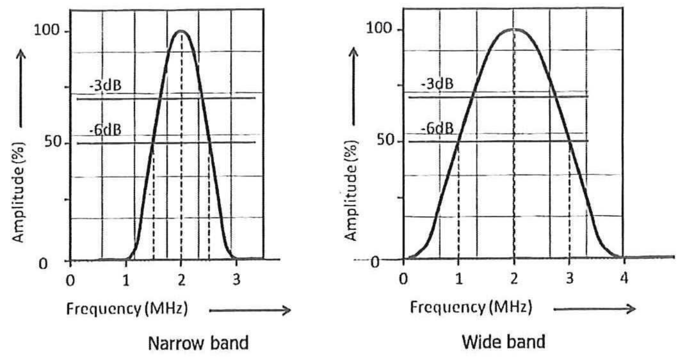

Figure 3.5: Narrow and broad bandwidth [5]

3

A narrow (smaller) bandwidth, as shown in figure 3.5, usually has a better sensitivity than broad bandwidths and are usually better for the detection of smaller defects. However, broad bandwidths generally have better axial resolution and has proven to have higher signal-to-noise ratios in anisotropic materials such as welds. This occurs due to the material acting as a natural frequency filter, filtering out undesired frequencies [5]. It is worth mentioning that PAUT transducers tend to have relatively broad bandwidths (> 60%) due to the nature of their design [8].

Due to the anisotropic nature of GLARE, PAUT transducers with relatively broad bandwidths should be beneficial when performing PAUT inspections.

3.5. ATTENUATION

Attenuation in ultrasonics is defined as the loss of signal due to various physical effects caused by absorption and scattering [9]. Many factors such as the inspection frequency f, the wave type and material properties such as the the elasticity modulus E, density ρ, lattice and grain size Φ have a great effect on the overall attenuation of the UT signal [9, 10]. It is therefore very important to understand attenuation and its effects in UT and PAUT inspections.

Absorption is a phenomenon in which energy is lost due to friction. Friction is created between atoms when they start vibrating, causing the mechanical energy of the vibrating atoms to be partly converted into thermal energy (heat), thus losing some energy. It is logical then that absorption is greatly dependent on frequency since atoms will vibrate differently at different frequencies. The higher the frequency, the faster the atoms vibrate, thus the higher the energy lost due to friction. [10]

Scattering on the other hand is caused by the reflection and deflection of acoustic waves at grain boundaries and crystal faces as shown in figure 3.6, causing the acoustic wave to scatter, thus losing energy.

The two parameters that have the biggest influence regarding scattering are the frequency f and the grain size Φ of the material. It is the relationship between the wave-

3

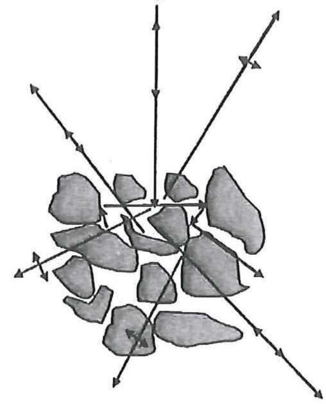

Figure 3.6: Scattering of an acoustic wave at the grain boundaries [10]

length λ and the grain size Φ that determines the type of scattering that occurs. These are classified as [9]:

- Rayleigh scattering when $\Phi < \lambda$
- Stochastic scattering when $\Phi \approx \lambda$
- Diffuse scattering when $\Phi > \lambda$

Rayleigh scattering is a type of scattering that occurs when the the wavelength is much bigger than that of the grains in the material being inspected, whilst stochastic scattering is caused by a resonance effect and occurs when the wavelength of the acoustic wave is similar to that of the particles [11]. Diffuse scattering occurs when the wavelength is much smaller than the grains, causing the acoustic wave to collide with the grain boundaries and reflect in many different directions [9]. A general rule of thumb states that the wavelength λ should be grater than 6Φ in order to avoid excessive attenuation [9].

There are different ways in which to express attenuation [9, 10]. The attenuation can be expressed as a function of the frequency f, an absorption constant C_A and a scattering constant C_S as follows [9]:

$$Attenuation = C_A f + C_S f^4 \tag{3.6}$$

Looking at equation 3.6, it can be seen that the attenuation will always increase for increasing frequency. In practice however, the attenuation of an ultrasonic signal can be measured by looking at the first and second back wall reflections of the ultrasonic signal. Measuring the amplitude in the first back wall A_1 and the amplitude of the second back wall A_2, the attenuation can be expressed as [2]:

$$Attenuation = 20 \cdot log_{10}\left(\frac{A_1}{A_2}\right) \tag{3.7}$$

3.6. Reflection and Transmission Coefficients

One important aspect of ultrasonic waves is the reflection and transmission coefficients [12]. The reflection and transmission coefficients essentially express how much of the ultrasonic wave's energy (amplitude) will be reflected and transmitted at an interface due to the inherent mismatches in acoustic impedance of materials. The reflection and transmission coefficients are both functions of the acoustic impedance of the material, which can be defined as:

3

$$Z_n = \rho_n c_n \tag{3.8}$$

Where ρ is the density of the material, c is the velocity of sound in that material and n denotes the material. Using equation 3.8, the reflection coefficient R can be expressed as:

$$R = \frac{Z_2 - Z_1}{Z_1 + Z_2} \tag{3.9}$$

Where Z_1 is the acoustic impedance of the first material whilst Z_2 is the acoustic impedance of the second material. The transmission coefficient T can then be expressed as:

$$T = \frac{2Z_2}{Z_1 + Z_2} \tag{3.10}$$

It is important to remember that ultrasonic transducers require couplants to transmit the signal. The couplant will also have an effect on the transmission and it can be expressed as [9]:

$$T_{couplant} = \frac{(4Z_1/Z_3)}{[(Z_1/Z_3+1)^2 cos^2\theta + (Z_1/Z_2 + Z_2/Z_3) sin^2\theta]} \tag{3.11}$$

Where $\theta = 2\pi t_{couplant}/\lambda_{couplant}$, $T_{couplant}$, Z_1 is the acoustic impedance of the wedge of the probe, Z_2 is the acoustic impedance of the test piece and lastly Z_3 is the acoustic impedance of the couplant.

Having a transmission coefficient $T > 1$ is possible because the time rate of flow of energy (power) is determined by both the amplitude and velocity of the wave, and the power should be in balance at the interface (i.e. the amplitude increases but the velocity decreases). [12]

3.7. Views in Ultrasonic Testing

The data collected by ultrasonic testing can be displayed in a variety of different views intended to facilitate the interpretation of the results. These will be explained in the following sections.

3

3.7.1. A-SCAN

An A-scan is the 'raw' data collected by the ultrasonic instrument and plots the amplitude of the acoustic signal received on the y-axis and time on the x-axis of a localized point. During inspection, the UT instrument can represent distance in the x-axis instead of time by either calibrating the UT instrument or by inputting the velocity of acoustic waves in the material being inspected. A typical representation of an A-scan of an isotropic material (epoxy) can be seen in figure 3.7.

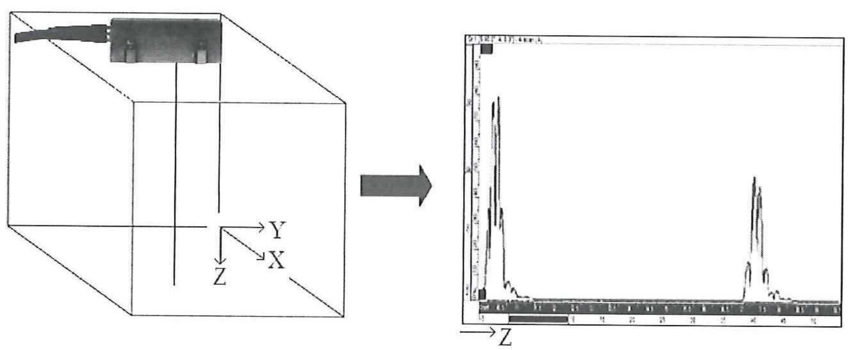

Figure 3.7: Example of a typical A-scan of Epoxy

A-scans show the reflections of the acoustic waves in the material, and hence can give information on the presence of defects and on the depth of such defects as well as information on the thickness of the material. When performing an A-scan, a gate is typically placed between the interphase echo (first peak) and the first back-wall echo (second peak), as shown by the red line in figure 3.7, to act as an alarm to detect defects and as a reference point to create C-scans.

During inspections of GLARE, the conventional A-scan is very difficult to interpret since there are various reflections caused by the anisotropy of the material, making the distinction between defects and echos occurring when the signal travels from one layer to the other difficult. A typical scan of an isotropic material (epoxy) and GLARE can be compared in figure 3.8.

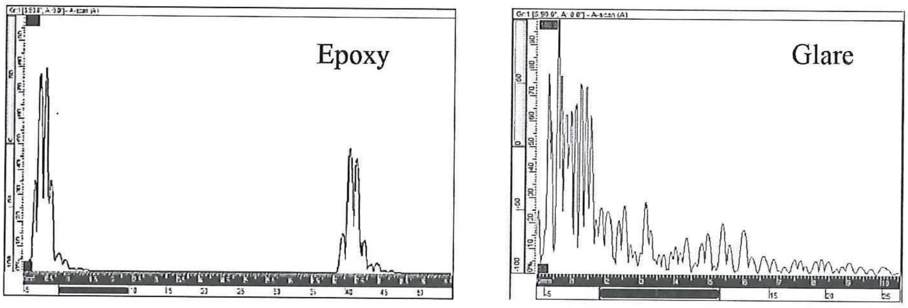

Figure 3.8: Comparison of an epoxy (left) and a GLARE (right) A-scan

3.7.2. B-SCAN
B-scans are in essence a combination of stacked A-scans through the length of a specimen, creating a cross section of the specimen as shown in figure 3.9. The amplitude of the signal is represented in B-scans as a color, where the color palette uses the highest amplitude of the A-scans as a reference point. The y-axis represents either time or depth (distance) whilst the x-axis represents distance length wise.

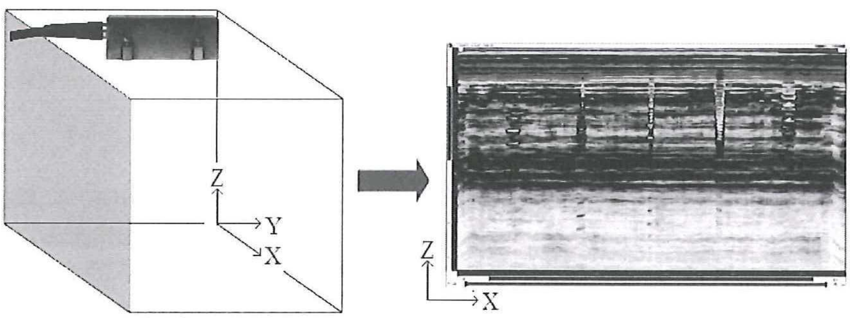

Figure 3.9: Example of a typical B-scan of GLARE

In contrast to A-scans, a 1D encoder is required to make a B-scan due to the need to stack the A-scans together. B-scans can show the same information as an A-scan regarding the presence of defects and depth/thickness information but can offer more information of the location and the size of the defect due to the use of an encoder. Due to the use of a color palette using the highest amplitude as a reference point, B-scans are very useful presentations of information when inspecting GLARE. Due to the data being presented relative to the highest amplitude, it becomes easy to find deviations.

3.7.3. C-SCAN
C-scans offer a top view representation of the specimen being inspected, as shown in figure 3.10. The x- and y-axis in a C-scan represent distance, whilst the amplitude is represented by the color palette. In contrast to B-scans where the amplitude is shown as relative to the maximum amplitude, the amplitude representation in a C-scan is in reference to the gate set in the A-scan. Therefore, C-scans are *greatly* dependent on the gate set in the A-scan. This also gives great flexibility and allows for C-scans to be made that represent different information such as changes in thickness or defects.

C-scans require the use of a 2D encoder in order to track the position of the transducer and create the full C-scan, allowing the location, shape and size in the x- and y-axis of the defect to be found. C-scans however do not provide information on the depth of the defect.

3.7.4. S-SCAN
An S-scan is a special type of view unique to Phased Array Ultrasonic (PAUT) inspections which makes use of the wave steering ability of PAUT transducers. This view is a stacking

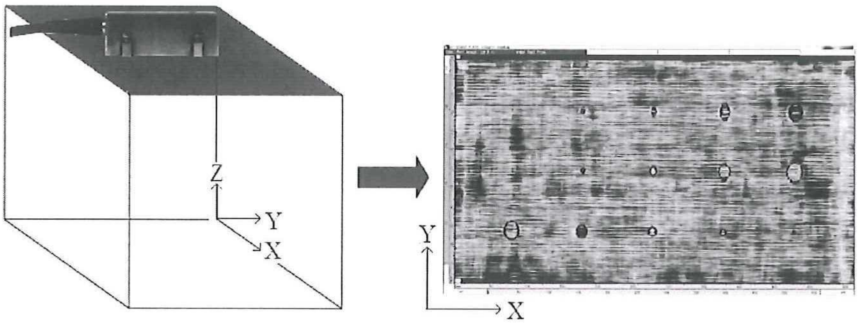

Figure 3.10: Example of a typical C-scan of GLARE

of A-scans performed over a range of angles, as can be seen in figure 3.11. It is therefore very similar to a B-scan, but performed at various angles. The advantage of such type of view is that it can provide a wide view without the need to move the transducers as well as penetrate below corners where inspection is normally difficult to conduct. S-scans will not be used in this thesis since the inspections performed will be 0° inspections.

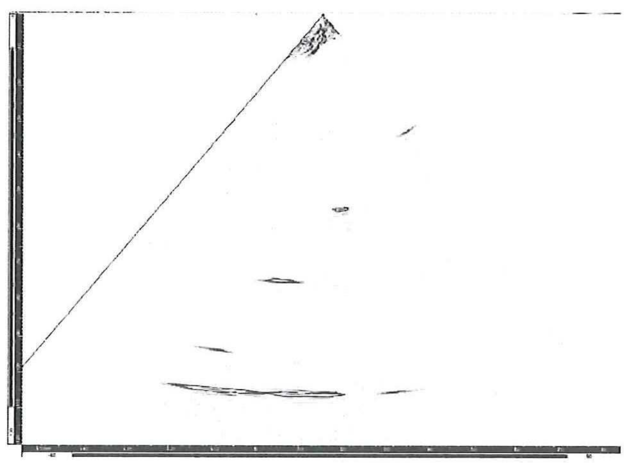

Figure 3.11: Example of a typical S-scan [9]

3.8. PAUT

The main difference between Phased Array Ultrasonics (PAUT) and conventional ultrasonics (UT) is the use of an array of independent piezoelectric crystals in PAUT instead of the individual piezoelectric monocrystal utilized in conventional UT. Utilizing an array of individual piezoelectric crystals allows for several advantages over the monocrystal approach, including greater flexibility in the ultrasonic beam steering and focusing. These elements can be configured in a linear, 2D or even radial array, as shown in figure 3.12.

The main characterizing factors in a PAUT transducer are the frequency f and the geo-

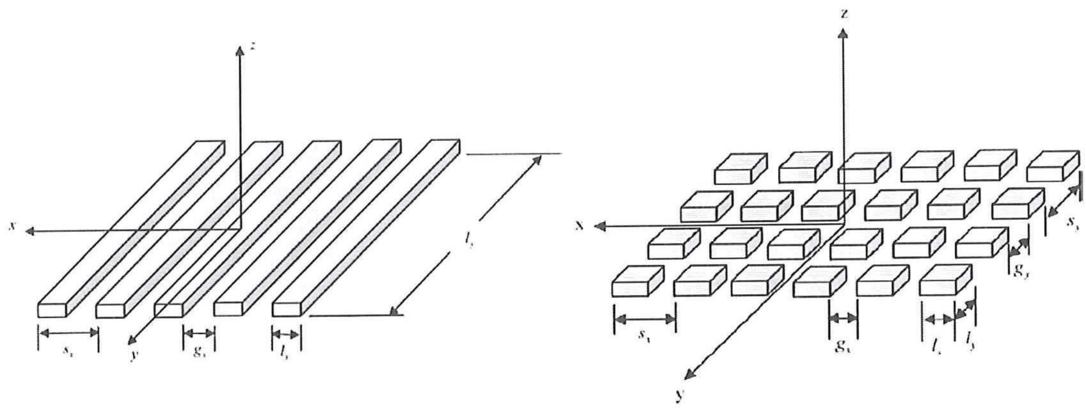

Figure 3.12: Linear 1D array configuration (left) and 2D array configuration (right) [1]

metrical parameters shown in figure 3.12, such as the number of elements, the element pitch s_x, the element gap g_x, the element width l_x and the element length l_y (also referred to as elevation) [1]. Two other very important parameters that derive from those previously mentioned are the aperture A, defined as the distance from the first element to the last element and the active aperture A_a, defined as the distance from the first active element to the last active element used in a specific law [1]. Hence if a 64 element PAUT transducer is used but only 16 elements are active, then the aperture is measured as the distance from element 1 to 64, whilst the active aperture is the distance measured from element 1 to 16. The effects of these will be discussed in the following sections.

3.8.1. Beam Profile

An ultrasonic beam profile is usually divided into 3 different 'zones': The dead zone, the near field and the far field, all of which are shown in figure 3.13. The dead zone is a part of the beam closest to the transducers surface where no information can be collected due to the fact that the piezoelectric elements are still vibrating from the pulse. This part is usually very small and depends on the damping properties of the transducer. The near field, also referred to as the Fresnel zone, is a part of the ultrasonic beam where there are considerable amounts of constructive and destructive wave interaction. The energy build up by these waves becomes the highest at the end of the near field, referred to as the focus point, where the constructive effects of wave interaction create the highest sound pressure in the ultrasonic beam. Since the acoustic pressure (energy) is the highest at the focus point, it is where the best sensitivity and resolution can attained. Lastly, the far field, also referred to as the Fraunhofer zone, is the area after the near field where the acoustic waves behave as one combined wave front. At the far field, the sound pressure starts to decrease as the beam's profile slowly diverges. [10]

The beam profile of a conventional UT transducer is decided before manufacturing and is based on the application it has to fulfill since it is fixed and can only be slightly modified by the use of wedges. On the other hand, Phased Array Ultrasonic (PAUT) transducers have the ability to modify the beam profile by electrically pulsing each individual element at different times. As shown in figure 3.14, PAUT transducers can change the

3

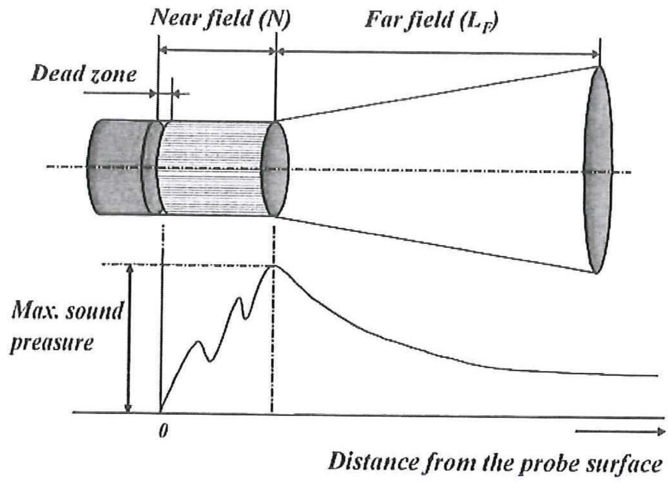

Figure 3.13: Ultrasonic beam profile [10]

beam's focus point as well as the beam's angle by applying different pulses.

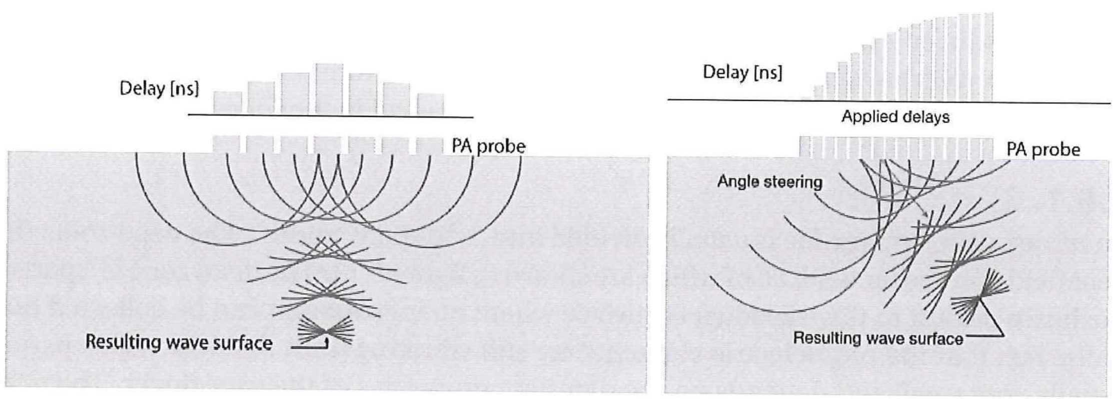

Figure 3.14: PAUT focusing (left) and steering (right) capabilities [8]

BEAM FOCUSING

Beam focusing is made possible in PAUT transducers because each piezoelectric crystal element in a PAUT transducer is independent so they can be triggered independently at different times and will create independent acoustic waves. As the waves travel away from the source, the wave fronts of each element will interact, creating constructive and destructive interference. By controlling the times at which each individual element is triggered, these effects can be controlled, creating the highest constructive interference in the desired direction and at the desired depth, as depicted in figure 3.14.

Even though PAUT transducers have the ability to focus the ultrasonic beam, they still posses a near field length that limits the focal distance. PAUT transducer can only focus at distance closer than the near field length N_0 of the transducer, which can be approximated as [13]:

$$N_0 = \frac{A_{act}^2}{4\lambda} \tag{3.12}$$

Where λ is the wavelength of the acoustic waves in the material inspected and A_{act} is the active aperture of the transducer, defined as [14]:

$$A_{act} = s_x(N_{act} - 1) + l_x \tag{3.13}$$

Where N_{act} is the number of active elements. It can be seen from equation 3.12 that the near field length of a PAUT increases when the active aperture increases. However, it can also be seen that the element width l_x has very little influence in the near field length. It has been shown that element width l_x will increase the pressure in the far-field with increasing element width [14]. Therefore the biggest effect on the near field length relies on the number of elements used and in the transducer pitch.

The near field length in the constituent materials of GLARE, as defined by equation 3.12 for the transducers used for testing during this thesis, can be seen in table 3.1. It is worth noting that the PAUT instrument used for testing during this thesis was limited to firing 16 elements at once, hence limiting the active aperture of the transducers to only 16 elements. It is also worth mentioning that these Near Field Lengths are larger than the thicknesses of the plates that will be tested during this thesis.

Table 3.1: Near field length of the transducers in aluminum and epoxy

Transducer	**2.25L32**	**5L64**	**10L32**
Aperture [mm]	64	64	9.9
Active Aperture [mm]	32	16	4.95
N_0 Aluminum [mm]	98.8	50.6	9.7
N_0 Epoxy [mm]	271.6	139.1	26.6

When a PAUT beam is focused beyond its near field length, the PAUT will simply be unfocused, leading to a beam profile similar to the one presented on the left side of figure 3.15. However, when the beam is focused at a focus point closer than the near field length, the PAUT beam will converge until it reaches the focus point and then diverge in the far field, as shown on the right side of figure 3.15. [9]

The number of elements used when focusing the PAUT beam will have a great effect in the beam profile and the focusing of the beam. Using a greater number of elements improves the focusing of the beam since a larger number of elements allows for more flexible time delays and more precise control of the beam, leading to a slimmer beam profile as well as a higher acoustic pressure in the focus area. Increasing the width will give a higher acoustic pressure as well as a better signal-to-noise ratio but will not affect the beam profile [14].

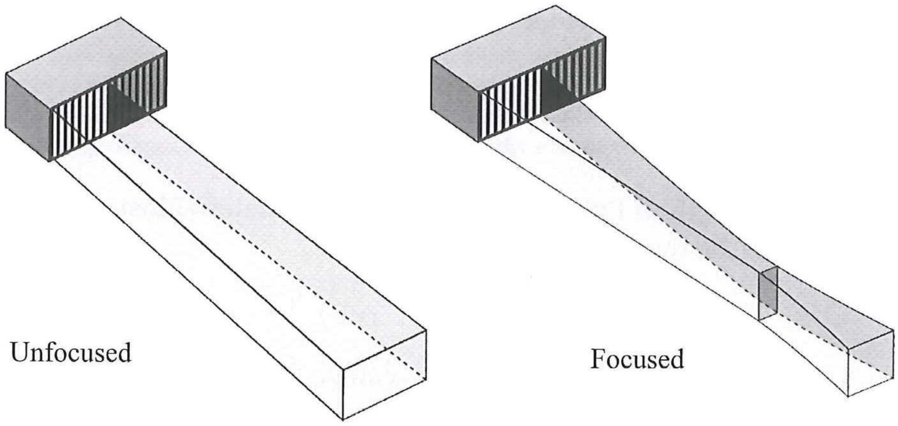

Figure 3.15: Beam profile of an unfocused (left) and a focused (right) linear PAUT transducer [9]

BEAM STEERING

When forming of a beam, the maximum angle at which the beam can be steered is mainly determined by the wavelength of the acoustic wave in the material λ, the element pitch s_x and the number of active elements N_{act}. The steering angle $(\theta_s)_{max}$ can be expressed as: [15]

$$(\theta_s)_{max} = sin^{-1}\left(\frac{\lambda(N_{act}-1)}{s_x N_{act}} - 1\right) \tag{3.14}$$

From equation 3.14 it becomes clear that the smaller the element pitch s_x, the larger the steering can be. Small element pitch however reduces the near field length of the transducer and can cause excessive grating lobes, as will be discussed in the next section. [15]

SIDE LOBES AND GRATING LOBES

Even though PAUT transducers can control the beam profile, some undesired effects such as side lobes and grating lobes occur.

Side Lobes

Side lobes are pressure distributions that stem at different angles from the main acoustic pressure beam and are a consequence of pressure leaking from the transducer elements at different angles from the main acoustic pressure beam, as shown in figure 3.16.

The ratio of the peak side lobe to the main acoustic lobe ξ can be calculated as a function of the number of active elements N_{act} as [14]:

$$\xi = \frac{2}{3\pi}\left|\frac{3\pi/2N_{act}}{sin(3\pi/2N_{act}))}\right| \tag{3.15}$$

The side lobe's amplitude is only dependent on the number of elements used, where increasing the number of elements decreases the effect of side lobes. It is worthy noticing that as $N_{act} \to \infty$, $\xi \to 2/3\pi$, which equates to $-13.5dB$ difference between the main

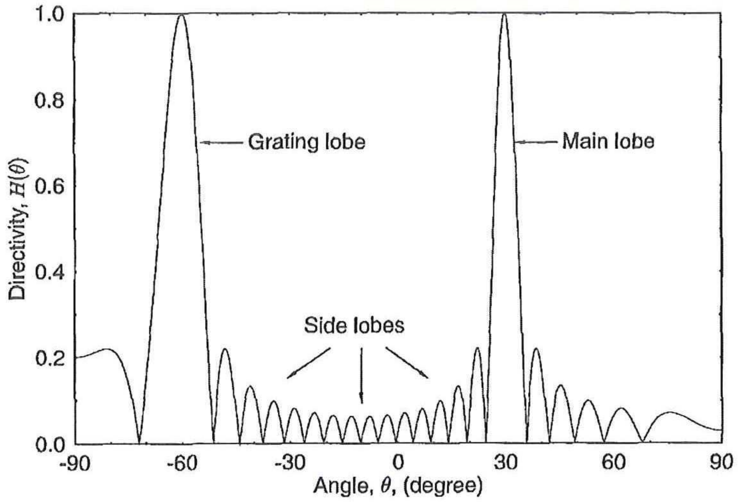

Figure 3.16: Main lobe (beam), side lobes and grating lobes occurring in a 30° steered beam [15]

lobe and the main side lobe. This theoretical limit for the suppression of side lobes is achieved with 16 elements, above which no noticeable suppression of side lobes occurs. [14, 15]

It can therefore be concluded that to avoid the effect of side lobes 16 elements should be used when forming the beam. This is attainable since the PAUT instrument used for testing during the thesis can actually excite up to 16 elements.

Grating Lobes

Whilst side lobes occur in both conventional UT and PAUT transducers, grating lobes only occur in PAUT transducers and are caused by the even constant spacing between the transducer elements. The angle of these grating lobes β_g can be calculated as: [15]

$$\beta_g = sin^{-1}\left(sin\theta_s - \frac{m\lambda}{s_x N_{act}}\right) \quad where\ m = \pm 1, \pm 2 \pm 3... \tag{3.16}$$

Increasing the element width tends to reduce the grating lobe amplitude [14]. Ideally, to avoid grating lobes, the pitch $s_x \leq \lambda/2$ [15].

The amplitude of these grating lobes mainly depend on transducer properties such as frequency f, bandwidth BW, pitch size s_x and number and size of elements [8]. When the PAUT transducer's pitch size is large, the effect of both side lobes and grating lobes will become bigger. Therefore reducing the size of the elements as well as the pitch will reduce the effect of side lobes and grating lobes in the PAUT beam. Furthermore, reducing the frequency and increasing the bandwidth can reduce the amplitude of the side lobes and grating lobes, as shown in figure 3.16.

3.8.2. DELAY LAWS

The set of times at which each individual element is triggered are called delay laws [1]. These delay laws can be calculated for both linear and 2D arrays. However, the research in this thesis was conducted with only linear array PAUT transducers, and therefore only this type will be further explored.

Looking at figure 3.17, the focal laws required to focus a specific PAUT transducer at a depth/distance F and at a steering angle Φ can be determine based on the PAUT transducer properties. A variable $\bar{M}$ can be defined for convenience and ease of calculation as:

$$\bar{M} = \frac{M-1}{2} \tag{3.17}$$

Which then allows for the distance to the centroid of the m^{th} element e_m to be defined as:

$$e_m = [(m-1) - \bar{M}]s \tag{3.18}$$

Where M is the number of active elements in the transducer and s is the distance from the edge of one element to the edge of the next, as defined in figure 3.12.

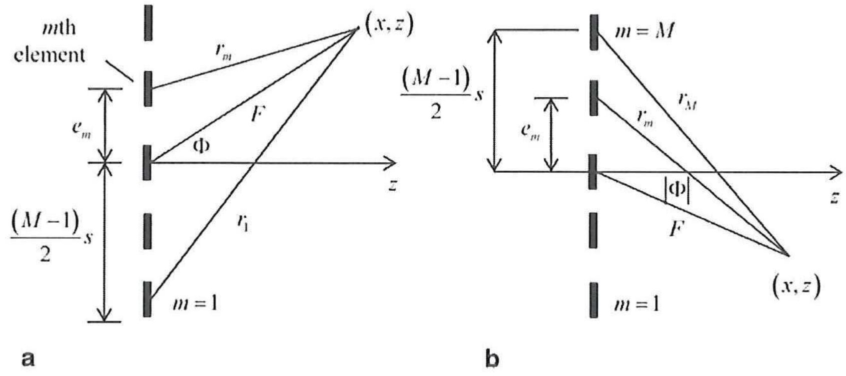

Figure 3.17: PAUT focusing and steering when $\Phi > 0$ (left) and $Phi < 0$ (right) [1]

The delay laws can then be expressed as:

$$\Delta t_d = r_1/c - r_m/c \tag{3.19}$$

Looking at figure 3.17, r_1 and r_m can be defined as:

$$r_1 = \sqrt{F^2 + (\bar{M}s)^2 + 2F\bar{M}s\,sin\Phi} \tag{3.20}$$

$$r_m = \sqrt{F^2 + (e_m)^2 - 2Fe_m sin\Phi} \tag{3.21}$$

Lastly, combining equations 3.19, 3.20 and 3.21, the delay law can be expressed as:

$$\Delta t_d = \frac{1}{c}\left[\sqrt{F^2 + \left(\bar{M}s\right)^2 + 2F\bar{M}ssin\Phi} - \sqrt{F^2 + (e_m)^2 - 2Fe_m sin\Phi}\right] \tag{3.22}$$

For the case where $\Phi > 0$, and as:

$$\Delta t_d = \frac{1}{c}\left[\sqrt{F^2 + \left(\bar{M}s\right)^2 + 2F\bar{M}ssin|\Phi|} - \sqrt{F^2 + (e_m)^2 + 2Fe_m sin|\Phi|}\right] \tag{3.23}$$

For the case where $\Phi < 0$.

3

3.9. THEORETICAL DEFECT DETECTION

As a general rule of thumb, the theoretical minimum defect size D_{min} that can be detected in a material can be expressed as [6]:

$$D_{min} > \frac{\lambda}{2} \tag{3.24}$$

It is however important to notice that UT and PAUT transducers do not operate at a single frequency but within a specific bandwidth with a center frequency. Therefore, the size of the defects that can be detected can possibly be smaller since frequencies higher and lower than the center frequency will also occur. Nevertheless, the minimum defect size that can be found in both the aluminum and epoxy layers in GLARE can be seen in figure 3.18.

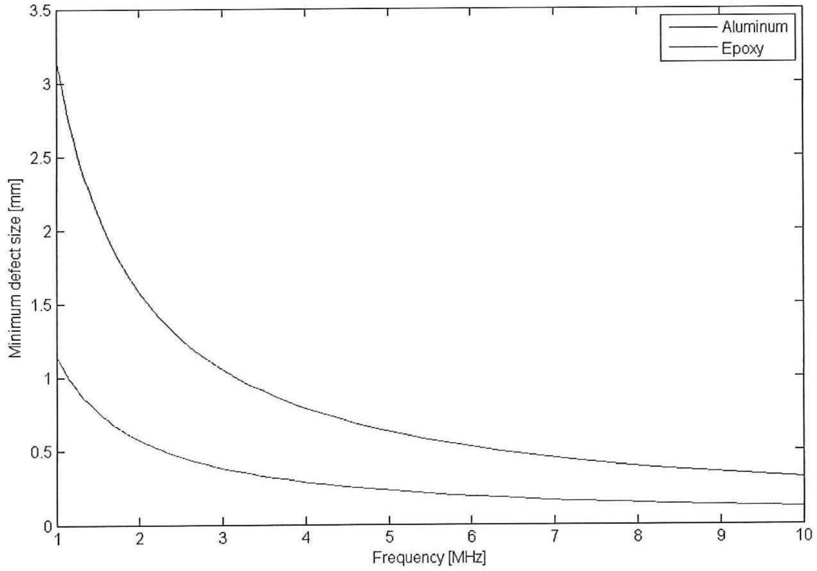

Figure 3.18: Theoretical minimum defect size detectable in aluminum and epoxy

From figure 3.18, it can be clearly seen that there is a relatively big difference in the size of the defects that can be detected in epoxy and aluminum. Due to the lower acoustic velocity in epoxy, the defects that can be found are roughly twice as small. It is also important to notice that as the frequency increases, the size of the defects that can be found changes very slightly. It is therefore important to chose the frequency wisely as an increase in frequency might give little benefit to the minimum size of defects that can be found whilst excessively increasing the attenuation.

As mentioned in section 3.5, the size of the grains can cause great attenuation of the ultrasonic signal, hindering the inspection. It is therefore interesting to determine what grain size will cause excessive attenuation when performing PAUT inspections of GLARE. Utilizing the rule of thumb mentioned in section 3.5 between the wavelength and the grain size, $\lambda > 6\Phi$, the grain size above which excessive attenuation will occur can be plotted for both the aluminum layers and the epoxy layers of GLARE, as shown in figure 3.19.

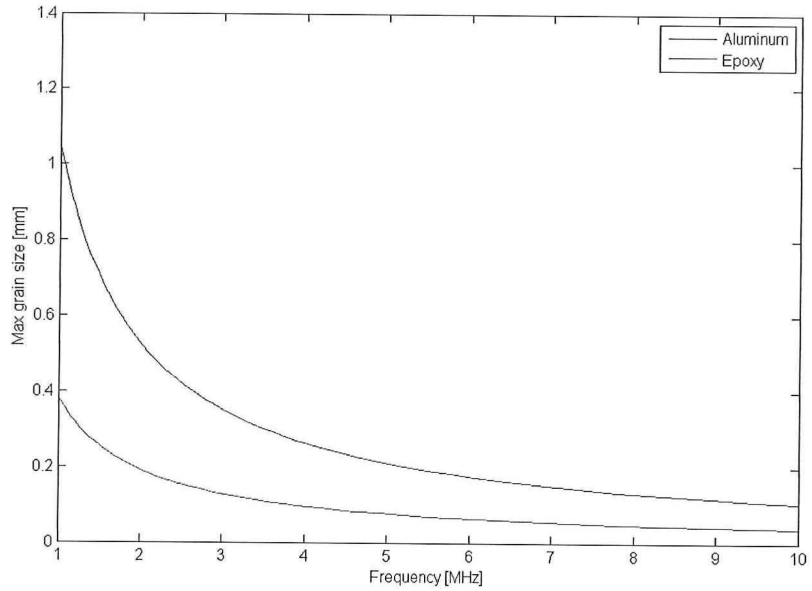

Figure 3.19: Theoretical maximum grain size in aluminum and epoxy

As can be seen in figure 3.19, the highest frequencies are the most susceptible to small grain size in the material. The smallest grain size that will cause excessive attenuation is $38\mu m$ and occurs in the epoxy layers with 10MHz frequencies. Considering that the fibers embedded in the epoxy prepreg are $10\mu m$, it should become clear that no excessive attenuation should be encountered due to the grain size of the materials.

REFERENCES

[1] L. W. Schmerr Jr., *Fundamentals of Ultrasonic Phased Arrays* (Springer, 2014).

[2] P. McIntire, R. E. J. Green, and A. S. Birks, eds., *Nondestructive Testing Handbook-Volume Seven: Ultrasonic Testing*, 2nd ed. (American Socirty for Nondestructive Testing, 1991).

[3] R. A. M. Coenen, *Design of a Quality Assurance System for Structural Laminates,* Ph.D. thesis, Delft University of Technology (1998).

[4] *Phased Array Testing: Basic Theory for Industrial Applications,* 1st ed. (Olympus NDT, 2010).

[5] F. Dijkstra, *Ultrasonic Testing of Austenitic Welds* (Applus RTD, 2012).

[6] W. Martens, *Phased Array Sabca Training,* Tech. Rep. (TiaT Europe B.V., Roosendaal, 2014).

[7] ASTM, *E1065-08 Standard Guide for Evaluating Characteristics of Ultrasonic Search Units,* Tech. Rep. (ASTM International, West Conshohocken, 2008).

[8] *Advances in Phased Array Ultrasonic Technology Applications* (Olympus NDT, 2007).

[9] *Introduction to Phased Array Ultrasonic Technology Applications,* 3rd ed. (Olympus NDT, 2007) p. 354.

[10] W. Martens, *Ultrasonic Level II,* Tech. Rep. (TiaT Europe B.V., Roosendaal, 2009).

[11] E. P. Papadakis, *Rayleigh and Stochastic Scattering of Ultrasonic Waves in Steel,* Journal of Applied Physics 34, 265 (1963).

[12] P. B. Nagy, *Part 3: Reflection and Transmission of Ultrasonic Waves,* Tech. Rep. (University of Cincinnati, Cincinnati).

[13] L. Azar, Y. Shi, and S. Wooh, *Beam focusing behavior of linear phased arrays,* NDT&E International **33**, 189 (2000).

[14] S. Wooh and Y. Shi, *Influence of phased array element size on beam steering behavior,* Ultrasonics **36**, 737 (1998).

[15] S. Wooh and Y. Shi, *Optimum beam steering of linear phased arrays,* Wave Motion **29**, 245 (1999).

4
Experimental Setup

The most basic phased array ultrasound system consists of a PAUT instrument and a PAUT transducer. The PAUT instrument is a piece of equipment which excites the PAUT transducer and receives the information from the PAUT transducer. These systems will control the voltage, focal laws, frequencies and other important parameters as well as process and analyze data. The system setup of the NDT laboratory of the Aerospace Faculty at TU Delft used for testing in this thesis can be seen in figure 4.1.

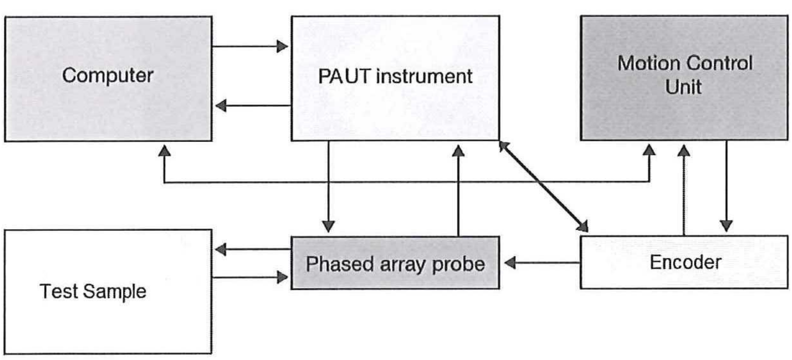

Figure 4.1: PAUT system setup of the NDT laboratory of the Aerospace Faculty at TU Delft

As seen in figure 4.1, the PAUT instrument (Olympus OmniScan SX) interacts with the PAUT transducer by exciting the elements of the transducer with different delay times. The transducer will then create an ultrasonic signal that will penetrate the test sample and reflect back to the PAUT transducer. The transducer will receive the signal and send it to the PAUT instrument, which can then reconstruct the data and display it in different modes (A-scan, B-scan, etc). This information can be further processed and analyzed by a computer with the Olympus TomoView software.

For automated inspection, the computer can be used to control a Motion Control Unit which will control the transducers positioning. The encoder will then transmit the position coordinates to the PAUT instrument so that the PAUT instrument can create B- and

C- scans of the sample.

4.1. PAUT INSTRUMENT

The PAUT instrument used for testing was an Olympus OmniScan SX commercial unit running the OmniScan MXU 4.1R8 software. This instrument is a portable PAUT instrument meant for remote PAUT inspections capable of both data collection as well as simple analysis and reporting. It is therefore not capable of connecting to a computer directly and all data has to be exported via an SD card or a USB storage device. The Olympus OmniScan SX can pulse PAUT transducers with an adjustable negative square pulse of 40V, 80V or 115V. The maximum active aperture that can be used is of 16 elements, allowing 16 elements out of the total amount of elements in the transducer to be used simultaneously. The OmniScan SX is limited to one group of focal laws at a time, and therefore does not allow the performance of tests with varying focal laws.

Figure 4.2: Olympus OmniScan SX PAUT instrument [1]

The Olympus OmniScan SX also has an adjustable gain for the input signal ranging from 0 dB to 80 dB, allowing the user to increase or decrease the amplitude of the received signal if the signal is too high or too low. It has a digitizing frequency of 400MHz (12 bits), allowing for a measurement to be taken every 2.5ns. The OmniScan SX also allows for the signal received to be averaged in real time up to 16 times. It also has the ability to use 3 low-pass, 3 band-pass and 5 high-pass filters as well as a frequency dependent smoothing filter for better visualization.

External encoders can be connected to the Olympus OmniScan SX via a LEMO 16-pin female circular input, allowing for 2-axis quadrature or clock/direction signals to be read by the OmniScan SX. This allows for C-scans to be performed by means of a raster scan with a file size of up to 300MB.

4.2. PAUT TRANSDUCERS

Three different transducers with center frequencies of 2.25MHz, 5MHz and 10MHz were used for testing in this thesis. These transducers were selected to provide a 'wide' range of frequencies and from those commercially available. The properties of the individual transducers can be seen in table 4.1.

Table 4.1: Transducer properties

Transducer	2.25L32	5L64	10L32
Serial Number	N2350	K1997	N1728
Average Center Frequency [MHz]	2.44	5.00	9.97
Average -6dB Bandwidth [%]	71	79	62
Number of Elements	32	64	32
Aperture [mm]	64.00	64.00	9.90
Elevation [mm]	7.00	7.00	7.00
Pitch [mm]	2.00	1.00	0.31
Type	NW	NW	Angled
Index resolution [mm]	2	1	0.3

As can be noted from table 4.1, all the transducers had relatively large bandwidths higher than 60%, which is a common trait of PAUT transducers. It can also be observed that all of the transducers had more than 16 elements, meaning that the effects of the side lobes due to the amount of elements used can be suppressed. However, none of the transducers can ideally remove the grating lobes since, as mentioned in chapter 3.8, a pitch $s_x \leq \lambda/2$ is required, which does not occur on most cases. This is shown in table 4.2, where one can observe that the only transducer that can avoid grating lobes is the $10MHz$ transducer when inspecting aluminum.

On average it can be observed that the $10MHz$ transducer will most likely be the least affected by grating lobes whilst the $5MHz$ will be the transducer affected the most by grating lobes.

The transducers used for testing were *not* contact transducers and therefore required wedges, such as the one shown in figure 4.3, for the inspection of the relatively thin GLARE panels. These wedges were also manufactured by Olympus and were made out of Rexolite, a transparent thermoset polymer. All the transducers had a matching medium (material between the piezoelectric elements and the surface of the transducer) matched to the acoustic impedance of Rexolite. This ensures a better transmission of the acoustic wave from the transducer to the wedge.

Table 4.2: Add caption

Transducer	2.25L32	5L64	10L32
c_{al} [m/s]	6320	6320	6320
c_{ep} [m/s]	2300	2300	2300
λ_{al} [mm]	2.809	1.264	0.632
λ_{ep} [mm]	1.022	0.460	0.230
s_x [mm]	2.000	1.000	0.310
$\lambda_{al}/2$ [mm]	1.404	0.632	0.316
$\lambda_{ep}/2$ [mm]	0.511	0.230	0.115
$\frac{\lambda_{al}}{2s_x}$	0.702	0.632	1.019
$\frac{\lambda_{ep}}{2s_x}$	0.256	0.230	0.371
Average	0.479	0.431	0.695

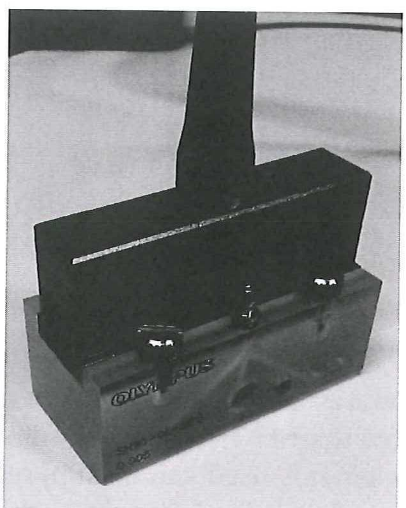

Figure 4.3: 2.25MHz PAUT transducer mounted on a Rexolite wedge

For the 2.25MHz and the 5MHz transducers, the wedges were manufactured with water channels that could be connected to a water pump in order to provide coupling when performing the inspection. On the other hand, the 10MHz transducer was mounted on a wedge that did not have any water channels but was instead mounted on a bracket which was equipped with water channels to provide coupling for the inspection.

4.3. AUTOMATED XY STAGE ENCODER

The motion control unit and the encoders responsible for the automated inspection of panels were both mounted on a custom rig capable of performing 2D inspections of flat surfaces. This automated unit utilized two LIDA 17C quad encoders to track the position of the transducer mounted on the rig while two independent electrical motors were responsible for the movement of the transducer. The automated XY stage was a feedback control system (or a closed loop system) controlled by a computer, where the encoder information was fed back to the computer to control the independent electrical motors in order to be able to accurately control speed and positioning. The encoder signal was split before it was fed back to the computer, allowing for the signal to be sent to the Olympus OmniScan SX and the computer simultaneously. In such a manner the signal was not interrupted and allowed for the proper functioning of the XY stage's feedback control system as well as the proper transmission of the encoder data to the PAUT instrument. The encoder resolution on the OmniScan SX was of 1000 steps/mm. The software used to control the automated XY stage was PEWIN32 by Delta Tau Data Systems Inc.

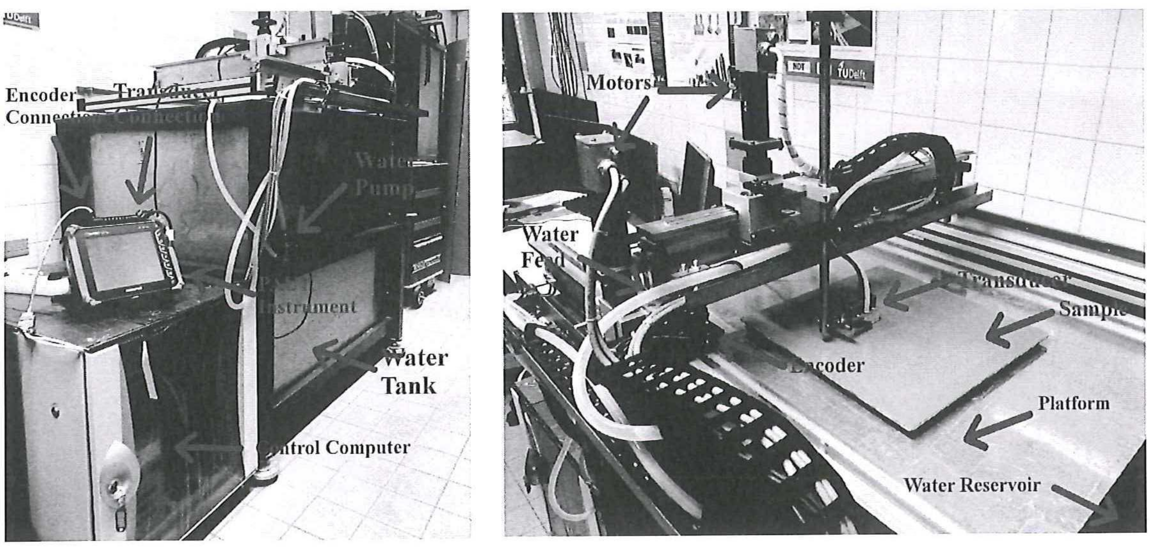

Figure 4.4: Automated XY stage setup

As can be seen in figure 4.4, the whole system is mounted on a water tank, which can be used as a source of water to provide coupling to the transducers and as a water reservoir where water is collected during inspection. During testing, the water was pumped to the transducer with a small water pump, which collected the water from the tank and pumped it to the transducer. The test panels were placed on top of an aluminum platform which was suspended above the water. The water tank also allowed for the possibility of performing submerged tests.

4.4. OLYMPUS TOMOVIEW ANALYSIS TOOL

Tomoview Analysis is a software tool from Olympus aimed at performing detailed analysis of UT and PAUT data. Tomoview offers various analysis tools to manipulate the data collected for better analysis. Tomoview provides the ability to create software C-scans, where a C-scan can be created based on a gate that is applied after the inspection. Other tools include the merging of different C-scans to provide various information in one file or signal-to-noise analysis tools aimed at objectively detecting defects in accordance to specified signal-to-noise ratios.

Tomoview software will be the primary software used for the analysis of the data collected during the thesis. Further explanations of the tools will be given when pertinent during the analysis.

REFERENCES

[1] *Introduction to Phased Array Ultrasonic Technology Applications*, 3rd ed. (Olympus NDT, 2007) p. 354.

4

5

Experimental Analysis

5.1. Test Samples

A total of three different flat GLARE test panels were used for the the testing of GLARE with PAUT. The objective of these test samples was to simulate delamination defects and damages at different depths and in different types of GLARE. In this section the selection of damage to be recreated as well as the method chosen to do so will be explained and justified. Furthermore, the final GLARE samples used for testing will be described.

5.1.1. Damage Type Selection

Delaminations were chosen as the defect/damage to recreate due to the fact that they are dangerous types of damages that can occur during the operational lifetime of an aircraft and are not easily detectable by visual inspection. As explained in chapter 2.2, delaminations have a great impact in the mechanical performance of the part and it was therefore deemed important to be able to detect them during the operation life of an aircraft.

5.1.2. Damage Type Recreation

When a delamination occurs, the space between the two separated laminates is filled by air, liquids or a vacuum [1]. As explained in chapter 3, the reflections that indicate irregularities in the material are caused by the change in acoustic impedance of the material, which in turn is caused by an irregularity in the material. It is therefore important for ultrasonic inspections to recreate the interface between the test material and the location where the damage occurs in order to evaluate the interaction between the ultrasonic wave and the damage/defect.

In the case of a delamination in GLARE, it was considered that it would most likely contain entrapped air instead of liquids or a vacuum. In the hypothetical case a vacuum would occur, the two delaminated layers would be pulled together by the vacuum, hence causing a type of 'kissing bond' situation, making inspection very difficult. Furthermore, due to the main use of GLARE as a structural skin in an aircraft, liquids within the delaminations are not as likely to occur as air. Water could be a possible fluid to perhaps ingress into the delamination but it would most likely evaporate, leaving an air void. Keeping such observations in mind, it became evident that recreating a delamination with entrapped air was preferable as it will be the most likely case to occur in a real life scenario.

Artificial delaminations are conventionally created in GLARE by inserting foreign material such as Teflon between layers, hindering the adhesion between layers and hence causing a delamination [1]. There were however several drawbacks to applying such a method when performing PAUT investigations in GLARE. One of the main drawbacks would be the fact that when performing the inspection it would be difficult to determine whether the irregularity detected would be caused by the foreign material or the actual delamination. In some cases the foreign material might not create complete delaminations and hence create kissing bonds [1], which could either not show during the inspection or appear as a reflection due to the acoustic mismatch between the inserted material and GLARE instead of the acoustic mismatch between GLARE and the air, liquid or vacuum within the delamination. It was therefore considered necessary, if given the possibility, to recreate delaminations in GLARE in a more suitable manner for PAUT testing.

5

One of the options considered was creating air pockets within GLARE layers that would remain in GLARE during the curing process and hence cause delaminations. This process however, did not offer accurate control over the size, shape or layer in which the delamination occurred, hence not being a viable method to recreate delaminations.

It was finally decided that creating flat bottom holes would be the best viable method to recreate delaminations for ultrasonic pulse-echo inspections in a controlled manner in GLARE. As the name suggests, flat bottom holes are holes with a flat surface artificially created in the material. These types of holes create the same type of interface that would be encountered in a delamination, with the exception of the 'bottom side' of the delamination. The interface exposes a layer of GLARE to air, thus allowing for the same type of change in acoustic impedances as would be expected in a delamination. It is worthy of noticing that these types of defects appear as a change in thickness in a C-scan rather than a defect. This is caused by the fact that a C-scan has water jets on both sides of the sample, and thus the signal will not be completely reflected as it will encounter water instead of air. Therefore it will simply suffer less attenuation in the defect than in the actual material, and hence appear as a change in thickness.

5.1.3. TEST SAMPLE PROPERTIES AND GEOMETRY

Three GLARE panels with different thicknesses and configurations were chosen to be investigated. Three different thicknesses were chosen in order to gain an understanding on the effects of thickness in the detection of delaminations with different frequencies since in an aircraft, the thickness of the parts is not always constant. Furthermore, different types of GLARE with different types of layups are used in aircraft, and hence that also had to be taken into consideration during the investigation. These three panels were scanned by the ultrasonic C-scan at TU Delft in order to ensure that no unintended defects were present.

Due to the availability of GLARE 3 (GL3) and GLARE 4 (GL4) panels having passed quality control tests, these two types of GLARE were chosen as two of the test panels. The last sample to be used for testing was the Master Reference Panel (made of GLARE 3 and referred to as MRP) used to calibrate the C-scan at TU Delft. This sample was chosen due to the fact that creating flat bottom holes in thin GLARE samples was problematic as the quality could not be ensured. Therefore, the MRP was chosen as the third tests panel since it is used as a well known standard for ultrasonic C-scan testing of GLARE panels. A summary of the general properties of the three different test samples are shown in table 5.1.

Table 5.1: Test sample panel properties

Panel	GL3	GL4	MRP
GLARE Type	GLARE 3	GLARE 4B	GLARE 3
Configuration	8/7	6/5	3/2
Layup	0°/90°	90°/0°/90°	0°/90°
Average Panel Thickness [mm]	5.208	4.361	0.875
Average Aluminum Thickness [mm]	0.470	0.423	0.219
Average Epoxy Thickness [mm]	0.207	0.364	0.109

Test sample panels GL3 and GL4 were both prepared with flat bottom holes with diameters ranging from $3mm$ in size to $21mm$ and at different thicknesses. The location, depth and size of the holes is depicted in figure 5.1.

The MRP panel on the other hand was manufactured with $0.07mm$ thick Teflon (PTFE) inserts in order to cause delaminations. The diameter of these Teflon inserts varied from $3mm$ up to $25mm$, as can be seen in figure 5.2. Their positions and sizes are shown in the C-scan presented in figure 5.2. The layer at which the PTFE insets were located is shown by the colored boxes in figure 5.2, where the defects in the red box were located between the first two prepreg layers, the defects in the green box were located within the first aluminum layer and the first prepreg layer, and lastly the defects in the blue box were located in between the first prepreg layer and aluminum.

The nomenclature used to refer to the holes during this thesis is as follows:

$$Hole = \textbf{TestSample}\ D\ \textbf{Diameter}\ R\ \textbf{Row}$$

Where **TestSample** is the test sample in which the hole is, where **Row** is the row in which it is as given in figures 5.1 and 5.2 and **Diameter** is the diameter of the hole. In the case of the MRP, an extra parameter C is added stating the column in which the defect is located.

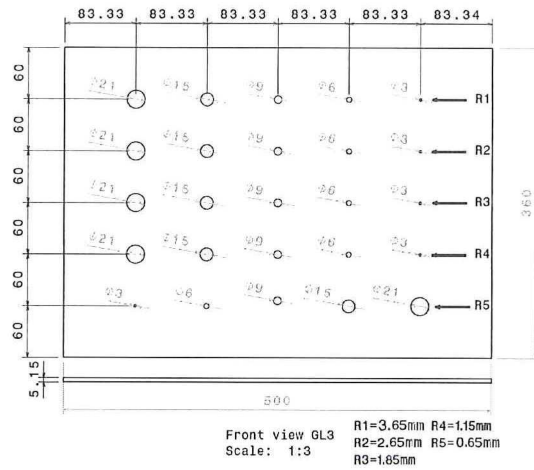

(a) GL3 test sample geometry

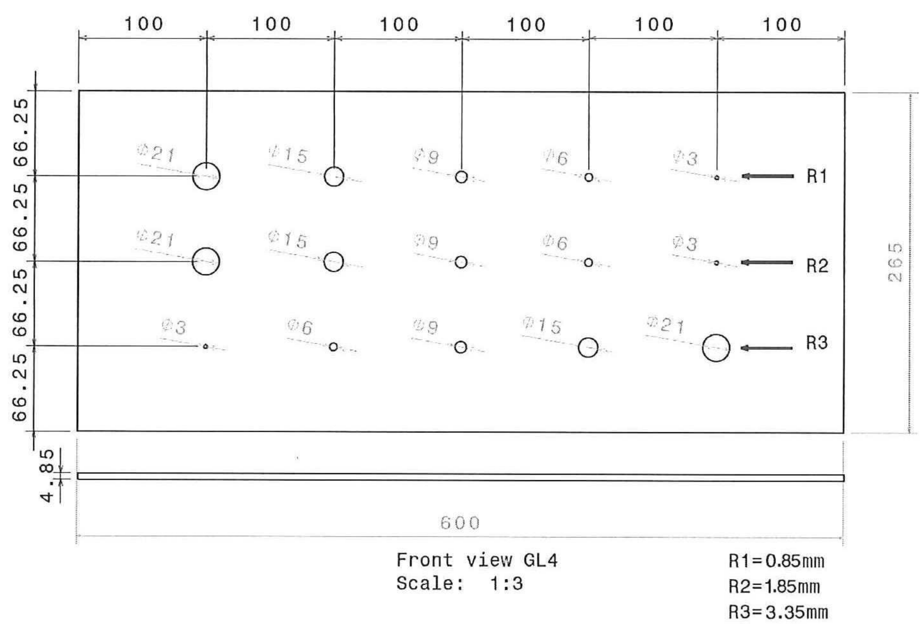

(b) GL4 test sample geometry

Figure 5.1: GL3 and GL4 test sample geometry

When performing the inspections, tacky tape was placed on the bottom of the plate and small wooden pieces were placed in the corners and sides in order to avoid water from penetrating the back of the plate and causing weaker reflections.

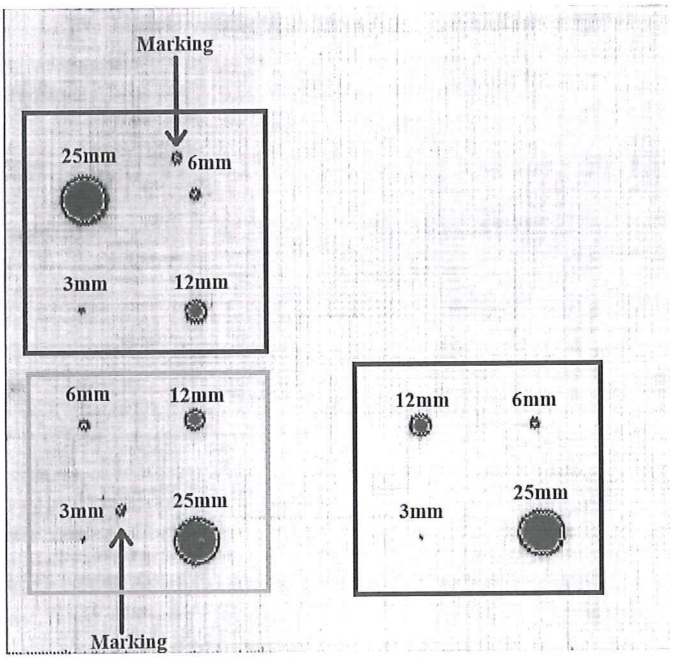

Figure 5.2: MRP test sample geometry

5.2. TESTING

This section will describe the testing methodology used to test the effects of the PAUT transducer frequency in the detection of delamination defects in GLARE as well as the settings used in each particular tests.

5.2.1. TESTING METHODOLOGY

In order to investigate the effects of PAUT transducer frequency in the detection of delaminations in GLARE, the three test samples described in section 5.1 were each tested using the three transducers described in section 4.2 in a factorial approach. The transducers ranging from 2.25MHz to 10MHz gave a good range of useful frequencies whilst the GLARE 3 and GLARE 4 samples gave a good variation in material properties.

During preliminary testing it was determined that the focusing depth of the PAUT transducer had a great effect in the quality of the results. Therefore the focusing of each PAUT transducer had to be tested with each test sample in order to eliminate the focusing factor and asses the effect of frequency on the detection of damage in GLARE. Therefore, each test sample was tested with each PAUT transducer utilizing five different focus depths. A flow chart of the testing performed is presented in figure 5.3. As can be seen from figure 5.3, the focusing tests for a specific transducer-test sample combination were averaged and then compared to the other PAUT transducers in that same sample, allowing for conclusions to be drawn regarding the influence of frequency. Lastly, observations on the three test samples allowed for final conclusions to be drawn.

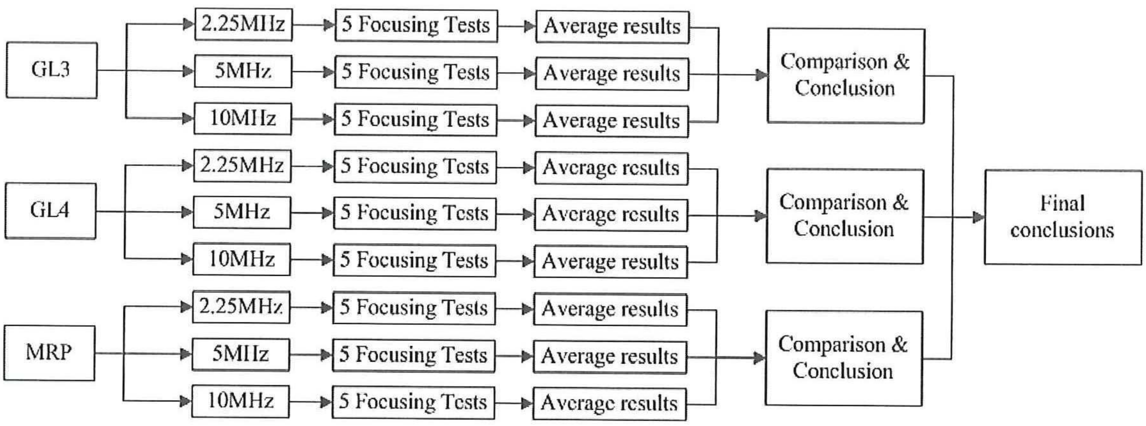

Figure 5.3: GLARE PAUT testing flow chart

The focusing tests were performed at depths of $1mm$, $2.5mm$, $5mm$, $10mm$ and $25mm$. These depths provided a reasonable range of focusing depths with smaller intervals in the thickness range of the test samples.

The steps performed for each test are given as:

1. Determine plate coordinates and insert them into the Motion Control Unit
2. Set standard settings such as plate dimensions, transducer properties, number of active elements, filters, signal averaging, axial resolution, etc to standard values
3. Adjust any parameters that conflict with each other
4. Retrieve maximum velocity from PAUT instrument and insert into Motion Control Unit
5. Set focusing depth and adjust the gain of the PAUT instrument
6. Perform automated scan

5.2.2. RELEVANT TEST SETTINGS

There are several important settings that have to be taken into consideration when performing PUAT inspections. This section will cover the the relevant settings and how they were set/chosen during testing.

FILTERS

Filters are software functions that offer the ability to remove (filter out) specific frequencies or frequency ranges. This allows for noise reduction when the frequency at which the noise occurs is well known. During the testing of the GLARE panels no filters were applied as important information could have been removed by applying filters.

FOCUS DEPTH

The focus depth F is the depth at which the PAUT transducer will have the highest pressure concentration. This was a parameter that had to be set in the PAUT instrument, which then automatically calculate the time delay laws to focus the defined PAUT beam at the desired depth in the defined material. It is however worthy of note that the delay laws are calculated for homogeneous materials, hence not being fully applicable to layered materials such as GLARE. This parameter was set to $1mm$, $2.5mm$, $5mm$, $10mm$ and $25mm$ in different tests.

ACTIVE ELEMENTS IN PAUT TRANSDUCER

The number of active elements in a PAUT transducer M determines the number of elements that are used simultaneously in one focal law to focus and receive information. As mentioned in section 3.8, the higher the number of elements, the better focusing and the better suppression of side lobes. However, the OmniScan SX had a maximum of 16 active elements, limiting the number of active elements that could be used in one focal law. However, as explained in section 3.8, increasing the number of elements above 16 only provided very minor improvements. Therefore, 16 active elements were always used during testing to get better focusing as well as better suppression of side lobes.

SIGNAL AVERAGING

Signal averaging (Avg) is an option available in the OmniScan SX which allows the sending and retrieval of a signal various times and taking the arithmetic mean of those signals as the final signal. This function allows for a reduction of noise at the cost of a reduced scanning velocity. During testing the signal averaging was set to average 16 signals when possible, as that was the maximum capability of the OmniScan SX. It is worthy noticing that in many tests the averaging had to be reduced due to velocity constraints, as will be further explained later.

SCAN RESOLUTION

The scan resolution Δx_{res} is the interval at which a measurement can be recorded in the scanning direction. The scanning resolution was limited by the maximum file size that the PAUT instrument could store (300Mb in the OmniScan SX). Therefore the scanning resolution was defined after the test sample dimensions and probe characteristics were inputted into the PAUT instrument. The scanning resolution was then selected to be as small as allowed by the file size constraints.

SCANNING VELOCITY

The scanning velocity v_s is the velocity at which the transducer moves when performing the scan. The maximum scan velocity is dependent on the scan resolution, the Pulse Repetition Frequency (PRF), and the signal averaging and is calculated by multiplying the PRF by the scan resolution. In some cases, the velocity required for scanning was too low (in the order of 2-5 mm/s) and the motors could not keep the velocity constant and would go over the maximum velocity limit, causing patches of missed data. In such cases, the averaging was reduced to be able to increase the scanning velocity and avoid the patches of missing data.

GAIN

The gain is the amplification of the receiving signal. Due to the different focus depths and PAUT transducer frequencies used, the gain had to be adjusted differently in different tests. During the testing, the gain was adjusted to a dB level where the back wall became clearly visible in the B-scan view. This was however not always possible due to high attenuation in certain tests (where the signal could not penetrate as deep as the back wall) or due to excessive amplification of noise in the signal when increasing the gain. In such cases the gain was set to a value where noise within the material was not excessively amplified.

5.2.3. TESTS

The tests performed were named according the the following nomenclature:

$$test\ name = \textbf{TestSample}\ T\ \textbf{TransducerFrequency}\ F\ \textbf{FocusDepth}$$

Where **TestSample** is the test sample on which the test was performed, **TransducerFrequency** is the PAUT transducer frequency used for the test and **FocusDepth** is the focus depth at which test was conducted. Therefore, test $MRPT2.25F5$ is the test performed on test sample MRP, with transducer $2.25L32$ and a focus depth of $5mm$. The settings used for the tests performed in the GL3 sample can be seen in table 5.2, whilst the settings used for the test performed on the GL4 and MRP samples are shown in table 5.3 and table 5.4 respectively. It is worthy noticing that there is no data available for the 10MHz transducer in the GL3 sample due to corruption of these data files.

5

Table 5.2: GL3 test settings

Transducer [MHz]	**F [mm]**	**M [-]**	**Avg [-]**	Δx_{res} **[mm]**	v_s **[mm/s]**	**Gain [dB]**	**Test Name**
	1	16	4	0.2	22	19	GL3T2.25F1
	2.5	16	4	0.2	22	19	GL3T2.25F2.5
2.25	5	16	4	0.2	22	19	GL3T2.25F5
	10	16	4	0.2	22	19	GL3T2.25F10
	25	16	4	0.2	22	19	GL3T2.25F25
	1	16	4	0.3	22	23	GL3T2.25F1
	2.5	16	4	0.3	22	23	GL3T5F2.5
5	5	16	4	0.3	22	23	GL3T5F5
	10	16	4	0.3	22	23	GL3T5F10
	25	16	4	0.3	22	23	GL3T5F25
	1	N/A	N/A	N/A	N/A	N/A	GL3T10F1
	2.5	N/A	N/A	N/A	N/A	N/A	GL3T10F2.5
10	5	N/A	N/A	N/A	N/A	N/A	GL3T10F5
	10	N/A	N/A	N/A	N/A	N/A	GL3T10F10
	25	N/A	N/A	N/A	N/A	N/A	GL3T10F25

Table 5.3: GL4 test settings

Transducer [MHz]	F [mm]	M [-]	Avg [-]	Δx_{res} [mm]	v_s [mm/s]	Gain [dB]	Test Name
	1	16	4	0.1	10	25	GL4T2.25F1
	2.5	16	4	0.1	10	25	GL4T2.25F2.5
2.25	5	16	4	0.1	10	25	GL4T2.25F5
	10	16	4	0.1	10	25	GL4T2.25F10
	25	16	4	0.1	10	25	GL4T2.25F25
	1	16	8	0.2	5	27	GL4T2.25F1
	2.5	16	8	0.2	5	27	GL4T5F2.5
5	5	16	8	0.2	5	27	GL4T5F5
	10	16	8	0.2	5	23	GL4T5F10
	25	16	8	0.2	5	23	GL4T5F25
	1	16	16	0.6	30	27	GL4T10F1
	2.5	16	16	0.6	30	27	GL4T10F2.5
10	5	16	16	0.6	30	27	GL4T10F5
	10	16	16	0.6	30	27	GL4T10F10
	25	16	16	0.6	30	27	GL4T10F25

5

Table 5.4: MRP test settings

Transducer [MHz]	F [mm]	M [-]	Avg [-]	Δx_{res} [mm]	v_s [mm/s]	Gain [dB]	Test Name
	1	16	8	0.2	10	10	MRPT2.25F1
	2.5	16	8	0.2	10	10	MRPT2.25F2.5
2.25	5	16	8	0.2	10	12	MRPT2.25F5
	10	16	8	0.2	10	15	MRPT2.25F10
	25	16	8	0.2	10	21	MRPT2.25F25
	1	16	8	0.2	7	20	MRPT2.25F1
	2.5	16	8	0.2	7	20	MRPT5F2.5
5	5	16	8	0.2	7	20	MRPT5F5
	10	16	8	0.2	7	23	MRPT5F10
	25	16	8	0.2	7	23	MRPT5F25
	1	16	16	0.65	30	19	MRPT10F1
	2.5	16	16	0.65	30	19	MRPT10F2.5
10	5	16	16	0.65	30	19	MRPT10F5
	10	16	16	0.65	30	21	MRPT10F10
	25	16	16	0.65	30	21	MRPT10F25

5.3. RESULTS AND DISCUSSION

This section will describe the criteria used to evaluate the results and will proceed by presenting the results and discussing them.

5.3.1. CRITERIA

Objective criteria are important in order to objectively determine the performance of the PAUT transducer frequencies when detecting defects. Four criteria were chosen to evaluate the performance of the PAUT transducers: detectability of defects, sizing of defects, depth determination of the defects and lastly the signal-to-noise ratio. These will be further discussed below.

DETECTABILITY OF DEFECTS

Within the context of this thesis, detectability is defined as the ability of the PAUT transducer to detect the artificial defects created in the test samples. This criteria was based on the visual inspection of the A-, B- and C-scans collected during each individual test and had three outcomes based on the 'detectability' of the defect: the defect was visible (V), the defect was barely visibly (BV) and the defect was non visible (NV).

A visible defect was defined as that which is clearly visible in any of the A-, B- and/or C-scans and could be sized utilizing the $6dB$ drop method, as explained later. This type of defect would be clearly qualified as a defect during a routine inspection due to its clarity. A barely visible (BV) defect was defined as a defect that was not easily identifiable and hence barely visible. These defects were *not* visible in all the views and were commonly only visible in the B-scan, where they appeared as a disturbance in the back wall. Even though they could usually be sized by manual measurement, they were not measurable with the $6dB$ drop method. The difference between a V and a BV defect can be seen in figure 5.4. Lastly, non visible (NV) defects were the ones that could not be seen by visual inspection of any of the views.

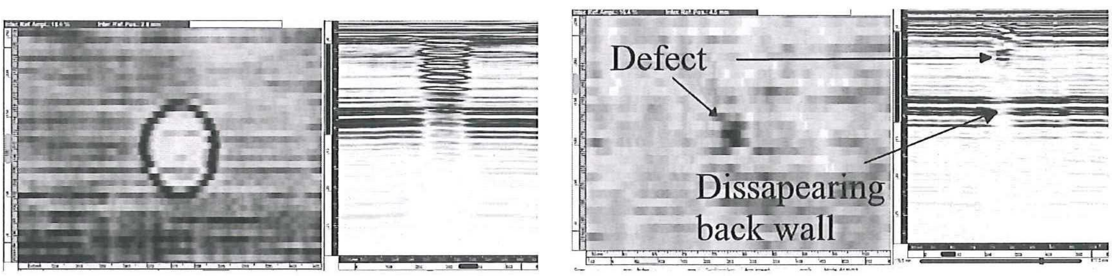

(a) Example of visible defect (V) (b) Example of barely visible defect (BV)

Figure 5.4: Difference between a visible and barely visible defects (test GL4T5F10)

The detectability criteria was applied to all defects in all the tests in order to gain an understanding of the defect detection capabilities of each transducer.

SIZING OF DEFECTS

The sizing criteria was used to determine how accurate the PAUT transducers could determine the dimensions of the defects when utilizing a well known defect sizing method, which as previously mentioned, was chosen as $6dB$ drop method. The $6dB$ method consisted of measuring the edges (beginning and end) of the defects when the highest amplitude of the signal created by the defect dropped by $6dB$, which corresponds to a decrease to half of the signal amplitude.[2]

To measure the size of the defects, the amplitude drop sizing utility function in Tomoview was utilized. This software function determined the maximum amplitude within a user specified region and then determined where it dropped below a user specified dB level, giving the location and size information of the defect. The measured dimensions of the defect were then compared to the known dimensions of the holes. Since the artificial defect's geometry was circular, the dimensions of the defects were measured in both the scan and index direction.

It is important to notice that defects nearest to the surface could appear as an attenuation rather than a reflection due to the fact that the reflection occurs very near to the surface, causing it to have a very high amplitude and become indistinguishable from the surface reflection. In such cases, the $6dB$ drop method was used in the opposite manner by measuring the locations where the signal increased above $6dB$, providing the same information.

Due to the large amount of artificial defects created and the large amount of tests performed, the sizing criteria was performed on all the $6mm$ diameter defects since they were the smallest size defects that were mostly visible during the tests. All the visible $3mm$ defects were also sized utilizing the $6dB$ drop method. However, the barely visible $3mm$ defects were sized manually utilizing cursors and best interpretation of the visible defect geometry. It is important to notice that current Quality Assurance procedures such as Fokker's C-scanning of the leading edge of the A380's horizontal and vertical tailplane only reject pieces with defects bigger than $6mm$. Hence detecting defects of $6mm$ or greater is of great importance.

DEPTH OF DEFECTS

The depths of defects criteria was used to determine how accurately the depths of the defects could be determined using the different PAUT frequencies. The depth of the defects was manually measured by measuring the distance between the surface reflection and the center of the reflection with the highest amplitude of the defect. The depth was determined for the $6mm$ defect at each depth. The measured results were compared to the known depths of the defects.

SIGNAL-TO-NOISE

The signal-to-noise ratio criteria was used to determine the quality of the signal. The signal-to-noise is conventionally determined by comparing the amplitude of the signal at the defect with the signal where no defect was present. The signal to noise ratio can be expressed as:

$$SNR = \frac{S}{N} \tag{5.1}$$

Where S is the signal amplitude over the defect and N is the signal amplitude at a reference point where no defect is present.

For the determination of SNR in this thesis, the defects GL3D9R1, GL3D9R3 and GL3D9R4 in GL3, the defects GL4D9R1, GL4D9R2, GL4D9R3 in GL4 and defects MRPD12R2C2, MRPD12R3C2 and MRPD12R3C3 in MRP were used as the reference defect points to record the amplitude. These defects were chosen for having a size big enough to always be detected as well as for their different depths (in the case of the GL3 and GL4 defects). The reference noise-signal where no defect was present was chosen halfway between the defect being used as a reference for the signal amplitude and the defect to its left (as seen from a C-scan).

5

5.3.2. RESULTS

DETECTABILITY OF DEFECTS

The results for the tests on the detectability of defects conducted on each individual panel can be seen in figure 5.5. These graphs show what percentage of defects were visible defects (V), barely visible defects (BV) and non visible defects (NV) utilizing all three different frequency transducers.

The graphs reveal that both the 2.25MHz and 5MHz frequencies have a 100% probability of detection across all test samples, whilst the 10MHz frequency only had 100% probability of detection on the GL4 test sample (note that there was no available data for the 10MHz frequency on the GL3 sample). It can also be seen that the 5MHz transducer has a better detectability than the 2.25MHz transducer since it has a higher percentage of visible defects on the GL3 and MRP test samples and the same percentage of visible defects on the GL4 test sample.

Testing also showed that in the GL3 and GL4 test samples, all frequencies were able to always detect the defects with 6mm diameter or bigger as V defects, and only the 3mm diameter defects were occasionally detected as BV. However, in the MRP test sample, only the 2.25MHz and 5MHz frequencies were capable of always detecting the defects with 6mm diameter or bigger as V defects whilst still detecting the 3mm diameter defects as V or BV. When inspecting the MRP, the 10MHz frequency detected some 6mm defects as BV whilst all 3mm defects were either found to be BV or NV.

The detectability of defects showed that the 5MHz transducer performed the best at detecting defects on all test samples whilst the 10MHz transducer performed the worst. Combining the results presented in figure 5.5, it is possible to view what the global performance of each frequency was in detecting defects, as shown in figure 5.6.

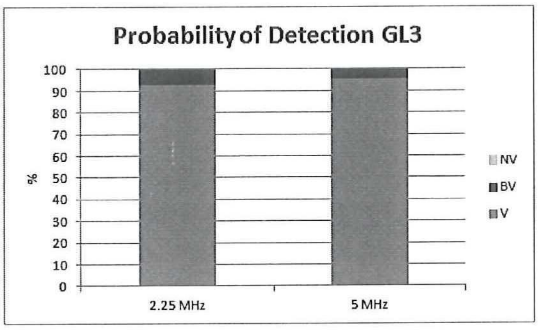

(a) Probability of detection in GL3 test sample

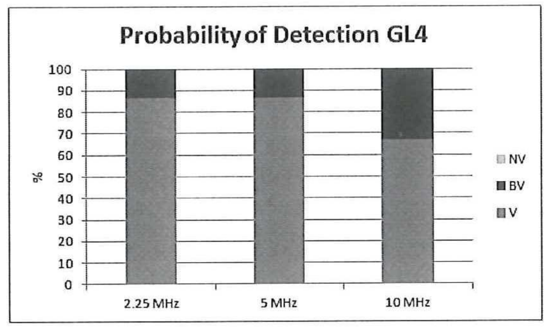

(b) Probability of detection in GL4 test sample

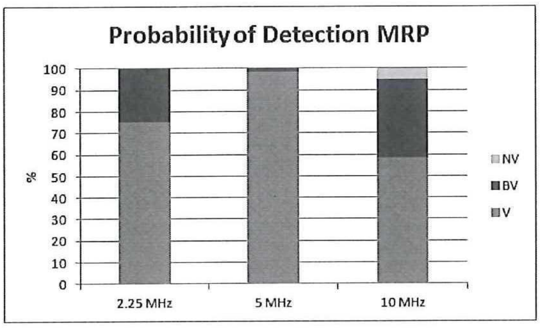

(c) Probability of detection in MRP test sample

Figure 5.5: Probability of detection of each individual test sample

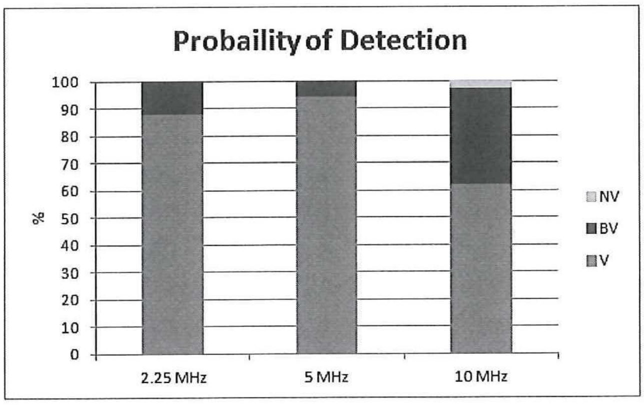

Figure 5.6: Probability of detection of visible defects (V), barely visible defects (BV) and non visible defects (NV)

From figure 5.6 it becomes evident that both the $2.25MHz$ and the $5MHz$ frequencies are capable of detecting 100% of the defects across all panels but that the $5MHz$ frequency is capable of the greatest number of visible detections. On the other hand, the $10MHz$ frequency had a probability of detection of 97.14%. It is also apparent that the $10MHz$ frequency performed much worse at detecting visible damage than the $2.25MHz$ and the $5MHz$ frequencies since it was only able to detect 61.9% of the defects as visible.

The poor performance of the $10MHz$ frequency on a thin test sample such as the MRP can be explained by its high noise level at the wedge-test sample interface and its high attenuation properties. As previously explained, due to the small wavelength of high frequencies, higher frequency signals are more easily disturbed than lower frequencies. Hence at the interface between the transducer and the test sample, it will have a bigger part of its signal reflected back, causing lot of noise near the surface. Therefore if a defect is near the surface it will get lost within the noise of the wedge-test sample interface and will not appear. In such cases one has to rely on the echoes of the signal, where the back wall disappears as shown in figure 5.4b. However, due to the high attenuation of the signal, the back wall echoes are weak in comparison to the original signal and disturbances are difficult to detect. This can be exemplified by looking at the B-scans of Row 4 in tests $MRPT5F2.5$ and $MRPT10F2.5$, as shown in figure 5.7.

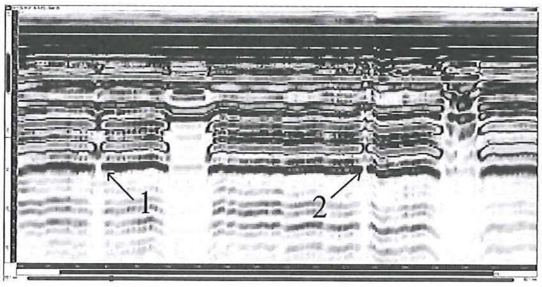

(a) B-scan of Row 4 of MRP test sample using 5MHz

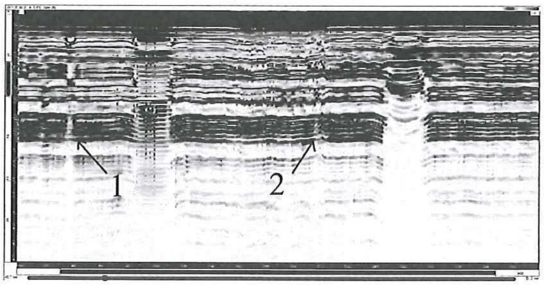

(b) B-scan of Row 4 of MRP test sample using 10MHz

Figure 5.7: B-scan of Row 4 of tests $MRPT5F2.5$ and $MRPT10F2.5$

As can be seen in figure 5.7, the signal echoes of the $10MHz$ frequency are considerably lower than those of the $5MHz$ at the same depth. Due to the stronger echoes and reduced noise in the $5MHz$ frequency, the back wall echoes show clear discontinuities, that when measured, give a reduction in signal amplitude greater to $6dB$. Therefore figure 5.7a is capable of displaying the two $3mm$ defects clearly. However, when looking at figure 5.7b defect 1 is apparent but defect 2 is very difficult to see since it could very well be noise. Measuring the reduction in signal strength at defect 2 shows a reduction in signal amplitude of $2.5dB$, which would not be considered a defect.

The depth of the defects seemed to have an effect on the detectability in both the $2.25MHz$ and the $5MHz$ frequencies in the GL4 and GL3 tests. In the tests conducted on the GL3 test sample, all the BV detection of both frequencies occurred at the 3mm deeper defects. In the GL3 sample, 9 of the 14 BV detections occurred on the deepest defect at $3.65mm$ deep whilst 5 of the 14 BV detection occurred on the $2.65mm$ defect. Furthermore, 9 out of 12 BV defects detected by the $2.25MHz$ and the $5MHz$ frequencies on the GL4 test sample occurred at the $3.35mm$ depth, further showing that as depth increases, the detectability becomes more difficult. This is caused by the attenuation of the ultrasonic signal as it travels through the depth of the material, where the signal being reflected will be weaker the further away it is reflected, hence making the detection more difficult. This agrees with the theory presented in chapter 3.

Interestingly enough the $10MHz$ frequency did not show such behavior in the GL4 test sample since it detected all the $3mm$ defects as BV defects regardless of depth whilst all other defects above $3mm$ diameter were detected as V defects. It is however important to notice that the $10MHz$ frequency should behave in a similar manner to the $2.25MHz$ and the $5MHz$ even though it should theoretically have a greater attenuation through the thickness of the material due to its smaller wavelength. Hence the detection of the defects should be expected to be more dependent on depth for the higher frequencies since they are more vulnerable to attenuation. However, it is noteworthy to mention that the data collected from the $10MHz$ is limited since no tests results were obtained from the GL3 testing and hence further testing should be conducted to verify the theory with the practice.

Conclusions

- $5MHz$ frequency provides the best detectability in all test samples with 94.3% visible detection
- $10MHz$ frequency performs very poorly on thin test samples (t<0.875mm)
- $6mm$ or greater diameter defects have a 100% probability of visible detection with the $2.25MHz$ and $5MHz$ frequencies
- $3mm$ defects have 100% probability of detection with the $2.25MHz$ and $5MHz$ frequencies
- The detectability of defects worsens as the depth of the defect increases

SIZING OF DEFECTS

The results for the tests on the sizing of defects conducted on each individual panel can be seen in figure 5.8. These graphs depict the average deviation between the measured size of the defect and the actual size of the defect for both the $3mm$ defects and the $6mm$ defects in both the scanning direction x and the index direction y in each individual panel.

The graphs presented in figure 5.8 show various interesting trends. One of the most obvious occurrences is the fact that the $3mm$ defects measurements have great deviations from the actual size of the defect, especially in the scanning direction where the deviation can be as high as 130%. The deviations in size measurement for the $3mm$ defects are also consistently higher than those for the $6mm$ defects, regardless of the frequency and the test sample. It also becomes apparent that the difference in size deviations between the scanning and index directions of the $6mm$ defects are relatively small in all the tests conducted. This is however not true for the $3mm$ defects where the difference in deviations between the scanning direction and the index direction are consistently significantly higher.

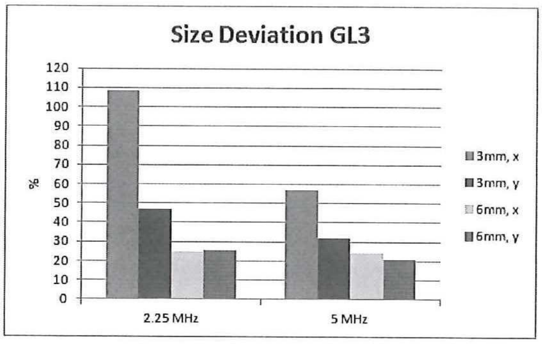

(a) Defect size deviation in GL3 test sample

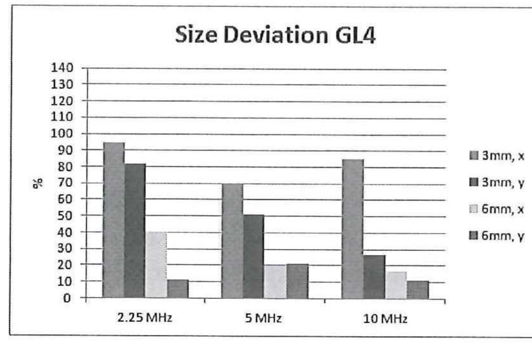

(b) Defect size deviation in GL4 test sample

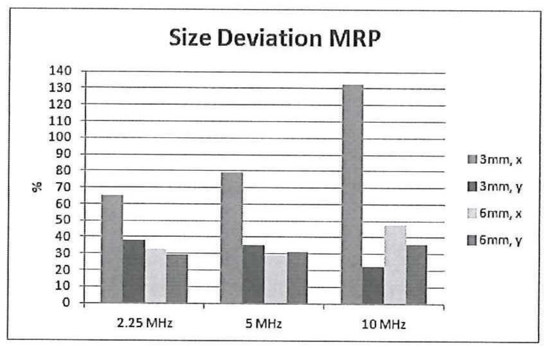

(c) Defect size deviation in MRP test sample

Figure 5.8: Defect size deviation of each individual test sample

It is important to present the standard deviation of size deviation. These standard deviations have been tabulated in table 5.5. It can be observed that in the case of the $2.25MHz$ and $5MHz$ frequencies, the standard deviation was smaller on the GL3 test sample than on the GL4 test sample. Furthermore, both transducers had the lowest standard deviations on the MRP. On the other hand, the $10MHz$ frequency had considerably higher standard deviations on the MRP, which reflected the poor performance of the $10MHz$ frequency on thin samples. Considering that the lowest standard deviation occurred on the thinnest panels for the $2.25MHz$ and $5MHz$ frequencies, it appears there might be a trend where smaller standard deviations occur on smaller thicknesses. However, the fact that both the $2.25MHz$ and $5MHz$ frequencies had smaller standard deviations in the GL4 than they did in the GL3 test sample, it appears that the type of GLARE might also affect the standard deviation of measurements. Therefore no definite conclusions can be drawn on such matter. It can however be concluded that, except the $10MHz$ frequency on the MRP, the differences in standard deviations between frequencies are relatively small. It is worth mentioning that the standard deviations are not excessively high and remain within reasonable limits.

It is also interesting to look at the resultant sizing deviation obtained when combining the deviations in the scanning direction as well as the index direction. By taking the square root of the deviations in the scanning and index direction squared, one can de-

Table 5.5: Standard deviation [%] of defect size deviation

	2.25MHz			5MHz			10MHz	
	GL3	GL4	MRP	GL3	GL4	MRP	GL4	MRP
3mm, x	9.073	16.362	12.389	16.810	19.152	12.673	16.764	50.676
3mm, y	9.428	15.592	7.698	12.872	16.826	7.698	7.191	3.536
3mm, av	9.250	15.977	10.043	14.841	17.989	10.185	11.977	27.106
6mm, x	15.251	19.109	0.000	10.224	12.317	4.538	7.767	31.872
6mm, y	7.303	7.890	3.849	9.250	8.592	7.698	6.692	14.222
6mm, av	11.277	13.500	1.925	9.737	10.454	6.118	7.230	23.047

termine the resultant deviations in size measurements. These are presented in figure 5.9, where the resultant deviations in sizing for both the $3mm$ and the $6mm$ defects are shown.

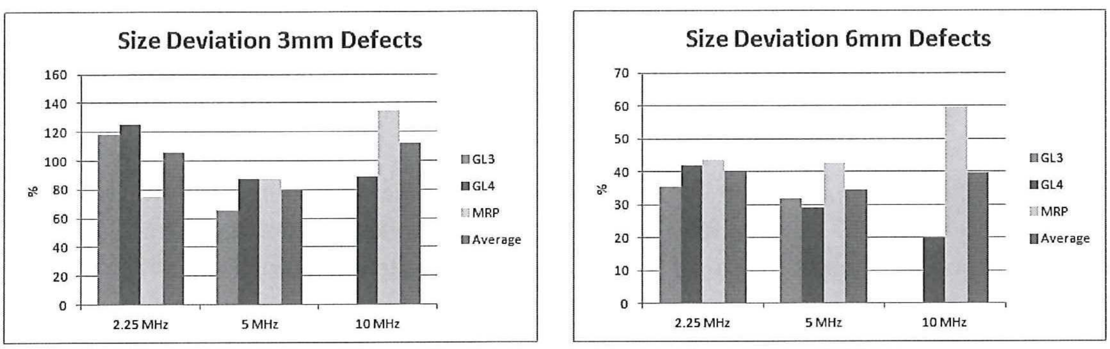

(a) 3mm defect size deviation

(b) 6mm defect size deviation

Figure 5.9: Defect size deviation of each individual test sample

Figure 5.9 confirms that there is indeed a great difference between the size deviation of the $3mm$ defects and the $6mm$ defects. The lowest average deviation in the sizing of the $3mm$ defects occurs with the $5MHz$ frequency and has a deviation of 79.8%, whilst the smallest average deviation in the sizing of the $6mm$ defects also occurs with the $5MHz$ frequency and has a deviation of 34.5%, which again demonstrates that the sizing of the $3mm$ defects is considerably worse than that of the $6mm$ defects.

The considerable difference in sizing deviation between the $3mm$ and $6mm$ defects observed in all the frequencies and is most likely due to the elevation size of the transducers. As mentioned in chapter 4.2, all three transducers had an elevation of $7mm$, which is more than twice the size of the $3mm$ defect. When performing the scans, the direction of the transducers elevation was parallel to the scanning direction, causing the great deviations in sizing in the scanning direction x in the $3mm$. To show this, one can assume that the ultrasonic signal sent by the transducer is a perfect square signal with a height of 1 (amplitude) and a length of $7mm$ (corresponding to the elevation of the transducer) and the signal caused by the $3mm$ defect is a perfect square signal which sends a signal of 0.5

(reflects the signal of the transducer with half amplitude) and a length of $3mm$. Performing a convolution of these two square waves simulates the movement of the transducer over the defect, which in turn produces the graph shown in figure 5.10.

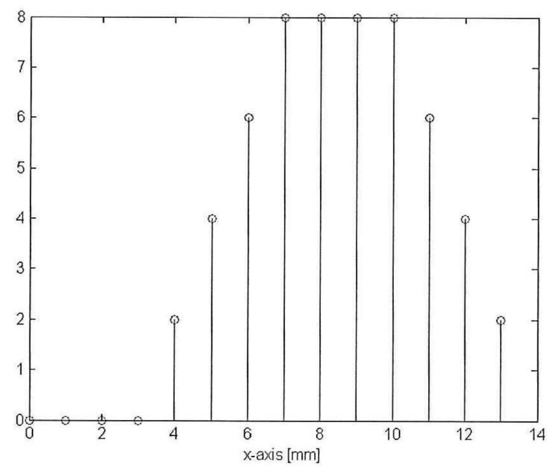

Figure 5.10: Convolution of the transducer square signal and the defect square signal

Looking at figure 5.10, one can see that the distance measured when the maximum signal drops to half (6dB drop criteria) is of $7mm$. It is worthy mentioning that when performing the same convolution on a defect with any size smaller than $7mm$, the same results are obtained. Hence it can be shown that theoretically, the transducer will measure about $7mm$, hence showing why the deviation in measurement in the x-direction was so high.

Looking at figure 5.9, it becomes evident that the $5MHz$ frequency performs the best at sizing both $3mm$ and $6mm$ defects in most test samples. Therefore, when looking at the averaged results across all test samples, the $5MHz$ frequency evidently performed better at sizing both $3mm$ and $6mm$ defects.

Looking at the sizing deviation in the $3mm$ defects of the averaged test samples, the $2.25MHz$ frequency had 5.6% less deviation in sizing than the $10MHz$ frequency, whilst in the $6mm$ defect sizing of the averaged test samples, the $10MHz$ frequency had 0.7% less deviation in sizing than the $2.25MHz$ frequency. However, it can be seen that this is caused by the poor performance of the $10MHz$ frequency on the MRP. Looking back at figure 5.9, it can be seen that the $10MHz$ frequency had 22% less deviation than the $2.25MHz$ frequency when sizing $3mm$ defects in the GL4 test sample and 8.9% less deviation than the $5MHz$ when measuring the $6mm$ defects in the GL4 panel.

It is worthy noticing that the $5MHz$ frequency had only 2% less deviation than the $10MHz$ frequency when measuring $3mm$ in the GL4 test sample, leading one to believe that the $10MHz$ frequency is perhaps as accurate or perhaps even more accurate than the $5MHz$ frequency when measuring defects in thicker panels. The poor sizing performance of the

$10MHz$ frequency on the MRP sample can again be justified by the high noise level at the wedge-test sample interface and its high attenuation properties, as previously explained.

The fact that the $5MHz$ frequency performed better than the $2.25MHz$ frequency at sizing is as expected. As explained in chapter 3, higher frequencies have smaller wavelengths which allow them to detect smaller defects and have a better resolution. It appears that the $5MHz$ frequency had the best balance between noise and resolution and therefore performed the best at most tests.

It is also interesting however to see how the sizing is affected by the depth of the defects. For such reason the deviations at different depths of the the $3mm$ and $6mm$ defects in both the GL3 and GL4 test samples are shown in figure 5.11.

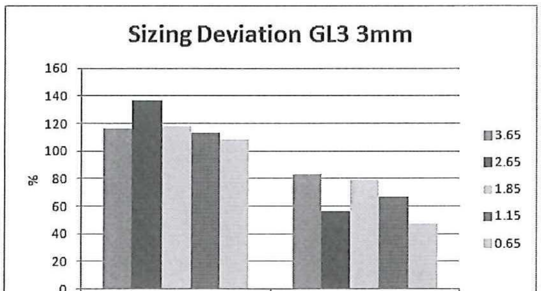

(a) 3mm defect size deviation in GL3

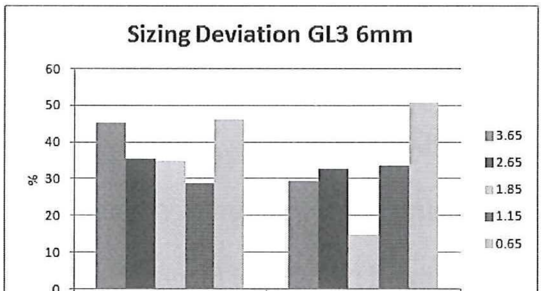

(b) 6mm defect size deviation in GL3

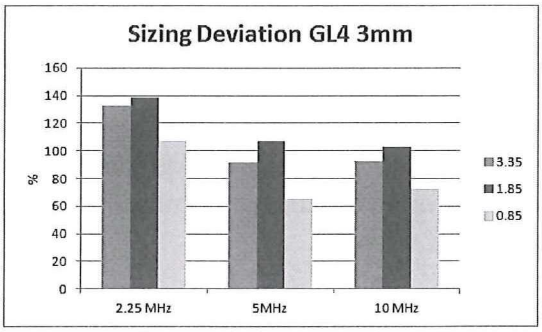

(c) 3mm defect size deviation in GL4

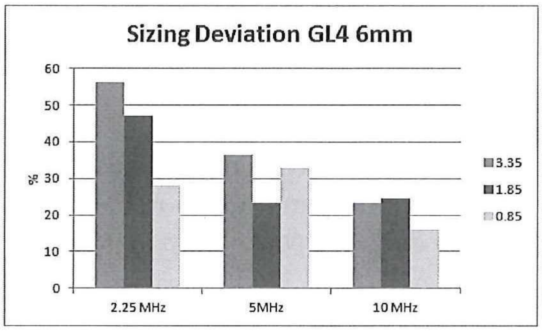

(d) 6mm defect size deviation in GL4

Figure 5.11: Defect size deviation at different depths

From figure 5.11 it becomes apparent that in most cases the sizing becomes worse as the depth of the defect increases. This again is as expected due to the fact that the deeper the defect, the more attenuated the signal will be, hence giving a weaker reflection. There are exceptions occurring at the shallower $6mm$ defects in the GL3 sample, where the deviations become greater. This type of deviation could be caused by the noise between the wedge-test sample interface. However, this does not occur in the $3mm$ defects in GL3, leading to the belief that it could be a measurement error.

Conclusions

Looking at the results from figure 5.9 it still appears that the sizing deviations are generally high, even for the $6mm$ defects. The best obtained result still had a deviation of 20%, which could still be considered an unacceptably high deviation when sizing critical parts. A transducer with a shorter elevation could prove a viable solution to improve the resolution in the scanning direction, hence improving the measurement results. Further conclusions are:

- $5MHz$ frequency is the most accurate at sizing defects in different panels
- $2.25MHz$ frequency appears to perform the best on thinner panels (t<0.875mm)
- $10MHz$ frequency appears to be the most accurate when measuring defects at depths greater than 0.85mm but further testing should be conducted to determine depth limitations
- Sizing deviations of $3mm$ diameter defects are more than 2x greater than defects of $6mm$ diameter
- Sizing of $3mm$ defects is unacceptably inaccurate
- Sizing deviation of $6mm$ defects is on average lower than 40%
- The sizing becomes less accurate for all frequencies as the depth increases , with as much as a 29% difference in defects with 2.5mm difference in depth
- Transducers with smaller elevations could potentially improve the sizing of defects

DEPTH OF DEFECTS

The results for the tests on the measurement of the depth of defects conducted on each individual panel can be seen in figure 5.12. These graphs depict the depth deviation of the $6mm$ defect at each depth in both the GL3 and GL4 panels.

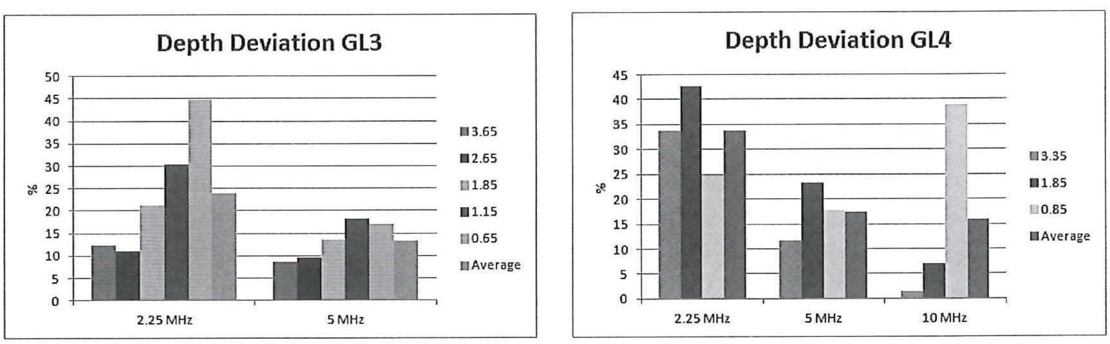

(a) Defect depth deviation in GL3 test sample

(b) Defect depth deviation in GL4 test sample

Figure 5.12: Defect depth deviation of each individual test sample

As can be seen from figure 5.12a, there seems to be trend where the deviation in the depth measurement increases as the depth of the defect becomes shallower. This could be caused by the interference between the signal caused by the defect and the 'entrapped' signals reflecting within the upper layers of GLARE. Due to the acoustic difference between the prepreg layers and the aluminum layers, signals might encounter a high reflection coefficient (of about 0.7) when going from aluminum to prepreg. This high coefficient means the signal will be be partly reflected and will retain an amplitude of 70% the original amplitude, which will then keep reflecting within the aluminum layer until it is attenuated. The presence of these signals could cause interference with the the defect signal when such a defect is close to the surface, hence causing greater deviations in the depth measurements. For defects further from the surface, this interference would be less problematic as the 'entrapped' signals would already be attenuated.

From figure 5.12 it also becomes apparent that on the averaged results the 10MHz frequency performs the best at determining the depth of the defects, followed by the 5MHz frequency, leaving the 2.25MHz as the worst performing when determining the depth of defects. However, the 10MHz frequency again suffers from the wedge-test sample interface noise issue, which greatly negatively affects its ability to perform depth measurements of defects near the surface. This is illustrated in figure 5.13.

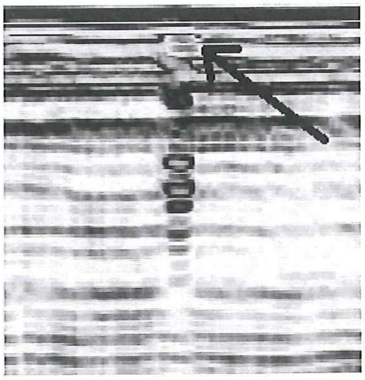

(a) 5MHz

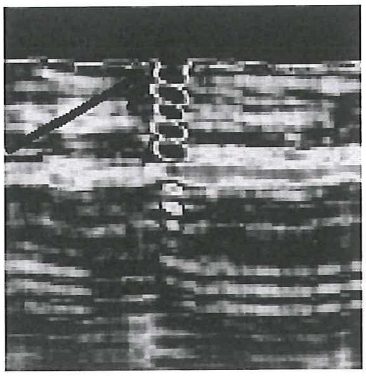

(b) 10MHz

Figure 5.13: Defect depth comparison for hole GL4R1D9 between 5MHz and 10MHz

As can be seen in figure 5.13, the same defect appears more distinctively separated from the interface noise in figure 5.13a with the 5MHz frequency than in figure 5.13b with the 10MHz frequency, where the defect appears right after the noise, implying that the defect probably occurs in the noisy part of the signal, hence not allowing for proper detection. Nevertheless, the fact that the 10MHz has more accurate detection on the deeper defects is as would be expected since the higher frequencies provide better sensitivity. It would however be expected that due to the greater attenuation of the 10MHz it would have lesser penetrability and hence not be able to detect defects at greater depths in GLARE.

It is worth mentioning that it was not possible to determine the depths of the defects in the MRP due to the defects being too close to the interface noise of the transducers.

Conclusions

- $5MHz$ frequency is the most accurate at determining the depth of defects in different panels
- $2.25MHz$ frequency performs very poorly at determining the depth of defects
- $10MHz$ frequency appears to be the most accurate when measuring depth of defects on defects at depths greater than 0.85mm but further testing should be conducted to determine depth limitations
- Near surface defects have greater deviations in depth measurement than deeper defects (up to 3.65mm depth)
- Depth cannot be determined in thin panels (t<0.85mm) or defects at depths smaller than 0.85mm

Signal to Noise Ratio

The results for the tests on the signal to noise ratio conducted on each individual panel can be seen in figure 5.14.

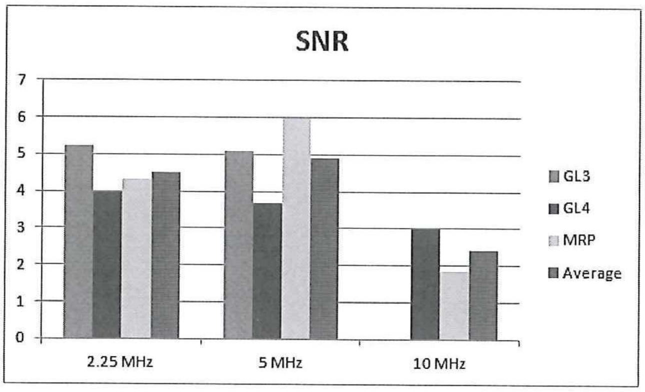

Figure 5.14: Signal to Noise Ratio (SNR) of the different test samples

Looking at figure 5.14, it can be seen that the $2.25MHz$ frequency had the highest signal to noise ratio on both the GL3 and GL4 test samples. However, the SNR on the MRP test sample was considerably higher for the $5MHz$ frequency. The signal to noise ratio of the $10MHz$ was consistently worse than the other two frequencies. These results are as expected since higher frequencies have higher noise levels due to their higher sensitivity.

It is interesting to note that the frequencies of the noise f_n were in most cases at frequencies lower than the central frequency f_c of the transducers. This can be seen in table 5.6, where the average frequencies of the noise are shown for each transducer. The frequency of the noise had to be manually measured because the signal of the A-scan was a rectified wave signal and hence a Fourier analysis was not possible. The noise was therefore measured by determining the time difference between two amplitude peaks of the signal at a location where no defects were present on the MRP.

Table 5.6: Signal to noise ratio of the different frequencies

	2.25MHz	5MHz	10MHz
f_c [MHz]	2.44	5	9.97
f_n [MHz]	1.9665	3.6699	8.5801

Knowing that the noise occurs within specific ranges allows for the use of frequency filters that could remove the undesired noise, thus improving the quality of the signal. However, further testing should be performed to verify the benefits of frequency filters.

5

Conclusions

- 2.25MHz has a better SNR in thicker test samples
- 5MHz has best SNR on thinner panels
- 10MHz has very poor SNRs
- The noise frequency occurs at slightly lower frequencies than the center frequencies

5.4. GENERAL DISCUSSION

The results obtained for the tests showed that the $5MHz$ frequency had the best detectability in all test samples and the best sizing of thin panels, whilst the $10MHz$ frequency excelled at the sizing of defects in panels greater than $0.85mm$ in thickness and the $2.25MHz$ offered the best SNR. On average however, the $5MHz$ frequency performed the best on most tests. The reason why the $5MHz$ performed so well most likely lies in the bandwidth of the transducer. Figure 5.15 shows an approximation of the frequency spectrum of each individual transducer, where it can be seen that the $5MHz$ frequency has a part in common with the $2.25MHz$ frequency and a small portion in common with the $10MHz$ frequency. This is most likely what makes the $5MHz$ frequency the most polyvalent frequency of all since it already acts as a 'multi-frequency' transducer, where the best balance between sensitivity and noise/attenuation is attained.

The testing showed that within the specified limits of this thesis, the $2.25MHz$ and $5MHz$ frequencies could detect all defects, whilst the $10MHz$ could not detect smaller defects in thin panels (t=0.87mm).However, no frequency could 'exclusively' detect one type of defect that could not be detected by others. Hence, from the results it becomes apparent that there is no real benefit at applying a multi-frequency approach to PAUT inspection

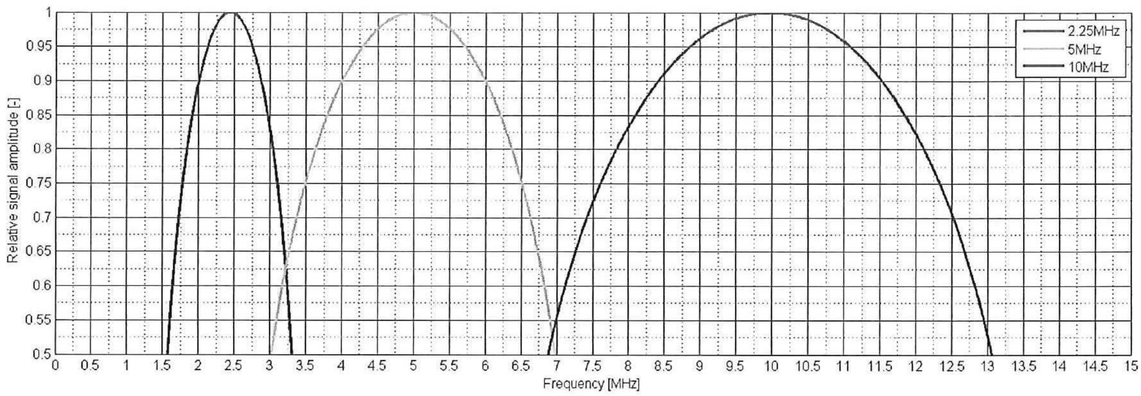

Figure 5.15: Transducer bandwidths

of GLARE laminates.

It is important to reflect on the fact that a multi-frequency approach system could be justifiable when different frequencies were exclusively capable of detecting a specific type of defect within GLARE. However, when one frequency detects all types of defects that other frequencies can detect, there is no real benefit in designing a complex and expensive system that operates at different frequencies.

It has also been shown that PAUT transducers can reliably detect delaminations of different sizes in different types and thicknesses of GLARE at different depths. The $2.25MHz$ and $5MHz$ frequency were both capable of detecting all types of defects in all the tests samples, including the $3mm$ defects. This is important since some components of GLARE such as the D-noses of the A380 are allowed to have manufacturing defects smaller than $6mm$, meaning that PAUT can detect defects smaller than are necessary. However, further optimization of transducer selection (transducers with smaller elevations) and/or standardized testing procedures are required to obtain more accurate sizing of smaller defects in GLARE.

When performing a blind inspection where the exact geometry of the part is not known, the $5MHz$ transducer would prove to be the most useful transducer since it has the best detectability and the best sizing across different types of GLARE and essentially acts as a multi-frequency transducer. One situation where a second frequency could be useful would be in the case that an accurate sizing of a defect was necessary, for example on a defect located in a critical part of an aircraft. In such a case a higher frequency such as $10MHz$ could provide up to 10% less deviation in the measuring of the defect (assuming the thickness is higher than t=0.87mm). Therefore, the $5MHz$ frequency could act as the defect detector and the $10MHz$ could be used for the sizing. However, this benefit would be minimal if calibrations or comparisons with known hole sizes were performed.

REFERENCES

[1] R. A. M. Coenen, *Design of a Quality Assurance System for Structural Laminates*, Ph.D. thesis, Delft University of Technology (1998).

[2] P. McIntire, R. E. J. Green, and A. S. Birks, eds., *Nondestructive Testing Handbook- Volume Seven: Ultrasonic Testing*, 2nd ed. (American Socirty for Nondestructive Testing, 1991).

5

6

Phased Array Ultrasonic Modeling in GLARE

Developing a model of the behavior of PAUT waves in GLARE can allow for a deeper understanding on the effect of frequency in PAUT inspection of GLARE. Phased Array Ultrasonic modeling has been successfully performed with analytical methods based on the Huygens-Fresnel superposition principle and the Rayleigh-Sommerfeld integral (RSI), semi-analytical models based on the Distributed Point Source Method (DPSM) and numerical methods based on the Finite Element Method (FEM) [1]. These were however determined to be unsuitable for modeling GLARE since these models had been applied for homogeneous isotropic materials and were too complex for the scope of this thesis [2].

Modeling of ultrasonic waves in GLARE had been performed by Coenen [3] to determine the most suitable frequency for a C-scan quality assurance system at TU Delft. The transfer function determined by such a model was confirmed to be very similar to the measured transfer function of a GLARE 3 3/2 layup. The model utilized by Coenen was developed for a through-transmission method utilizing conventional UT transducers and where a water jet was used for ultrasonic coupling. In this section the model utilized by Coenen will be explained, and an adapted version of such model will be proposed for the determination of attenuation in the pulse-echo method. The results will then be presented and discussed.

6.1. Coenen's Model

The through transmission model utilized by Coenen was based on sound-wave propagation in discretely layered media theory presented by Brekhovskikh [4]. The model makes various assumptions that simplify the model but still provide accurate results. The assumptions were as follow:

1. No attenuation of any layer

2. Layers have a homogeneous thickness and constant velocity within the layer
3. Bandwidth of transducer is not taken into account, only center frequency
4. No measurement errors or amplification distortions
5. No frequency-dependent velocity effects
6. Flat wave was assumed

Assuming perfectly homogeneous material layers, the transfer matrix of a laminated layer was described as the multiplication of the transmission matrices of each individual layer of the laminate as follows:

$$M_{laminate} = \prod \begin{bmatrix} cos(\delta(f,d,c)) & \frac{i}{z_{layer}} sin(\delta(f,d,c)) \\ i z_{layer} sin(\delta(f,d,c)) & cos(\delta(f,d,c)) \end{bmatrix} \tag{6.1}$$

Where $\delta(f,d,c)$ was the advance in the phase of the wave within the layer's thickness as a function of: the frequency f, the layer's thickness d and the velocity within the layer c. Assuming these three variables are constant (as stated in the assumptions), $\delta(f,d,c)$ could be defined as:

$$\delta(f,d,c) = \frac{2\pi d f}{c} \tag{6.2}$$

The total acoustic impedance of the laminate $Z_{laminate}$ was then defined as:

$$Z_{laminate}(f) = \frac{p}{v_z} \tag{6.3}$$

Where p is the pressure and v_z is the velocity of the acoustic wave in the medium in the z-direction (across the thickness). These values can be defined in a vector utilizing the following relation:

$$PV(f) = M_{stack}(f) \cdot \begin{bmatrix} 1 \\ z_{water} \end{bmatrix} \tag{6.4}$$

Where the first value of PV defines p and the second value defines v_z. Using equations 6.1 and 6.4, $Z_{laminate}$ could be found. The amplitude reflection coefficient R was then defined by assuming the change between media to be between the water jet coupling and the GLARE laminate, thus becoming:

$$R(f) = \frac{Z_{water} - Z_{laminate}(f)}{Z_{water} + Z_{laminate}(f)} \tag{6.5}$$

Lastly, the total transmission coefficient of the laminate was determined to be as follows:

$$T(f) = \sqrt{1 - R(f) \cdot \overline{R(f)}} \tag{6.6}$$

From equation 6.6, it was possible to determine the attenuation that the ultrasonic signal undergoes when penetrating GLARE. Coenen utilized this predicted attenuation to guide in the selection of the best frequency for through transmission inspection in a C-scan quality assurance system for GLARE.

6.2. Adapted Coenen's Model for Pulse-Echo

The model utilized by Coenen was adapted in order to predict the attenuation of the ultrasonic signal within GLARE when using the pulse-echo method with PAUT. There were however several further assumptions that had to be considered. These were:

1. PAUT beam was at 0° and thus creating a perfect flat wave
2. There were no interactions between the scattered signals within layers caused by the 'pulse' signal and the 'echo' signal
3. No signal loss or perturbation occurred when the acoustic signal was reflected back in the pulse-echo method
4. The transducer was coupled with water and the opposite side was kept dry and in contact with air

Coenen's model was adapted to be used with pulse-echo by simulating the equivalent of a ultrasonic signal's path in pulse-echo in a through transmission manner. The concept is clearly depicted in figure 6.1.

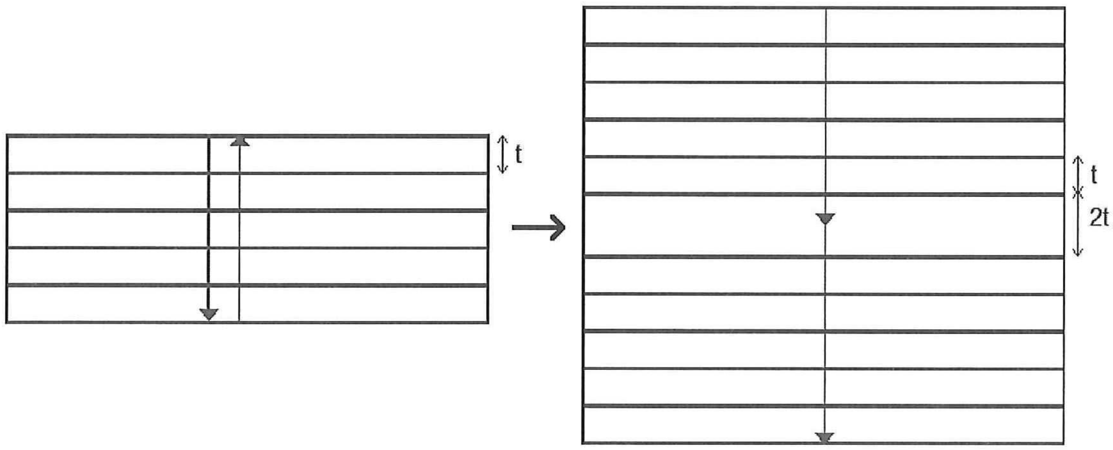

Figure 6.1: Pulse-echo signal (left) adapted to through transmission (right)

In the pulse-echo method, the signal travels twice the thickness of the material, covering one full thickness in the 'pulse' signal (represented as red in figure 6.1) and covering another full thickness in the 'echo' signal (represented as blue in figure 6.1). This can be considered equivalent to a single through transmission signal traveling through the same panel with twice the thickness/layers, as can be seen in figure 6.1.

In reality, when the signal is reflected in pulse-echo, part of the signal will be transmitted and part will be reflected back. However, when the signal is traveling from aluminum to air, the signal will have a reflection coefficient of 0.999, meaning that virtually all the signal will be reflected back and very little transmitted to air. If the signal traveled from aluminum to water, the reflection coefficient would then be 0.84, making this adaptation invalid.

Therefore, the model utilized by Coenen was adapted to take into consideration the middle layer with double thickness as well as the doubled thickness of the panel. The second modification performed on the model was meant to provide the attenuation of the signal in relation to the first reflection that would occur at the surface. This last modification was performed by calculating the reflection at the surface utilizing the same methodology as explained in section 6.1 but utilizing a single aluminum layer.

6.3. RESULTS

The model utilized by Coenen was verified for a GLARE 3 3/2 layup sample. Therefore, the adapted model was verified with the MRP test sample since it is a GLARE 3 3/2 panel. The results as obtained from the model can be observed in figure 6.2.

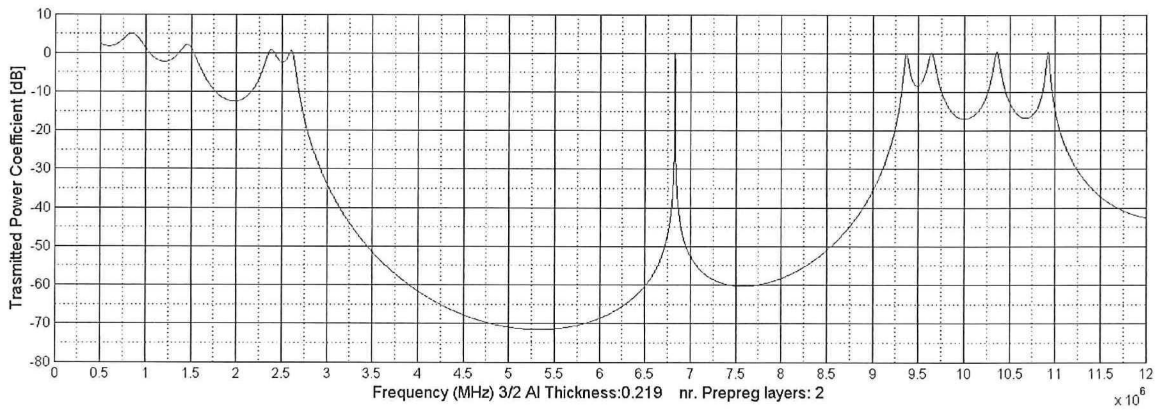

Figure 6.2: Pulse-echo signal (left) adapted to through transmission (right)

Looking at the results of the adapted model of figure 6.2, one can observe that the attenuation at $2.44MHz$ is lower than that of the $9.97MHz$, which would be as expected since higher frequencies have greater attenuations. However, the $5MHz$ frequency shows an extremely high attenuation of up to $-70dB$.

In order to take the bandwidth into consideration, the attenuation was scaled according to the frequency distribution of each transducer as presented in figure 5.15. Hence, the attenuation occurring at the center frequency was multiplied by a factor of 1 whilst the attenuation at the -6dB frequency was multiplied by a 0.5 factor. Performing this scaling for the full bandwidth of each transducer and then summing up all the scaled attenuations allowed for the determination of an average attenuation through the full bandwidth.

The results of the predicted attenuations were compared to the measured attenuations at the center frequency and those averaged through the full bandwidth of each transducer, where the results were tabulated into table 6.1. It can be clearly seen that the model has great deviations from the actual measured values in both the center frequency predicted attenuation and the bandwidth corrected attenuation. This was more pronounced on the $5MHz$ frequency, where the signal attenuation was predicted to be seven times higher than the actual recorded value. The bandwidth corrected attenuation seemed to reduce the difference between the calculated attenuation and the measured attenuation for both the 2.44MHz and the 5MHz frequencies. However, it worsened that of the 9.97MHz frequency. It could however not correct or explain the considerable deviation in attenuation of the 5MHz frequency.

Table 6.1: Predicted attenuations and measured attenuations in the MRP

	2.44Mhz	5MHz	9.97MHz
Center Frequency Predicted Attenuation [dB]	-0.9	-70.9	-16.8
Bandwidth Corrected Attenuation [dB]	-12.5	-54.0	-33.2
Actual Attenuation [dB]	-7	-9.5	-11.2

Looking again at figure 6.2, it could also be seen that the attenuation was very sensitive to the frequency, where a change in $0.25MHz$ could cause an attenuation difference of $6dB$. One of the model's assumption was that the transducers only vibrated at their center frequency. However, as has been previously shown, the transducers used during the testing of this thesis had relatively large bandwidths, which could possibly cause the discrepancies found between the actual attenuation of each transducers and that determined by the model.

In order to shed some light on the possible reasons causing the differences between the model and the actual measured values, a sensitivity analysis on various parameters affecting the model was performed. Looking at section 6.1, it seemed apparent that the density, thickness and sound velocity in the different layers of GLARE could all have great effects on the outcome of the model. Therefore, the density, thickness and sound velocity for both the aluminum and prepreg layers were varied between $\pm10\%$ of the known values. The results for the density sensitivity test are presented in figure 6.3.

Figure 6.3 showed that the $9.97MHz$ frequency had very little sensitivity to changes in density, whilst the $2.44MHz$ and $5MHz$ frequencies had considerably small sensitivities as well. Whilst the density of the aluminum should be expected to remain constant, the prepreg (epoxy) density could be expected to variate through the panel. However, the MRP had been inspected repeatedly with an ultrasonic C-scan and no significant changes in density could be observed. It was therefore concluded that the model's sensitivity to density variations was not responsible for the differences between the model and the actual measurements. Therefore, the thickness sensitivity analysis was performed, as shown in figure 6.4.

From figure 6.4, one could observe that the $5MHz$ frequency is very insensitive to the

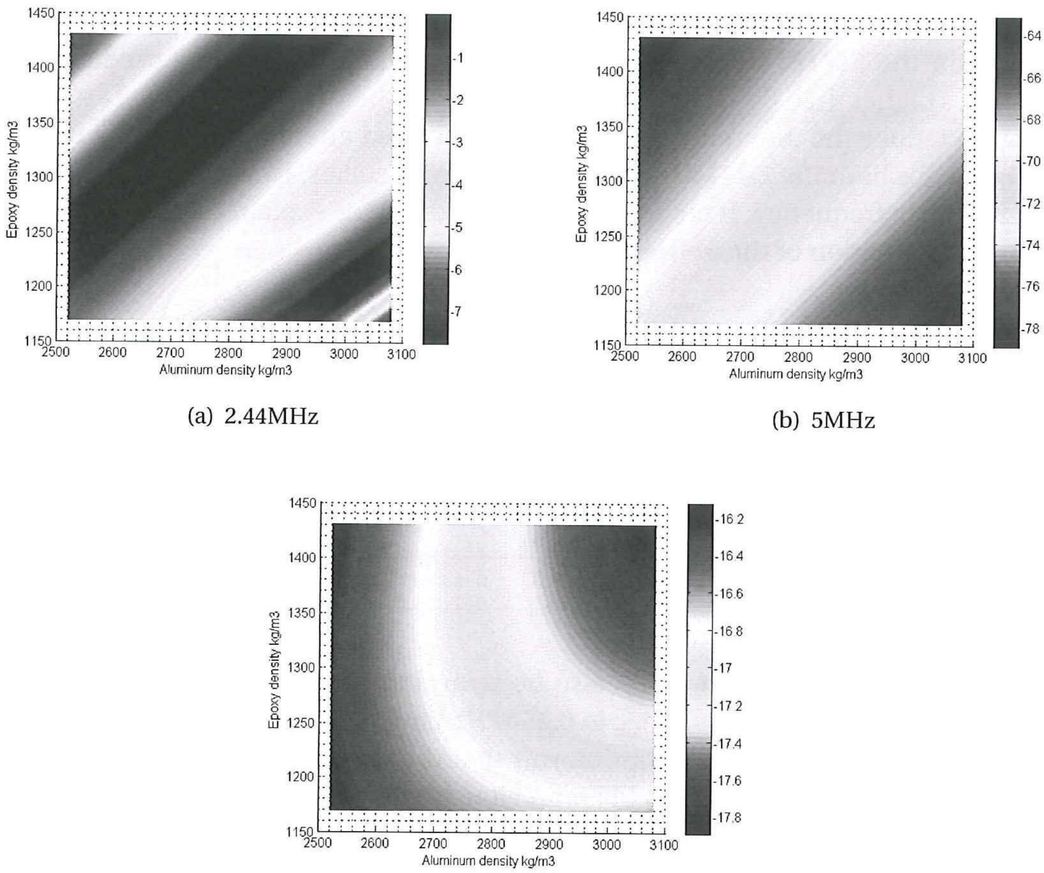

(a) 2.44MHz

(b) 5MHz

(c) 9.97MHz

Figure 6.3: Density sensitivity analysis

thickness changes, leading one to believe that the thickness variations could not explain the $60db$ difference in attenuation between the adapted model and the actual measurements. On the other hand, the $2.44MHz$ frequency was relatively sensitive to the thickness variations, where a change of 10% could cause a $6dB$ change in attenuation. Considering that the standard deviations of the thickness of both aluminum and prepreg layers in the MRP were of 13%, the deviation between the model's results and the actual results in the $2.44MHz$ could be due to the variations in thickness. Lastly, the $9.97Mhz$ frequency was very sensitive to the thickness variations, where a change in 10% thickness could cause as much as $15dB$ change in attenuation. Again, considering that the standard deviations of the thickness in the MRP were of 13%, it was very probable that the difference between the actual results and the model in the $9.97MHz$ frequency were due to the variations in thickness.

Figure 6.5 lastly showed the velocity sensitivity analysis of the adapted model for the MRP. As can be observed, both the $2.44MHz$ and the $5MHz$ frequencies were relatively sensitive to the velocity, where changes in the acoustic velocity of 10% could cause changes

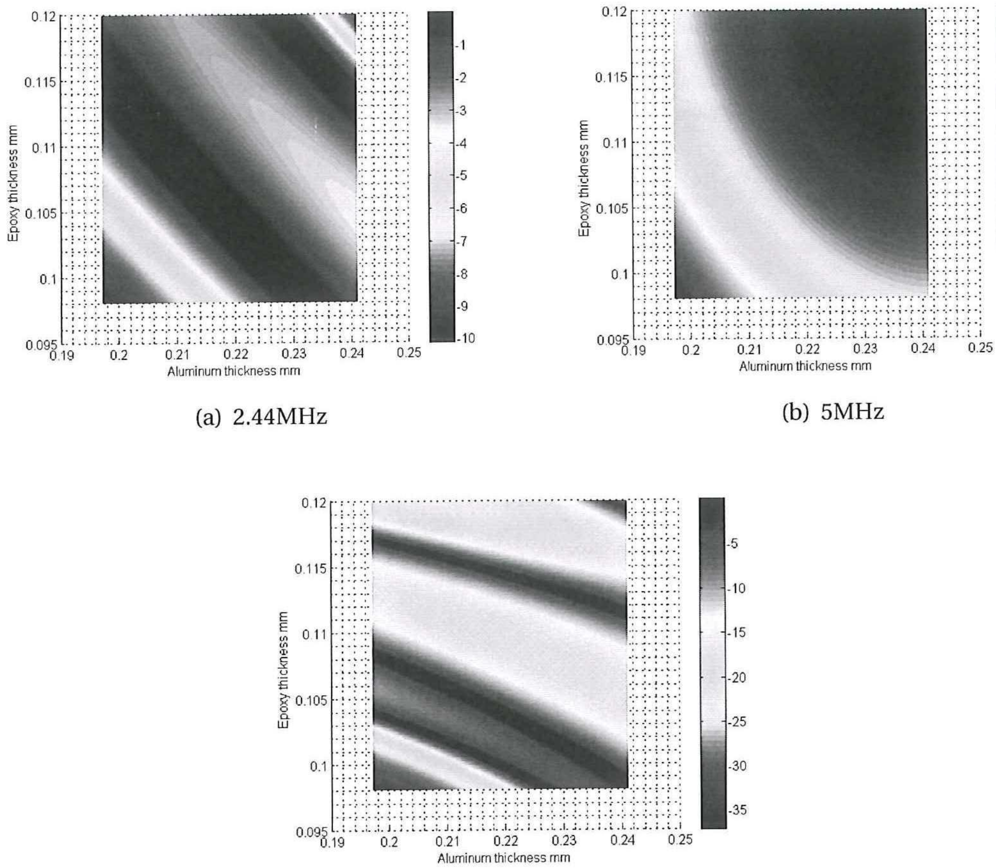

(a) 2.44MHz (b) 5MHz (c) 9.97MHz

Figure 6.4: Thickness sensitivity analysis

in attenuation of up to $8dB$. This could explain the difference in variation between the model and the measured attenuation in the $2.44MHz$ since the acoustic velocity in the prepreg material might not be as constant due to the presence of fibers. This however does not explain the differences on the $5MHz$. Lastly, the $10MHz$ frequency was very sensitive to changes in velocity, where attenuation differences of up $30dB$ could occur due to changes of as little as 5% in the material's velocity. This could again explain the deviation between the model and the deviations.

6.4. DISCUSSION

The results showed that the adapted model could not predict very accurately the attenuations that occurred in the MRP. It was shown that the factors such as the thickness and acoustic velocity variations within the aluminum and prepreg layers could have a significant impact on the predicted attenuations and could explain the deviations between the model's results and the actual measured results. Furthermore, on many occasions, the deviations that could occur due to individual parameters did not have a great effect

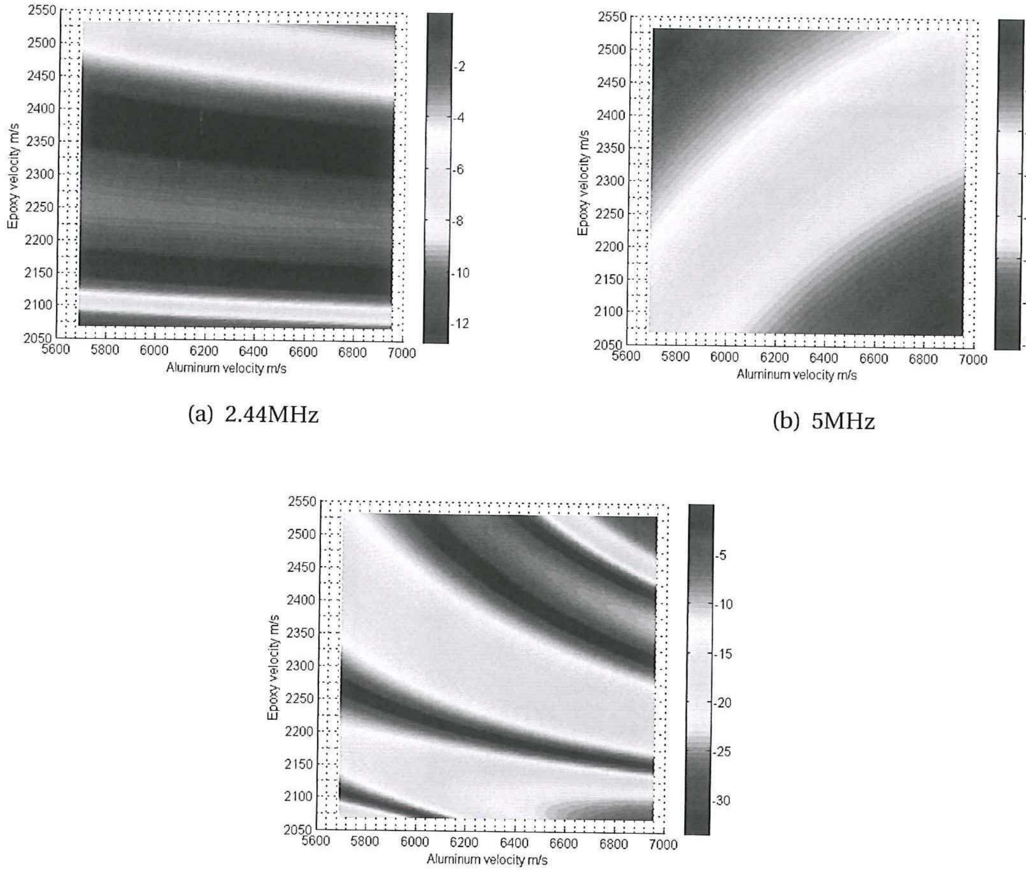

(a) 2.44MHz

(b) 5MHz

(c) 9.97MHz

Figure 6.5: Velocity sensitivity analysis

on the results. However, the sum of all these together could have significant effects on the results of the model. Nevertheless, it is important to realize that these combined deviations could not explain the extreme difference in the model's predicted attenuation and the actual measure attenuation of the $5MHz$ frequency. No reasonable explanation was found for such deviation.

It is important to state that the adapted model was also tested on the GL3 and GL4 test samples, where the attenuation was predicted to be as high as $-160dB$ (the model's limit) on a wide variety of frequencies. Needless to say the attenuation was excessively overestimated. Hence it was concluded that the model was not applicable for panels with layups of 5/4 or higher.

The adapted model seems to have the potential to predict the frequency attenuation in GLARE samples with layups of 3/2. However, the sensitivity of the model might be too high to make it a viable model for GLARE since the material properties such as thickness seem to vary too much for the adapted model to give accurate results. Furthermore, the model had an inexplicable inaccuracy at the $5MHz$ frequency, which requires further research.

In order to make the model a useful tool for pulse-echo ultrasonics in GLARE, it would be important to improve the model so that that it took into consideration factors such as pulsed and echoed signal interference and bandwidth considerations. Nevertheless, it was concluded that the adapted model in its current state did not accurately predict the attenuation in GLARE samples and hence was not a useful tool to determine the frequency attenuation in GLARE.

REFERENCES

[1] T. Kundu, D. Placko, E. K. Rahani, T. Yanagita, and C. M. Dao, *Ultrasonic Field Modeling : A Comparison Numerical Techniques,* IEEE Transactions on Ultrasonics, Ferroelectrics and Frequency Control **57**, 2795 (2010).

[2] V. Fraguas Garcia, *A review of defects and damages in Glare, Non-Destructive Inspection methods to detect them and Phased Array Ultrasonics for NDI of Glare,* Tech. Rep. (Delft, 2014).

[3] R. A. M. Coenen, *Design of a Quality Assurance System for Structural Laminates,* Ph.D. thesis, Delft University of Technology (1998).

[4] L. M. Brekhovskikh and O. A. Godin, *Acoustics of Layered Media I,* 1st ed. (Springer-Verlag Berlin Heidelberg, New York, 1990).

7

Conclusions and Recommendations

The objective of this thesis was to investigate the effects of the frequency of ultrasonic waves of Phased Array Ultrasonic (PAUT) transducers on the detection of defects and damages in GLARE in order to evaluate the benefits of a multi-frequency PAUT approach capable of reliably performing in-service inspections of GLARE in a near future. To attain this goal, a comprehensive review on the defects and damage occurring in GLARE as well as on the physics of PAUT was presented. This knowledge was used to create a testing method utilizing three different test samples comprised of different types of GLARE with different types of thicknesses, with defects being modeled by drilled flat bottom holes and Teflon inserts. The results were then judged on the criteria of detectability, sizing of defects, depth determination of defects and Signal to Noise Ratio. Lastly, a model was proposed which could be capable of determining the attenuation in ultrasonic waves in GLARE in the pulse-echo mode. These results were then compared to actual experimental data.

Testing showed that the $5MHz$ frequency was the best frequency to use to detect delaminations in flat GLARE panels of thicknesses between 0.875mm and 5.2mm, with a probability of detection of 100%, where 94.3% of these defects were visible defects. The $5MHz$ was also determined to have the best performance when sizing defects across different panels. However, the $10MHz$ frequency appeared to perform better sizing on panels thicker than 0.875mm. A similar trend occurred on the depth detection where the $5MHz$ frequency performed the best across different panels and defect depths whilst the $10MHz$ performed better at defects at depths bigger than 0.85mm. Lastly, the $2.25MHz$ frequency had the best SNR on thick panels (t>0.85mm) whilst the $5MHz$ had better SNR on thinner panels (t<0.85mm).

The results of the testing showed that a multi-frequency approach to PAUT inspection of GLARE panels would provide negligible benefits to a single-frequency approach where the frequency has been selected thoughtfully. The $5MHz$ consistently performed better across the different test samples and different criteria. The benefits of applying a different frequency to $5MHz$ provided very little benefit. In the case of sizing the benefits never exceeded a margin of 15% less deviation in measurement whilst the same held true for the depth determination.

It was therefore concluded that a multi-frequency approach to PAUT inspection of GLARE panels did not provide significant benefits to using a $5MHz$ transducer when inspecting flat panels of thicknesses between 0.875mm and 5.2mm. The reason the $5MHz$ frequency performs so well most likely lies in the fact that the bandwidth of the transducer was very high (79%), meaning that it vibrated at frequencies between $2.5MHz$ and $7.5MHz$, with a center frequency at $5MHz$. This in essence made it a multi-frequency transducer.

The model proposed during the thesis showed potential for the determination of the attenuation of ultrasonic waves in pulse-echo but was deemed unsatisfactory in its current state since it could not accurately predict the attenuation in the MRP. It was determined to be excessively sensitive to parameters such as thickness, density and ultrasonic wave velocity, causing significant errors. Furthermore, inexplicable attenuation was predicted at $5MHz$ several orders of magnitude higher than measured. It was also deemed unsatisfactory for plates having a layup higher than 3/2.

7.1. RECOMMENDATIONS

Several recommendations can be made for future work. These are as follows:

- Develop models to create accurate focal laws for laminated materials such as GLARE in order to have a better control and understanding of the focusing within GLARE.
- Develop a model to determine the attenuation of ultrasonic signals in GLARE with PAUT ultrasonics, taking into consideration factors such as pulsed and echoed signal interference, bandwidth considerations and angles of incidence greater than $0°$.
- Utilize a PAUT instrument with higher memory capacity to avoid limits in resolution and with the capability to perform Dynamics Depth Focusing tests.
- Investigate new geometries such as curved panels, splices and stringer attachments.
- If possible, perform tests with transducers with smaller elevations and different configurations in order to determine the limitations of size detection of frequencies and not transducers.